

# Single Electron-ics with Carbon Nanotubes



# Single Electron-ics with Carbon Nanotubes

## Proefschrift

ter verkrijging van de graad van doctor  
aan de Technische Universiteit Delft,  
op gezag van de Rector Magnificus prof. ir. K.C.A.M. Luyben,  
voorzitter van het College voor Promoties,  
in het openbaar te verdedigen op vrijdag 2 juli 2010 om 10:00 uur

door

**Georg Thomas Jakob GÖTZ**

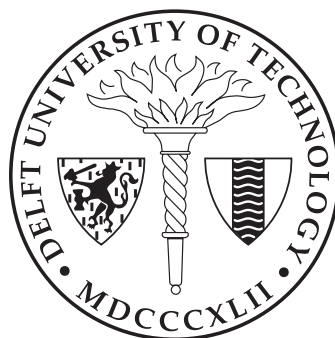
Diplom - Physiker, ETH Zürich, Zwitserland  
geboren te Hamburg, Duitsland.

Dit proefschrift is goedgekeurd door de promotor:

Prof. dr. ir. L.P. Kouwenhoven

Samenstelling van de promotiecommissie:

Rector Magnificus	voorzitter
Prof. dr. ir. L.P. Kouwenhoven	Technische Universiteit Delft, promotor
Prof. dr. C.M. Marcus	Harvard University, Verenigde Staten
Prof. dr. ir. J.E. Mooij	Technische Universiteit Delft
Prof. dr. J.M. van Ruitenbeek	Universiteit Leiden
Prof. dr. B.J. Thijsse	Technische Universiteit Delft
Prof. dr. B. Trauzettel	Universität Würzburg, Duitsland
Prof. dr. ir. W.G. van der Wiel	Universiteit Twente
Prof. dr. ir. H.S.J. van der Zant	Technische Universiteit Delft, reservelid



Published by: Georg Götz

Printed by: Gildeprint, Enschede

ISBN: 978-90-8593-0778

Casimir PhD Series, Delft-Leiden, 2010-14

Copyright © 2010 by Georg Götz

An electronic version of this thesis is available at [www.library.tudelft.nl/dissertations](http://www.library.tudelft.nl/dissertations)

# Preface

At the end of my studies, I had no clue what experimental research really was like; studies at ETH Zürich were mainly theoretical (especially, since I am one of the “old guys”, that did not have to do a Bachelor project). But during my diploma project, I experienced how exciting it can be to work on your own experiment in a lab. I was sure, I wanted to continue on this path. So I started to search for a PhD project. Having looked at several places, I decided to come to the Quantum Transport group in Delft. The quality of research in QT was famous and the research projects sounded very exciting. And, equally important, there seemed to be a very cooperative and friendly atmosphere in this group, which hosted people from all over the world.

So in 2006, I started my work on Carbon Nanotubes here in Delft. The long-term goal was to build spin-qubits in carbon nanotubes, possibly with longer spin coherence times than in other semiconducting quantum dot systems. It was not completely clear how exactly to do this, but there were some promising ideas and we started to implement them in real experiments. During my first year, I also got to know *the other side of science*: Nothing was really working out for us, samples got destroyed at every stage of fabrication, measurements did not show the results we expected. But almost exactly after one year, we started having success with our work and obtaining the results, presented in this thesis. Looking back, I can say that carbon nanotubes are a challenging but extremely exciting and many-sided topic to work on.

First, I would like to thank my advisor, Leo Kouwenhoven. Your insight in physics and intuition for the relevant experiments are a great guidance for a student. Your trust to let me present our work to the outside and to take my own decisions from the beginning was very motivating. At the same time, you always stayed positive and came up with some alternative path when experiments were not going as expected. Also, it was great to see you back again on the football field last year!

This research would not have been possible without the help of many collaborators from QT and outside. First of all, I would like to thank Gary, postdoc of

the QT Nanotube-team and advocate of *ultra-clean* CNTs. We spent more than four years of Nanotube-research together and I learned a lot from you: Fabrication, low-noise measurement techniques, operating a dilution fridge, assembling a measurement setup and much more. Only your *spyview* habits, I did not really adopt. I wish you all the best for your family and good luck with setting up your own research group! Pablo and Sami, thanks a lot for introducing me to the world of carbon nanotubes and the crash-course during my first 6 months in QT. I always enjoyed the discussions about the theory side with Björn, Patrick and Fabian from Leiden as well as with Yuli from upstairs. From the MED and MB groups here in Delft, I would like to mention Herre van der Zant, Andreas, Benoit, Christian, Mascha and Iddo. For the collaboration on the  $^{13}\text{C}$  - project, I thank Prof. Daniel Loss for the idea and Prof. Charlie Marcus and Hugh Churchill for the samples (also for the ALD in 2007!) and discussions. Marc, Marco and Roel from the Delft Nanofacility helped a lot with countless fabrication issues during the last years. We had two temporary guests in our team: Marcus (thanks for showing me the Finnish center in Rotterdam) and Salvo (“Mr. cleanroom”), it was great to have you here! I also was supervisor of two Master students, Diego and Willem-Jan. I really appreciated your contributions! Now, there are two new people continuing the nanotube transport project: Edward (bringing British accent to QT) and Tang; I am sure you will have a lot of success!

QT is not only a great place to do research but I also enjoyed many social activities and events during the past years. Hans Mooij, it is impressive how you have built such a great place for research and how many outstanding research groups have emerged from your group. Also many thanks to the other staff members who form the “frame” of QT: Lieven, Ronald, Kees and Ad.

During my PhD, I spent a lot of time inside and outside the TU with the inhabitants of the “QT house”, who all started their PhDs around the same time as me: Pol, I really enjoyed all the football games, on the field as well as in front of a TV or at the Amsterdam Arena! Umberto, I remember a lot of interesting movies (*Calvaire* is still the highlight) and discussions. Katja (thanks for all the advice about the last steps of a promotion) and Lan (I am sorry that I don't like any Chinese food except *Beijing duck*), thanks for organizing countless BBQs! My office was not only a pleasant place to work, but also for non-scientific discussions. Thanks to Han (who finally also “arrived” at the nanotubes), Stevan (who also was my housemate for 2 years) and Victor. With Juriaan, Maarten and Maarten, I shared the experience of writing up a thesis and facing the related obstacles (to get from PROM-01 to PROM-06). Having similar systems, goals and problems, I had a lot of interaction with the Nanowire-team, Stevan, Juriaan and Sergey; the “wires and tubes” have been a really nice group! Amelia and

---

Stijn, good luck with the unfolded nanotubes! Gilles and Maria, I hope you will see a lot of nanotube-photons! Reinier and Wolfgang, good luck with building futuristic devices! The GaAs-team has set a high standard for spin-qubits; Lars, Floris and Mohammad, I am sure you will continue on that track. I played a lot of Friday-afternoon football games with Floor, Floris Z., Pol, Lan, Stijn, Ewan, Yvonne, Thomas, Tomoko and many others. During my PhD, I had the opportunity to visit some great conferences. I remember interesting discussions with Shahal Ilani, Carola Meyer, Vikram Deshpande and many others; Hubert, thanks for Strassbourg! There are not only scientists in QT: Yuki, Angele and Ria, thanks for administrative support. Bram, during four years I have not encountered one technical problem, you would not find a solution to! Also many thanks to Remco and Peter. Many experiments in QT would not be possible without Raymond Schouten, our electronics wizard. From ETHZ, I would like to thank Klaus Ensslin and Renaud Leturcq for supervising my Diploma-thesis. Finally, I wish all the other PhD-students and post-docs from QT a lot of success with their projects; it has been a great time for me in QT!

Although I was very busy during the last years, I am happy I am still in touch with friends from Hamburg and Zürich. Beni (thanks for your advice on the *life after physics*) and Hesham (remember the *Mexican flag?*), I remember many Sunday-afternoon cooking sessions and beers at the Limmat! Flo and Sebastian, it was always nice to meet you back in HH.

Finally, I would like to mention the people that are most important to me: I thank my parents and my brother for their love and their confidence in me; every time I was back in Hamburg, I always felt at home immediately! Kata, thanks for all the time we spent together and your love and support. Nagyon szeretlek!

Georg Götz  
May 2010





# Contents

<b>Preface</b>	<b>5</b>
<b>1 Introduction</b>	<b>13</b>
1.1 Nanoscience and Nanotechnology . . . . .	13
1.2 Carbon Nanotubes . . . . .	14
1.3 Outline . . . . .	15
<b>2 Carbon Nanotubes and single electrons</b>	<b>17</b>
2.1 Carbon nanotubes . . . . .	17
2.1.1 The crystallographic structure of carbon nanotubes . . . . .	17
2.1.2 The electronic band structure of carbon nanotubes . . . . .	18
2.1.3 Small bandgap CNTs . . . . .	24
2.1.4 Spin-orbit coupling and the symmetries of the spectrum . . . . .	26
2.2 Longitudinal quantization: Quantum dots . . . . .	28
2.3 Pauli blockade and spin qubits . . . . .	31
2.3.1 The effect of K-K' degeneracy . . . . .	32
2.3.2 Singlet-triplet splitting and Wigner molecules . . . . .	35
<b>3 Fabrication</b>	<b>41</b>
3.1 Electron beam lithography . . . . .	42
3.2 SET fabrication . . . . .	44
3.3 Carbon nanotube growth . . . . .	45
3.4 Etching of silicon structures . . . . .	47
3.5 Fabrication of narrow gates for clean, suspended CNT devices . . . . .	48
3.6 Room temperature characterization . . . . .	50
<b>4 Charge detection with single electron transistors</b>	<b>53</b>
4.1 Charge detection in CNT-QDs . . . . .	53
4.2 Aluminium single electron transistors . . . . .	54
4.3 Sensitivity . . . . .	56
4.4 Experimental demonstration . . . . .	59

4.4.1	Noise and sensitivity . . . . .	60
4.4.2	Active feedback . . . . .	61
4.4.3	Quantum dots at the end of a CNT . . . . .	62
<b>5</b>	<b>Coupling effects between a carbon nanotube quantum dot and a SET charge detector</b>	<b>65</b>
5.1	Introduction and device . . . . .	66
5.2	Backaction effects . . . . .	66
5.3	Mechanisms . . . . .	69
<b>6</b>	<b>Real time electron tunneling and pulse spectroscopy in carbon nanotube quantum dots</b>	<b>73</b>
6.1	Introduction and device fabrication . . . . .	74
6.2	A tunable CNT QD with a SET charge detector . . . . .	76
6.3	Real time charge detection . . . . .	78
6.4	Pulse spectroscopy . . . . .	78
6.5	Upper bound for the spin relaxation time $T_1$ . . . . .	82
<b>7</b>	<b>Tunable few-electron double quantum dots and Klein tunnelling in ultra-clean carbon nanotubes</b>	<b>85</b>
7.1	Introduction and device fabrication . . . . .	86
7.2	Single quantum dots defined by p-n junctions . . . . .	88
7.3	Few electron double quantum dots . . . . .	89
7.4	Klein tunneling . . . . .	91
7.5	Supplementary information . . . . .	96
<b>8</b>	<b>Towards local gate control over clean, as-grown carbon nanotubes</b>	<b>103</b>
8.1	A tunable triple quantum dot . . . . .	104
8.1.1	Stability diagrams . . . . .	106
8.2	Towards spin-manipulation . . . . .	108
8.2.1	Electron-electron interactions . . . . .	108
8.2.2	Electro-mechanical coupling . . . . .	109
8.2.3	Schemes for coherent spin manipulation . . . . .	109
<b>A</b>	<b>Pulse scheme to measure <math>T_1</math>, using an averaged charge detector signal</b>	<b>111</b>
A.1	The pulse scheme . . . . .	112
A.2	The rate equations . . . . .	113
A.3	Finding $W = 1/T_1$ . . . . .	114

## CONTENTS

---

<b>Bibliography</b>	<b>117</b>
<b>Summary</b>	<b>127</b>
<b>Samenvatting</b>	<b>129</b>
<b>Curriculum Vitae</b>	<b>133</b>
<b>Publications</b>	<b>135</b>



# Chapter 1

## Introduction

### 1.1 Nanoscience and Nanotechnology

The research described in this thesis has been carried out at the *Kavli Institute of Nanoscience* at Delft University of Technology. *Nanoscience* and *Nanotechnology* have become extremely popular terms in the world of science (and beyond) during the last one or two decades [1, 2]: There are institutes of Nanoscience, scientific journals dedicated to Nanotechnology and new study programs at universities. But is Nanoscience really a new scientific discipline?

*Nanoscience* and *Nanotechnology* deal with objects which are, at least in one dimension, of nanometer size. This means these objects approach the size of single or a few molecules. But this alone does surely not justify to call Nanoscience a new scientific discipline. What is crucial is that for objects of the size of a few nanometers, many properties require a fully quantum mechanical description. This is, because the quantum mechanical wavelength of electrons in the object now starts to become comparable to the object size. Another characteristic of Nanoscience is that at the length scale of single molecules, the traditional boundaries between the classical scientific disciplines Physics, Chemistry and Biology start to break down. Doing Nanoscience, it is possible to trace back many biological or chemical properties to the laws of Physics.

Nanoscience can be found in almost any area of science and technology: fundamental physics, electrical engineering, genetics, process engineering or pharmacy, just to name a few. In Physics, one of the most important aspects of Nanotechnology is the possibility to manufacture devices that are tailor-made to investigate one particular effect. E.g. in a quantum dot, which is often also called an *artificial atom*, it is possible to systematically investigate the energy spectrum and interactions of a well-defined number of confined electrons in a controlled and adjustable environment.

Another important line of research is the development of new electronic, mechanical and optical devices. On the one hand, commercial state-of-the-art electronic devices are nowadays approaching the borderline to Nanotechnology, such that understanding and controlling quantum mechanical effects becomes inevitable. On the other hand, in the regime of non-classical physics, entirely new types of devices become possible. Two prominent examples are *quantum cryptography* and the *quantum computer*.

But in the field of Physics there are no fundamentally new concepts related to *nano*. However, thanks to Nanotechnology, an entirely new world of experiments has become accessible for physicists now. Many of the classic, text-book examples of quantum mechanics can today be realized “on chip” and measured in the lab. Besides the technological implications this opens the door for a better and deeper understanding of existing concepts in Physics.

## 1.2 Carbon Nanotubes

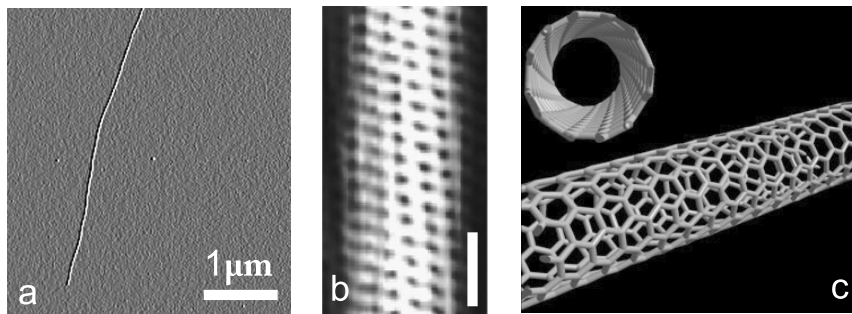


**Figure 1.1: Carbon Nanotubes** (a) Atomic force microscopy image of a CNT on a  $\text{SiO}_2$  surface. (b) Scanning tunneling microscopy image of a CNT, resolving the atomic structure. The scale bar is 1 nm. (from ref. [3]). (c) The structure of a single-wall CNT (schematic).

Carbon nanotubes (CNTs) are often named as *the* paradigm for an object in Nanotechnology. They are small hollow cylinders made out of carbon atoms, arranged in a hexagonal lattice structure. In fact, a single-walled CNT (the cylinder wall consists of a single layer of carbon atoms) is one large molecule. CNTs measure only a few nm in diameter and possess remarkable electrical and mechanical properties. Since their discovery in 1991 [4] (single-wall CNTs: 1993 [5]), CNTs have been used for many fundamental experiments (concerning e.g. quantum dots, electron-electron interactions in 1D, the Kondo effect or super-

conductivity) as well as for new devices (biosensors, scanning probe microscopy tips, water filters and many more).

In this thesis, we are interested in the electrical properties of single-wall CNTs at low temperatures. Besides fundamental physics, this research area is interesting for new types of electronic devices, such as spin based quantum information processing. During the last 10 years, a lot of research has been carried out on the electronic properties of CNTs. But new exciting results just keep appearing. One reason for this is the great progress in device fabrication that still is being made. CNT-QDs have become more tunable (work on tunable tunnel barriers and charge detection has made great progress during the last years) and also it has been possible to reduce disorder in these devices. A number of research groups is today able to fabricate CNT-QDs in the few electron regime. But there are still many open questions to answer: What is the exact role of electron-electron interactions at low carrier densities? Can spin-orbit interaction be used for spin-based quantum information processing? Is it possible to cool the mechanical vibrations of a CNT by means of an electrical current? And these are just a few examples, there is much more to investigate.

### 1.3 Outline

The outline of this thesis is as follows:

In **Chapter 2** we explain the basic properties of CNTs, with the focus on electronic properties and QDs. The discussion includes both theoretical concepts as well as fundamental experimental results.

**Chapter 3** gives an overview of the fabrication of QD devices in CNTs. Techniques to fabricate top-gate devices with a charge detector as well as methods to obtain very clean CNT-QDs are presented here.

In **Chapter 4, 5 and 6** we present experiments on a CNT-QD coupled to a charge detector. The charge detector is a metallic single-electron transistor (SET) which is sensitive to single electrons on the CNT-QD. We start by demonstrating the principle of charge detection with a simple CNT-QD, followed by a discussion of backaction effects. It appears that backaction from the SET to the CNT is small and that the SET is sensitive to the noise in the current through the CNT, as well.

Finally, we use charge detection to investigate real-time electron tunneling on extremely long timescales, showing the stability and tunability of gate-defined QDs in CNTs. Also, we perform excited state spectroscopy on isolated CNT-QDs.

In **Chapter 7** we present measurements on very clean, suspended CNT-QD devices. These devices have been fabricated with a scheme that aims at minimizing disorder in the CNTs. Both single and double QDs are shown to reach the few-electron regime. P-n junctions are used to create tunable tunnel junctions inside the CNT. In small bandgap CNTs, we are able to investigate a process that is similar to Klein tunneling in relativistic quantum mechanics.

**Chapter 8** describes the status of experiments aiming at combining clean, suspended CNTs with local (electrical) gates. We use a device with five local gates underneath a clean CNT to create a tunable triple QD in the few-electron regime. At the end, we discuss the future of these devices for experiments on spin manipulation in CNTs.



# Chapter 2

## Carbon Nanotubes and single electrons

### 2.1 Carbon nanotubes

Carbon is the sixth element of the periodic table and belongs to the group IV which means it has four electrons in its outer shell. It has the remarkable property that it can form stable objects of three dimensions (graphite, diamond), two dimensions (graphene), one dimension (CNTs) and zero dimensions (carbon molecules, such as fullerenes). In this thesis, we are interested in its one dimensional form, CNTs [4, 6, 7]. They can be described as carbon atoms forming a hexagonal lattice, wrapped up to a hollow cylinder (figure 2.1 a). A single-wall CNT has a diameter of 1 - 5 nm and a length between 100 nm and 1 cm. On the length scale of a unit cell CNTs are still three dimensional objects (as in fact anything in this world is a three dimensional object). However, already on a length scale of a few 100 nm, CNTs can be described as one dimensional objects very well.

#### 2.1.1 The crystallographic structure of carbon nanotubes

To discuss the electronic band structure of CNTs [8] we start with the band structure of graphene and then deduce the electronic properties of CNTs. But first we look at the crystallographic structure (for a more detailed review, see e.g. [9] or [10]). A single sheet of carbon atoms is called graphene. The atoms are arranged in a hexagonal structure with a lattice constant of  $a \simeq 0.25nm$ . A hexagonal structure can be described as a triangular lattice with a two atom basis (A and B). The two lattice vectors are  $\vec{a}_1$  and  $\vec{a}_2$  (figure 2.2). This means, any atom in the graphene lattice can be reached by an integer combination of these two vectors, starting from either atom A or B. The reciprocal lattice is also a triangular lattice (with lattice vectors  $\vec{b}_1$  and  $\vec{b}_2$ ).

Now we construct a CNT from a sheet of graphene. This is not the way CNTs are made in reality but a very useful way of describing their electronic and crystallographic structure. Graphene can be rolled up to a cylinder in many different ways. We pick an arbitrary carbon atom and define it to be our origin,  $(0,0)$ . We choose a second point of the lattice (which we can reach by an integer combination  $n\vec{a}_1 + m\vec{a}_2$  of unit vectors from the origin) and label this point  $(n,m)$ . Furthermore, one chooses (without loss of generality)  $n \geq m$ . The vector  $\vec{C}$  connecting  $(0,0)$  and  $(n,m)$  is called the wrapping vector. The graphene sheet is wrapped up to a cylinder such that the atoms  $(0,0)$  and  $(n,m)$  are on top of each other and the CNT axis points along the direction perpendicular to  $\vec{C}$ . This is called a  $(n,m)$  CNT or also a CNT with chirality  $(n,m)$  (figure 2.1 b). We have to mention that for the way we fabricate CNTs (CVD growth, see chapter 3 for details) there is no control over the chirality of our CNTs. We get CNTs with a certain diameter distribution but within this distribution all chiralities are probably distributed equally.

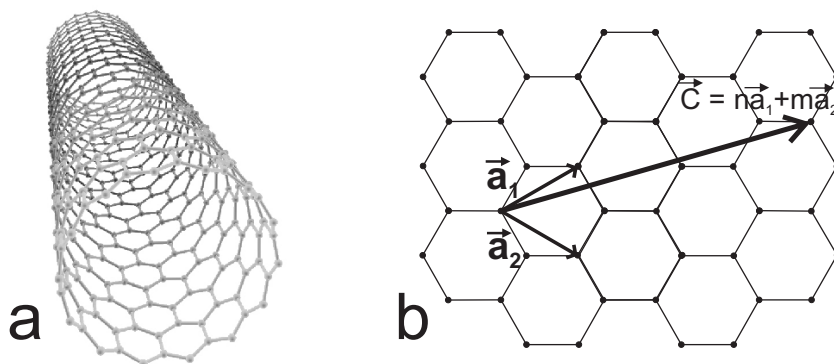


**Figure 2.1: Carbon nanotubes** (a) Carbon nanotubes are hollow cylinders, formed by a hexagonal structure of carbon atoms. (b) A CNT is constructed from a graphene sheet. The wrapping vector  $\vec{C}$  is wrapped onto itself, thereby generating a CNT. The axis of the CNT is pointing perpendicular to  $\vec{C}$ .

### 2.1.2 The electronic band structure of carbon nanotubes

The electronic band structure of graphene [11] is our starting point for understanding the band structure of CNTs. Again, we refer to [9] and [10] for a more detailed description. Each carbon atom has four electrons in its outer shell. Three of them occupy the  $sp^2$  orbitals, forming bonds to its three neighboring atoms. The last valence electron occupies the  $p_z$  orbital (which is oriented perpendicular to the graphene plane) and mixes with the  $p_z$  states of the other atoms in

the lattice, thereby forming delocalized electron states, so called  $\pi$ -bonds. Only these states contribute to the electric conductivity because their energy is located around the Fermi energy ( $E_F$ ).

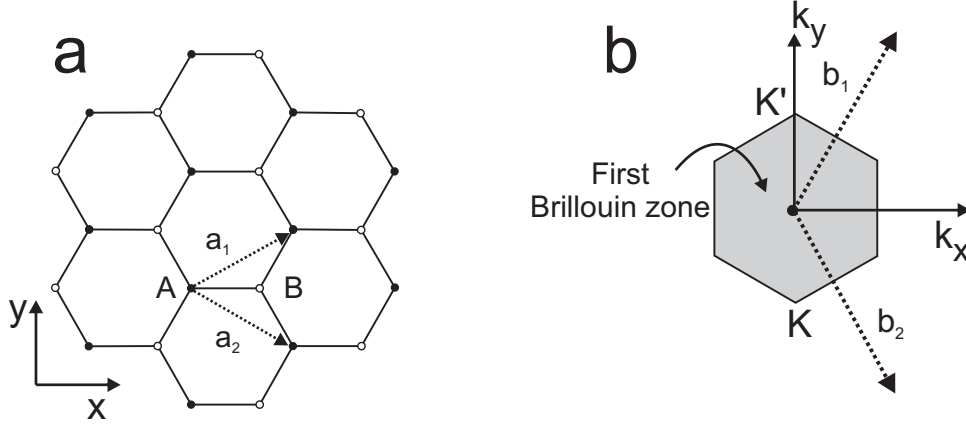


**Figure 2.2: Real space lattice and reciprocal lattice** (a) The real space lattice of graphene and its two lattice vectors. Each unit cell hosts two atoms, A and B. (b) Reciprocal space lattice. The first Brillouin zone is hexagonal and has two inequivalent corner points, K and K’.

To discuss the band structure we take a look at the reciprocal space lattice (figure 2.2b). The first Brillouin zone is hexagonal. Conductance and valence band touch each other at a discrete set of points which coincide with the corners of the first Brillouin zone. These special points are called “K points”. The Fermi surface consists of only these K points. Of the six K points in the first Brillouin zone only two are inequivalent. These two points are called K and K’. The dispersion  $E(k_x, k_y)$  around the K points is conical, i.e. linear in  $|\vec{k}|$ . Graphene is a semimetal or zero bandgap semiconductor. Its bandstructure is summarized in figure 2.3.

What happens to the dispersion if we wrap up graphene to a CNT? Let us consider a coordinate system for  $\vec{k}$ , with its two components pointing along and around the CNT axis:  $\vec{k} = (k_{\parallel}, k_{\perp})$ . This coordinate system is rotated with respect to the  $(k_x, k_y)$  coordinate system by an angle  $\theta$  which depends on the CNT chirality. While  $k_{\parallel}$  is still continuous,  $k_{\perp}$  becomes quantized.

$$\pi dk_{\perp} = 2\pi i; i = 0, \pm 1, \pm 2, \dots \quad (2.1)$$

This means the dispersion relation of a CNT consists of discrete, equally spaced vertical planecuts through the dispersion relation of graphene, resulting

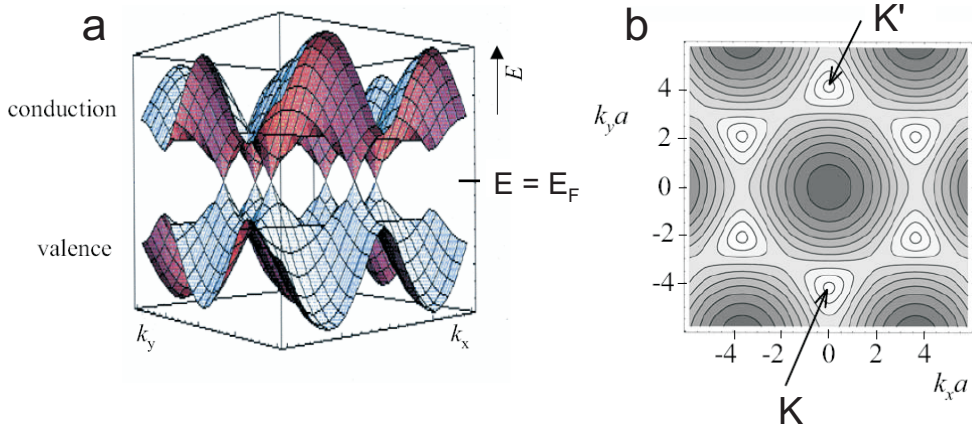


**Figure 2.3: The bandstructure of graphene** (a) The energy dispersion relation of graphene as a function of the wavevector  $\mathbf{k}$ . The Fermi surface consists of six points, the so called K-points. Around these points the energy dispersion is conical. (b) Contour plot of the valence states from (a). Lighter colors correspond to higher energies. Out of the six K-points two are inequivalent: K and K'. Figure adapted from [12]

in a set of one-dimensional subbands (figure 2.4). For the energy scales we are interested in, only the subbands next to K and K' are relevant (the energy of the following (second) subband is higher by about 1eV or 10000K). Now, if a subband exactly intersects with K (because of symmetry, then also a subband intersects with K'), there is no bandgap and the CNT is metallic. Otherwise, there is a finite bandgap and the CNT is semiconducting (figure 2.5). The nature of a CNT follows from its chirality by a simple rule: A  $(n,m)$  CNT is metallic if  $n - m = 3q$ , where  $q$  is an integer. Otherwise it is semiconducting, with a bandgap  $E_G$ , depending on its diameter [9]:

$$E_G = 2\gamma_0 a / (\sqrt{3}d) \simeq 0.8eV/d [nm] \quad (2.2)$$

Here  $\gamma_0 \approx 2.9eV$  is the transfer integral from the graphene tight binding model. Every longitudinal state is twofold degenerate because of the identical band structure around K and K'. This degeneracy, which is often called the “valley-degeneracy”, has a very intuitive explanation, since the origin of the discrete plane cuts is the quantization of  $k_\perp$ , the perpendicular component of the wavevector: One can talk about a state with an electron going clockwise around the CNT and another with an electron going counter-clockwise. Therefore, these states also possess an orbital magnetic moment [13]:  $\mu_{orb} = ev_F d/4 \simeq 0.2meV \times d [nm]$ , for electrons at the Fermi energy. Here  $v_F = \sqrt{3}/2 \times a\gamma_0/\hbar$  is

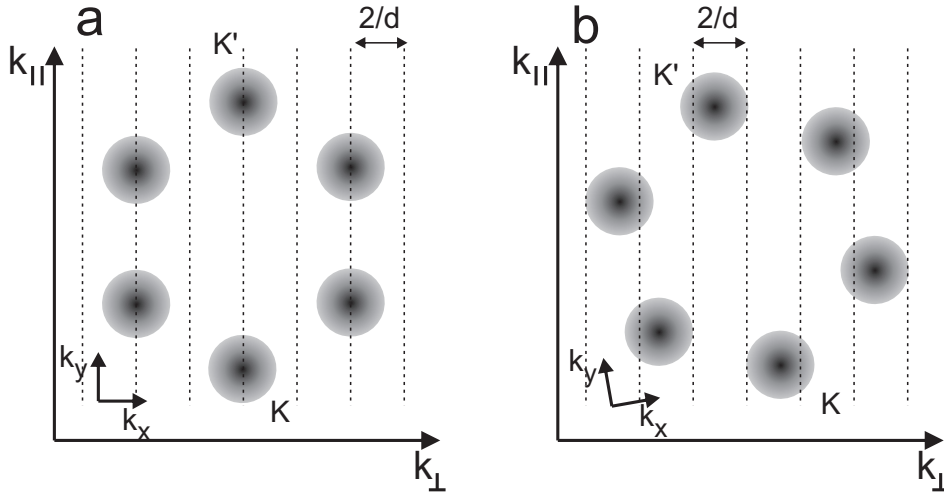


**Figure 2.4: Quantization of  $k_{\perp}$**  Top view contour plot of the graphene band structure in the first Brillouin zone (figure 2.3). Quantization of  $k_{\perp}$  defines equally spaced plane cuts through the graphene band structure. These plane cuts are the 1-D bands of the CNT band structure, as shown in figure 2.5. Note that the relative orientation of the  $(k_x, k_y)$  and  $(k_{\parallel}, k_{\perp})$  coordinate systems depends on the chirality. We have sketched the situation for zero parallel magnetic field. **(a)** Metallic CNT (armchair): a subband intersects with the K (and K') point. **(b)** Semiconducting CNTs: no subband intersects with the K (and K') point. The subbands which are closest to K and K' define the bandgap  $E_G$ .

the Fermi velocity of graphene. For a typical CNT with a diameter of a few nm  $\mu_{orb}$  is much larger than the spin magnetic moment.

### Magnetic field dependence of the band structure

An external magnetic field has a remarkable effect on the electronic states of a CNT (figure 2.6). For the moment we ignore the electron spin and only consider the orbital magnetic moment. In a magnetic field, equation 2.1 is modified to:

$$\pi d k_{\perp} + 2\pi\Phi/\Phi_0 = 2\pi i; \quad i = 0, \pm 1, \pm 2 \quad (2.3)$$

Here  $2\pi\Phi/\Phi_0$  is the so called Aharonov-Bohm flux, acquired by electrons traveling around the CNT circumference. It is related to  $B_{\parallel}$ , the magnetic field component pointing along the CNT axis, via  $\Phi = \pi d^2 B_{\parallel}/4$ .  $\Phi_0 = h/e$  is the magnetic flux quantum. This means the intersection planes from figure 2.4 will shift proportional to  $B_{\parallel}$  (figure 2.6). For a metallic CNT this just means that

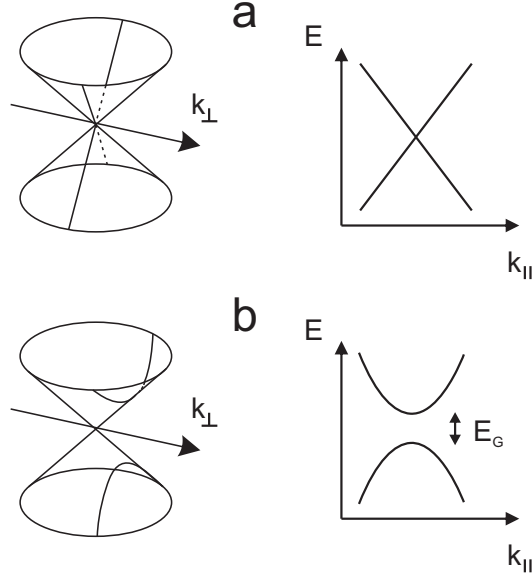


**Figure 2.5: Low energy spectrum of CNTs** (a) Metallic CNTs: There is a possible value of  $k_{\perp}$  whose subband passes exactly through K and therefore there is no bandgap. (b) Semiconducting CNTs: There is no subband passing through the K-points and therefore a finite bandgap exists. The vertical intersection of the cone defines a hyperbolic dispersion relation.

a band gap will open up and its magnitude increases linearly with  $B_{\parallel}$ . For a semiconducting CNT the situation is a bit more complicated. For one of the two symmetry points (let us say K') the bandgap will increase with magnetic field. However, for K the bandgap first decreases with  $B_{\parallel}$  until it is zero. For higher fields the bandgap for K then increases again. Eventually, if the zero field gap is small, one will observe the point where the bandgap vanishes for K at a field value achievable in the lab (see section 2.1.3). The different situations for metallic and semiconducting CNTs are shown in figure 2.6. The change of the bandgap with magnetic field depends on the CNT diameter:

$$\frac{dE_G}{dB_{\parallel}} = \frac{dE_G}{dk_{\perp}} \frac{dk_{\perp}}{dB_{\parallel}} = \pm 2 \frac{\sqrt{3}\gamma_0 a}{2} \frac{\pi e d}{2h} = \pm \frac{2ev_F d}{4} = \pm 2\mu_{orb} \quad (2.4)$$

To give an idea of this effect, for a CNT with  $d = 2nm$ ,  $E_G$  changes with a slope of  $dE_G/dB_{\parallel} = 0.8mVT^{-1}$ .

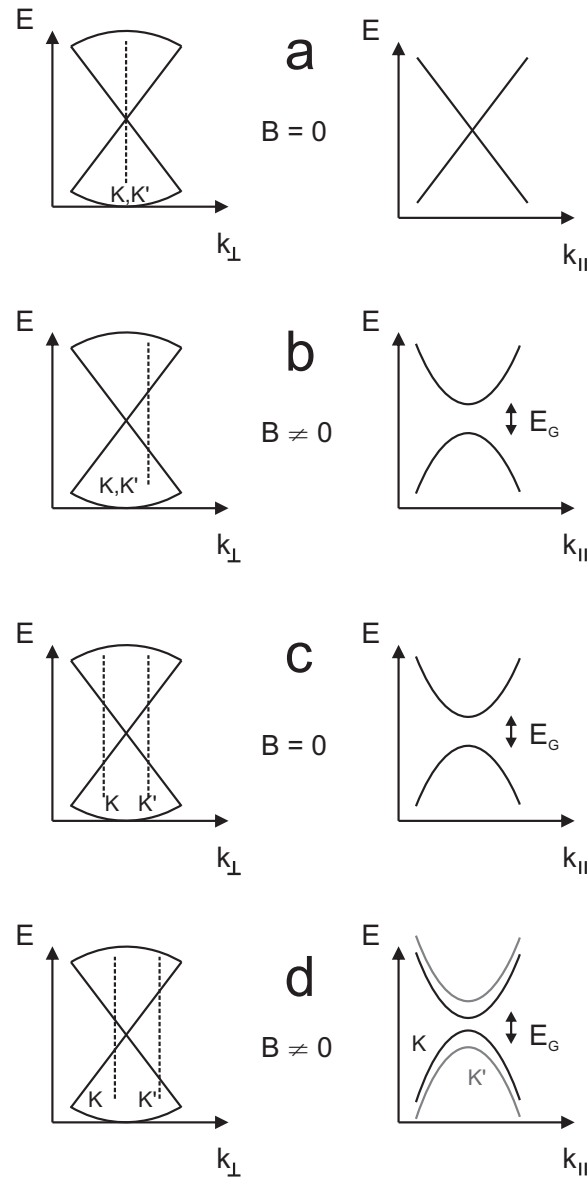


**Figure 2.6: Dependence of the band structure on the parallel magnetic field** On the left side, a schematic of the cone of the graphene band structure is shown. The vertical dashed lines indicate at which position of the cone the allowed quantized wavevector  $k_{\perp}$  of the first subband intersects (for both  $K$  and  $K'$ ). On the right side, the energy dispersion vs parallel wave vector  $k_{\parallel}$  is shown. (a) Metallic CNT (b) Metallic CNT, finite magnetic field: A bandgap opens up (c) Semiconducting CNT (d) Semiconducting CNT, finite magnetic field: for one  $K$ -point the bandgap increases, for the other  $K$ -point the bandgap decreases.

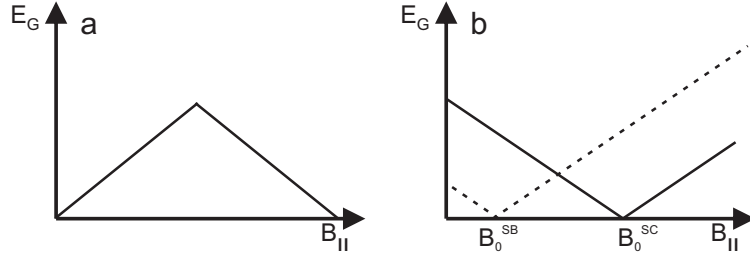


**Figure 2.7: Bandgap  $E_G$  as a function of parallel magnetic field** (a) Metallic CNTs: The bandgap increases linearly with  $B_{||}$  until the first subband gets further away from the K-points than the second subband. From this point on,  $E_G$  decreases again. K-K' degeneracy is maintained, even for finite magnetic field. (b) Semiconducting CNTs: The bandgap decreases with  $B_{||}$  until the first subband passes through the K-point. If  $B_{||}$  is increased further,  $E_G$  increases again. The field  $B_0$ , where  $E_G = 0$ , is huge for semiconducting (SC) CNTs ( $\sim 2000T$  for  $d = 1nm$ ), but can be on the order of a few T for small bandgap (SB) CNTs.

In figure 2.7, we summarize how the bandgap depends on parallel magnetic field for both metallic and semiconducting CNTs.

### 2.1.3 Small bandgap CNTs

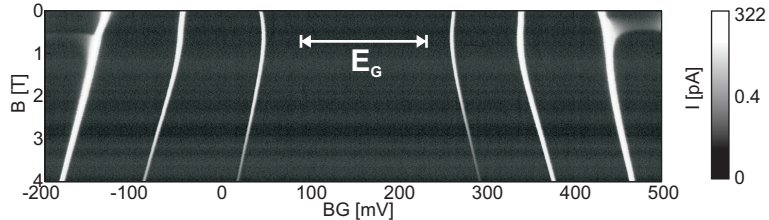


**Figure 2.8: Magnetic field dependence of the gap of a small bandgap CNT** Low temperature measurement of the current through a small bandgap CNT-QD. The first three electron and hole states are shown as a function of parallel magnetic field and applied back gate voltage (BG). The bandgap  $E_G$  (which can be estimated by subtracting half the addition energies of the first electron and first hole from the measured total gap between the first electron and first hole state) is minimal but clearly finite at  $B_0 \approx 0.75T$ . Using  $\alpha = 0.2$  (obtained from the charging energy of the first hole), we find - after subtracting the addition energy - a minimal bandgap of  $\sim 35meV$ .

As discussed above, for CNTs  $(n,m)$  with  $n - m = 3q$ , one expects that they



are metallic, i.e. have no bandgap. However, in reality <sup>1</sup> many CNTs have a small bandgap of typically  $10 - 50\text{meV}$  <sup>2</sup>.

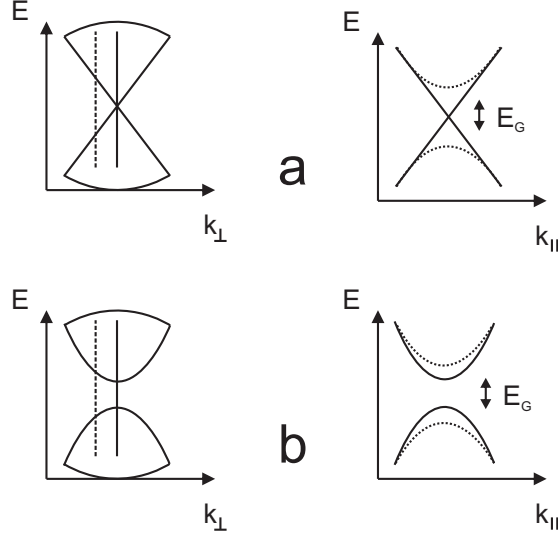


**Figure 2.9: Small bandgaps in CNTs** (a) Shift: If the quantized value of  $k_{\perp}$  misses the K-point by small amount (e.g. caused by mechanical deformations) there is a small bandgap at zero magnetic field (dashed line). The gap will be zero for some finite magnetic field  $B_0$  (solid line). (b) Interactions: If electron-electron interactions modify the bandstructure such that there is finite gap at  $E_F$ , the bandgap is nonzero at any magnetic field.

What is the origin of this gap? It is known that curvature [16, 17] and mechanical deformations such as strain [18] or twist [19] can create a bandgap of this magnitude. The mechanical deformations shift the positions of the K-points in k-space. This changes the magnitude of the bandgap. For metallic (non-armchair) CNTs, the quantized wave vector will now miss the K-points and therefore a small bandgap will exist (figure 2.9 a). For curvature induced bandgaps, the magnitude of this bandgap is proportional to  $1/r^2$  [16, 17]. For all these mechanical deformations, the K-K' degeneracy is maintained and conduction and valence bands still meet at single points in k-space [12]. Just the position of these points is shifted. Therefore, by applying a parallel magnetic field (which shifts the allowed quantized wavevector states in k-space) one should be able to return

<sup>1</sup>This observation has been reported by a number of groups (e.g. [14, 15]) and is also found by us; both for the clean, suspended CNTs and as well for CNTs deposited on a substrate.

<sup>2</sup>We know that these bandgaps do not correspond to CNTs that are semiconducting by chirality: The CNTs have a diameter of 1 - 4 nm; this would correspond to a gap of 200 - 800 meV for semiconducting chirality.

to zero bandgap for some field  $B_{\parallel} = B_0$  [12, 16].

However, for experimental data this is very often not the case: One finds that the minimal gap occurs at a magnetic field  $B_0 \neq 0$ , but this minimal gap remains finite (figure 2.8). So it seems that mechanical deformations alone cannot cause these observed small bandgaps. An explanation might be found by taking electron-electron interactions into account (section 2.3.2).

### 2.1.4 Spin-orbit coupling and the symmetries of the spectrum

Until now, we have treated the spin and valley (K-K') quantum numbers completely independently of each other. This means that the electronic states in a CNT are fourfold degenerate at zero magnetic field: Each state is twofold degenerate with respect to the valley (K and K') and each of these states can be occupied by a spin-up and a spin-down electron. The fourfold degenerate state splits into four states when a parallel magnetic field is applied, because of the magnetic moments related to spin and orbital quantum numbers (see also figure 2.12). Although this model has successfully described a number of experiments, it is inaccurate because it neglects spin-orbit interaction. Rather than discussing the detailed theory of spin-orbit interaction in CNTs, we discuss its form, its implications for the spectrum and the consequences for implementation of spin based quantum information processing in CNTs.

Spin-orbit interaction for atomic carbon is weak (spin-orbit splitting  $\Delta \sim 10meV$ ) because of its low atomic number, and is almost vanishing for graphene (because of the symmetries in the graphene lattice) [20]. However, there is a peculiar effect resulting from the curvature of CNTs.

It has been predicted [20, 22, 23] and confirmed experimentally [21] that the spin and orbital momenta of electrons in CNTs are coupled. The main findings are summarized in figure 2.10. For electrons, a parallel configuration of spin and orbital momenta is favored over an antiparallel configuration by an energy  $\Delta_{SO}$  at zero magnetic field. The spin-orbit splitting,  $\Delta_{SO}$ , depends only on the diameter:

$$\Delta_{SO} = 1.6meV/d [nm] \tag{2.5}$$

So, in fact the spectrum of a CNT is two-fold degenerate at zero magnetic field (thereby maintaining Kramers degeneracy) and the four states have a linear dependence on a parallel magnetic field, determined simply by their combined spin and orbital magnetic momentum. Spin-orbit coupling in CNTs can be described

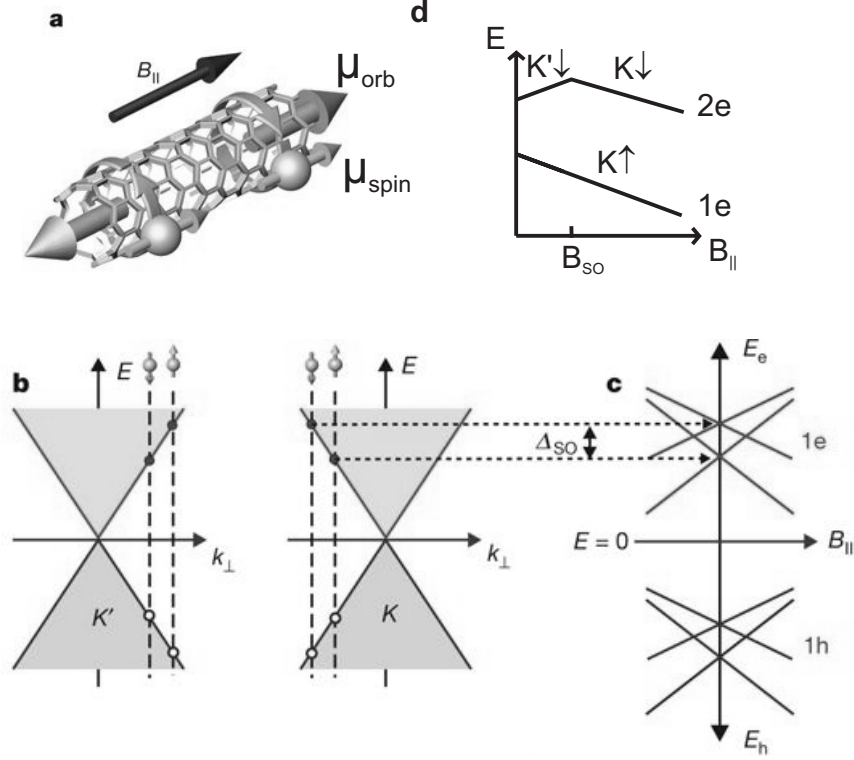


**Figure 2.10: Spin-orbit coupling in CNTs** (a) In CNTs, the spin couples to the valley. (b) Energies for spin-up and spin-down states for the two valleys K and K' at zero magnetic field. Spin-orbit interaction results in different allowed  $k_{\perp}$ -values for spin up and down. (c) Magnetic field dependence of the four states. The different slopes are given by the combined spin and orbital magnetic momenta of the states. (d) One and two electron ground states as function of magnetic field. The two electron ground state changes its valley at  $B_{SO}$ . (a)-(c) from [21]

by a spin-dependent topological flux,  $S_{\parallel}\Phi_{SO}$ , which modifies the quantization condition 2.1 for the transversal wave vector [21]:

$$\pi dk_{\perp} + 2\pi S_{\parallel}\Phi_{SO}/\Phi_0 = 2\pi i; \quad i = 0, \pm 1, \pm 2 \quad (2.6)$$

Here  $S_{\parallel} = \pm 1$  for the spin moment parallel/antiparallel to the orbital moment and  $\Phi_{SO} \approx 10^{-3}\Phi_0$  [22]. Spin-orbit coupling not only modifies the excited states of the first electron but is also visible in the ground state energies of multiple electron states. In particular, for the two electron ground state, the two electrons occupy different valleys below a characteristic field  $B_{SO}$ . Above  $B_{SO}$  the two electrons occupy the same valley (figure 2.10 d). This is observable by following

the two-electron ground state as a function of magnetic field. The magnitude of the spin-orbit field is given by

$$B_{SO} = \Delta_{SO}/2\mu_{orb} \simeq 4T/(d[nm])^2 \quad (2.7)$$

Experimental observation of the spin-orbit splitting is not easy and requires very clean samples since the observability of the spectrum shown in figure 2.10 can be masked by K-K' mixing [21]. Finally, it should be noticed that the spin-orbit coupling also breaks electron-hole symmetry because it favors for holes the opposite configuration (antiparallel spin and orbital momenta) than for electrons (figure 2.10). The presence of spin-orbit coupling opens up the possibility of all electrical coherent spin manipulation (EDSR) [24] in CNTs. A detailed proposal using spin-orbit coupling in bent CNTs and predicting Rabi frequencies of MHz up to GHz can be found in [25].

## 2.2 Longitudinal quantization: Quantum dots

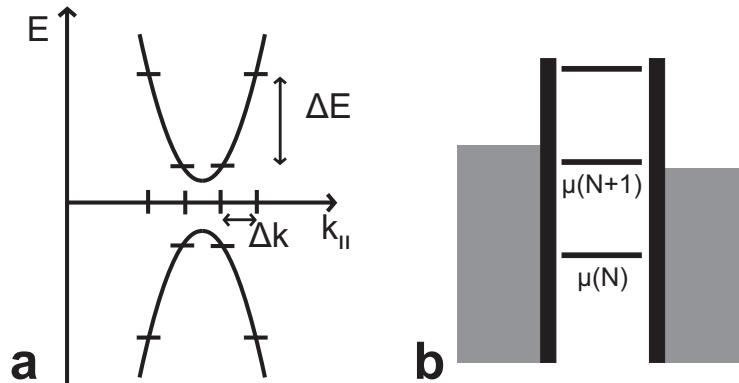


**Figure 2.11: Longitudinal quantization** (a) For a CNT with finite length, also the  $k_{\parallel}$  component of the wavevector becomes quantized. This leads to a quantized energy spectrum; a quantum dot (QD) is formed. (b) The addition energy of the QD is the sum of the charging energy and the quantum mechanical level spacing:  $\mu(N+1) - \mu(N) = E_C + \Delta E$ . Electron transport is only possible if the electrochemical potential,  $\mu$ , for adding an electron to the QD is inside the bias window (Coulomb blockade). The degeneracies of these quantized states in CNTs are discussed in figure 2.12.

Until now, we have assumed that the CNT is infinitely long and thereby forms a quasi one-dimensional system. Now we consider a small isolated section

of length  $L$ , coupled to leads by tunnel junctions. The leads can either be the left and right sections of a long CNT or a metal contact. The junctions can be formed by Schottky barriers at the metal-CNT interface [26, 27], p-n junctions inside the CNT (see chapter 7 of this thesis) or electrostatic barriers in the CNT (induced by the voltages on local gates) [28, 29]. Such a small section of a CNT forms a quantum dot (QD) [30].

The longitudinal confinement leads both to a considerable charging energy and to a discrete energy level spectrum. The quantized energy spectrum of a CNT-QD can be calculated from the Schroedinger equation for given confinement potential, electron number and CNT bandstructure. E.g. for a hard wall confinement, the wavevector along  $k_{\parallel}$  is quantized in steps of  $\Delta k_{\parallel} = \pi/L$ . If we assume a linear energy dispersion (metallic or small bandgap CNTs) we find for the energy level spacing:

$$\Delta E = \frac{dE}{dk_{\parallel}} \Delta k_{\parallel} = \frac{hv_F}{2L} \approx \frac{1.7meV}{L[\mu m]} \quad (2.8)$$

Despite its simplicity, this model describes many experiments surprisingly well. Different models include a harmonic confinement potential or electron-electron interactions (for instance by using a self-consistent electrostatic confinement potential) but the numeric values for the level spacing are very similar to the one found above [31]. Also, the charging energy might depend on  $N$ , the number of electrons on the CNT-QD.

The charging energy  $E_C$  is not directly related to the length of the CNT-QD but rather is inversely proportional to the total self-capacitance  $C_{\Sigma}$  of the CNT-QD.  $C_{\Sigma}$  depends not directly on  $L$  but on the capacitances to source, drain and gates (which depend on  $L$ ). However, the charging energy is in general larger for shorter CNT segments.

If  $\Delta E$  is larger than temperature (for CNT-QDs, this is already fulfilled at a few Kelvin) and tunnel coupling, this system is called a quantum dot. If only the charging energy is larger than temperature and tunnel coupling, one calls this a “single electron transistor” (SET). Electron transport through QDs and SETs is governed by Coulomb blockade, which we will not discuss here but refer to [32, 33] or [34] for an overview.

In figure 2.12, we show the first two orbital states in a QD, both for electrons and holes. We show the magnetic field dependence of these states both in a parallel and a perpendicular field. Also, the two situations with and without spin-orbit coupling are compared. Without spin-orbit coupling, each orbital state

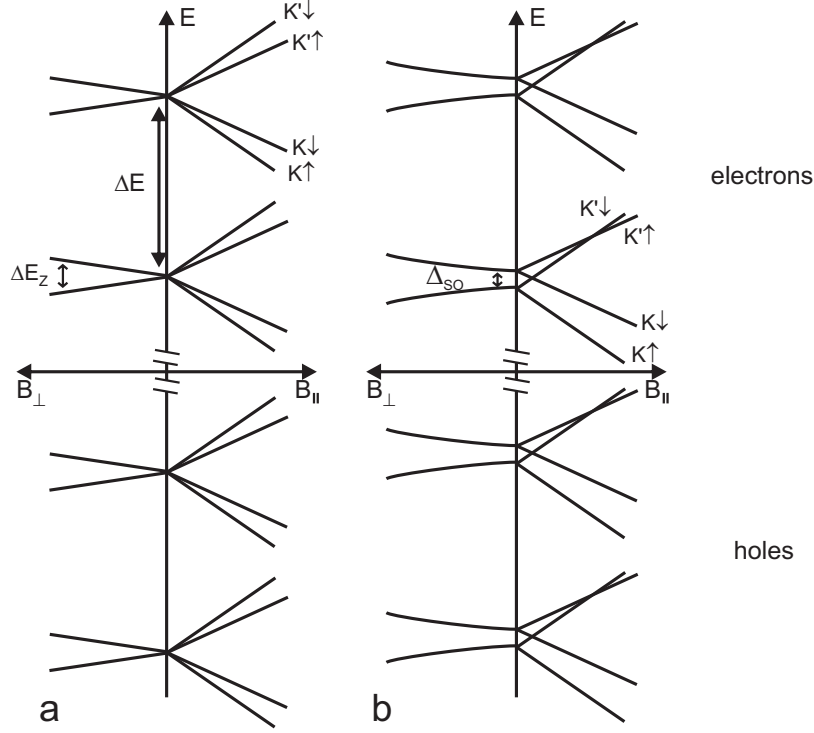


**Figure 2.12: First two electron and hole energy levels in a CNT-QD** On the left side of each diagram, the dependence of the states on a perpendicular magnetic field is shown, whereas the dependence on a parallel magnetic field is sketched on the right side. Sets of four states are split by  $\Delta E$ , the orbital level spacing resulting from the quantization along the CNT-axis. (a) No spin-orbit coupling. At zero magnetic field, each orbital state is fourfold degenerate. In case of a perpendicular magnetic field (left), K-K' degeneracy remains, while different spin states are split by the Zeeman energy  $\Delta E_z$ . In a parallel field, also the K- and K'-states split, according to their orbital magnetic moment (right). (b) With spin-orbit coupling. In a parallel magnetic field (right), we have the spectrum discussed in figure 2.10. Note that spin-orbit coupling breaks electron-hole symmetry. For a perpendicular field (left) there are two states which are twofold degenerate. They split nonlinearly in the perpendicular field, since  $B_{\perp}$  and  $B_{SO}$  are perpendicular to each other.

is fourfold degenerate at zero magnetic field. When a magnetic field is applied, these four states split, according to their spin and orbital magnetic momenta. Since the orbital magnetic moment only couples to a parallel field, a twofold degeneracy remains even at a finite perpendicular field.

Spin-orbit coupling splits each orbital state into two sets of twofold degenerate states at zero magnetic field, which are split in energy by  $\Delta_{SO}$ . In a parallel magnetic field, the slope of the four states is determined by their combined spin

and orbital magnetic moment. Even at finite parallel fields, spin-orbit coupling does not mix spin states since both spin-orbit coupling and external field lead to quantization of the spin in the direction along the CNT-axis.

In a perpendicular magnetic field, the states again remain twofold degenerate. However, in contrast to the case without spin-orbit coupling, the energy dependence on a perpendicular field is not linear. This is, because  $B_{\perp}$  and  $B_{SO}$  are perpendicular to each other. The splitting is in this case given by  $\Delta E_Z = 2g\mu_B\sqrt{B_{\perp}^2 + B_{SO}^2}$ . Now, spin states are mixed by spin-orbit coupling, since  $B_{\perp}$  points perpendicular to the CNT-axis while (the valley-dependent)  $B_{SO}$  points parallel to the CNT-axis. The nonlinear splitting as a function of magnetic field could also explain the findings of a reduced g-factor in few electron CNT-QDs [27] since these results were obtained under the assumption of a linear Zeeman splitting.

We conclude this section, summarizing the most important parameters for CNTs-QDs.

Symbol	numeric value	description
$a$	$2.46\text{\AA}$	graphene lattice constant
$v_F$	$8 \times 10^5 m/s$ [9]	Fermi velocity of graphene
$E_G(d)$	$0.8eV/d[nm]$	Semiconducting bandgap as a function of CNT diameter
$\mu_{orb}(d)$	$\pm 0.2meV/T \times d[nm]$	orbital magnetic moment
$\Delta E(L)$	$1.7meV/L[\mu m]$	Longitudinal level spacing (metallic CNTs, hard wall confinement)
$\Delta_{SO}(d)$	$1.6meV/d[nm]$ [20, 21]	Spin-orbit splitting

**Table 2.1: Carbon nanotube parameters and constants**

## 2.3 Pauli blockade and spin qubits

CNTs have been proposed as a promising material for devices in spin based quantum information processing. The main reason for this is that CNTs containing only  $^{12}C$  (and therefore no nuclear spins) can be fabricated. Thereby, the main source of spin decoherence in QD systems [35, 36, 37, 38] would be eliminated. However, in CNTs there are other issues that may cause difficulties for spin based quantum devices.

A key tool for investigating and probing the physics of a single, confined electron

spin is Pauli blockade (sometimes also called spin blockade)[39], as shown in figure 2.13. In a double QD the transition from a (1,1) triplet to a (0,2) triplet is blocked, since the Pauli exclusion principle for the (0,2) triplet requires a higher orbital to be occupied. This has usually a much higher energy and is therefore inaccessible. Spin blockade can be lifted by transforming a (1,1) triplet into the (1,1) singlet (the transition to the (0,2) singlet is energetically possible) and is thereby a tool to probe spin states in QDs.

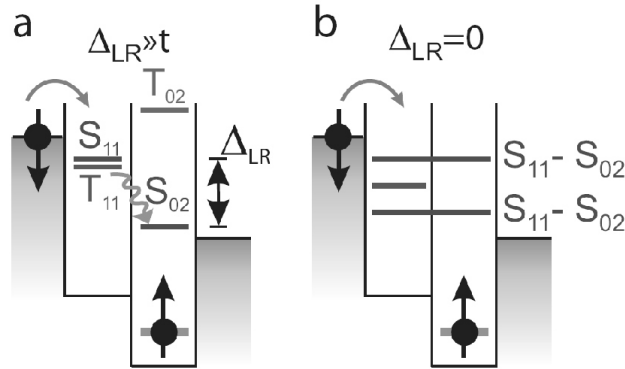


**Figure 2.13: Spin blockade in QDs** (a) Spin blockade for finite detuning  $\Delta_{LR}$ . Only from the (1,1) singlet ( $S_{11}$ ) an electron can tunnel to the (0,2) singlet ( $S_{02}$ ). The transition from the (1,1) triplets ( $T_{11}$ ) to the (0,2) triplets ( $T_{02}$ ) is energetically not possible. For the (0,2) triplets, a higher orbital must be occupied to maintain the overall antisymmetry of the wavefunction. (b) For zero detuning the (1,1) and (0,2) singlets hybridize. The triplets remain blocked. Figure from [40]

We discuss two particular aspects of this effect in CNTs: The role of the additional valley (K-K') degeneracy and the singlet-triplet splitting in CNTs.

### 2.3.1 The effect of K-K' degeneracy

As discussed above, there is an additional quantum number in CNT-QDs compared to other QD systems: an electron can occupy a state belonging to either of the two K-points. This is called the valley- (or isospin-) degeneracy. Let us neglect spin-orbit coupling for the moment. If we consider only the lowest longitudinal modes, there are 16 possible states for the separated (1,1) configuration (instead of 4, if there was only spin and no valley) [41, 42]. These states are listed in table 2.2. Which of these states can evolve into the (0,2) configuration (we



assume that interdot tunneling conserves spin and valley) without occupying a higher longitudinal mode? To answer this question, one has to look at the symmetry of these states under exchange of the two electrons. The Pauli exclusion principle requires that the total wavefunction for two electrons is antisymmetric under exchange. The total wavefunction is the product of a spin, a valley and an orbital part:

$$\Psi = \Psi_{spin} \otimes \Psi_{valley} \otimes \Psi_{orbital} \quad (2.9)$$

Therefore, if the combined spin and valley part of the wavefunction is symmetric, the (longitudinal) orbital part has to be antisymmetric - a requirement that in the (0,2) configuration can only be met if also the next higher (longitudinal) orbital is occupied. One finds that 10 out of the 16 states must have an antisymmetric orbital part of the wavefunction (table 2.2) and therefore their transition from (1,1) to (0,2) is blocked [41, 42, 43].

How can the blockade be lifted? If either the spin or the valley part of the wavefunction changes its symmetry, the combined spin and valley wavefunction changes its symmetry and both electrons can access the same orbital state and (0,2) is accessible. Therefore, either a “spin-flip” or a “valley-flip” can lift the spin blockade. A detailed theoretical discussion of this “spin-valley blockade” can be found in [43].

Now let us consider spin-orbit coupling. At zero magnetic field the states  $K \uparrow$  and  $K' \downarrow$  are lower in energy by  $\Delta_{SO}$  compared to  $K' \uparrow$  and  $K \downarrow$ . Let us first look at the situation where electrons only occupy the lowest energy states. Then, we have four possible (1,1) states, comparable to the usual spin blockade situation (table 2.3, states 1-4). Out of these four states only the antisymmetric one can evolve into (0,2). To lift spin blockade (and staying within the lowest energy states), both spin and valley have to flip.

It might be more realistic to consider all four single electron states, although they are not degenerate. In a typical spin blockade experiment in a double QD, a bias much larger than  $\Delta_{SO}$  is applied. If we take this into account we have again 16 possible states, 6 of them having an antisymmetric spin and valley part of the wavefunction (table 2.3).

Now we discuss the situation where a parallel magnetic field  $B_{\parallel} \gg B_{SO}$  is applied. Here the states  $K \uparrow$  and  $K \downarrow$  are the only ones we need to consider (they are much lower in energy than  $K' \uparrow$  and  $K' \downarrow$ ). This means we are in a situation, equivalent to the “conventional” spin blockade, without any effect from the valley quantum number: The spin singlet can evolve from (1,1) to (0,2) while the three triplets are blocked in (1,1). Spin-orbit coupling can facilitate spin relaxation [23]

	spin $\otimes$ valley	symmetry
1	$(\uparrow\downarrow - \downarrow\uparrow)(KK)$	-1
2	$(\uparrow\downarrow - \downarrow\uparrow)(K'K')$	-1
3	$(\uparrow\downarrow - \downarrow\uparrow)(KK' - KK')$	-1
4	$(\uparrow\uparrow)(KK' - K'K)$	-1
5	$(\downarrow\downarrow)(KK' - K'K)$	-1
6	$(\uparrow\downarrow + \downarrow\uparrow)(KK' - K'K)$	-1
7	$(\uparrow\uparrow)(KK)$	+1
8	$(\uparrow\uparrow)(K'K')$	+1
9	$(\uparrow\uparrow)(KK' + KK')$	+1
10	$(\downarrow\downarrow)(KK)$	+1
11	$(\downarrow\downarrow)(K'K')$	+1
12	$(\downarrow\downarrow)(KK' + KK')$	+1
13	$(\uparrow\downarrow + \downarrow\uparrow)(KK)$	+1
14	$(\uparrow\downarrow + \downarrow\uparrow)(K'K')$	+1
15	$(\uparrow\downarrow + \downarrow\uparrow)(KK' + K'K)$	+1
16	$(\uparrow\downarrow - \downarrow\uparrow)(KK' - K'K)$	+1

**Table 2.2: Two-electron states (without spin-orbit coupling)** Spin and valley part of two-electron wavefunctions in a CNT. We separate spin and valley components; the 16 possible states can be understood as a spin singlet or triplet times a valley singlet or triplet. From this, one can easily find the symmetry under particle exchange. Normalization is omitted for brevity.

and thereby lift spin blockade.

In case of a perpendicular magnetic field, spin states are mixed by spin-orbit coupling (see previous section), which can lift spin blockade by introducing non spin-conserving interdot tunneling [44]. Comparable situations have been studied in InAs QDs [45, 46]. A theoretical study of the influence of spin-orbit coupling in CNTs on Pauli blockade can be found in [43].

Finally, also the hyperfine interaction between the ( $^{13}\text{C}$  -) nuclear spins and the electron spin can lift Pauli blockade [47, 35]. Theoretical work suggests that this hyperfine interaction in CNTs can not only mix different spins but also - because of the short-range nature of the hyperfine interaction - mixes different valleys [42]. However, Pauli blockade can be restored by applying a sufficient parallel magnetic field, which splits different spin- and valley-states.

	spin $\otimes$ valley	symmetry
1	$(K \uparrow K' \downarrow - K' \downarrow K \uparrow)$	-1
2	$(K \uparrow K' \downarrow + K' \downarrow K \uparrow)$	+1
3	$(K \uparrow K \uparrow)$	+1
4	$(K' \downarrow K' \downarrow)$	+1
5	$(K \uparrow K \downarrow + K \downarrow K \uparrow)$	+1
6	$(K \uparrow K \downarrow - K \downarrow K \uparrow)$	-1
7	$(K \uparrow K' \uparrow + K' \uparrow K \uparrow)$	+1
8	$(K \uparrow K' \uparrow - K' \uparrow K \uparrow)$	-1
9	$(K \downarrow K' \downarrow + K' \downarrow K \downarrow)$	+1
10	$(K \downarrow K' \downarrow - K' \downarrow K \downarrow)$	-1
11	$(K' \uparrow K' \downarrow + K' \downarrow K' \uparrow)$	+1
12	$(K' \uparrow K' \downarrow - K' \downarrow K' \uparrow)$	-1
13	$(K \downarrow K' \uparrow + K' \uparrow K \downarrow)$	+1
14	$(K \downarrow K' \uparrow - K' \uparrow K \downarrow)$	-1
15	$(K \downarrow K \downarrow)$	+1
16	$(K' \uparrow K' \uparrow)$	+1

**Table 2.3: Two-electron states in presence of spin-orbit coupling** We consider all four single-electron states. As in the situation without spin-orbit coupling, we have 16 possible states. 6 of these states have an antisymmetric spin and orbital wavefunction part. However, because of spin-orbit coupling, the states have different energies: states 1 - 4 have the lowest energy, states 5 - 12 are higher in energy by  $\Delta_{SO}$  and states 13 - 16 by  $2\Delta_{SO}$ . Note, that now - when we use the spin orbit states as a basis - the states 1,2, 13 and 14 cannot be factorized into a spin- and valley-part.

### 2.3.2 Singlet-triplet splitting and Wigner molecules

Since CNTs are one-dimensional systems, electron-electron interactions play a very different role compared to QDs in three dimensional systems. Electron-electron interactions become particularly important in the limit  $\Delta E/E_C \ll 1$ , i.e. when the charging energy is the dominant energy scale. This regime is valid for long CNTs and low carrier densities. Here we discuss the splitting  $E_{ST}$  between the (0,2) singlet and (0,2) triplet and its role for spin blockade.

A key requirement for observing spin blockade is a sufficiently large  $E_{ST}$ . Although the spacing of longitudinal modes is large in CNTs,  $E_{ST}$  can be affected substantially by electron-electron interactions. In a shell filling model, singlet-triplet splitting is often expressed as the energy difference of two single electron

wavefunctions minus an exchange term [48]:  $E_{ST} = \Delta E_{orb} - E_K$ <sup>3</sup>.  $E_K$  results from the difference in Coulomb repulsion between the two electrons in the singlet and triplet states<sup>4</sup>: For the triplet state, a higher longitudinal mode has to be occupied and the orbital wavefunction is antisymmetric. This results in a reduced Coulomb energy compared to the singlet, where both electrons can occupy the same orbital state and the wavefunction is symmetric (in a strict sense, “exchange interaction” refers to the energy difference of the symmetric and antisymmetric wavefunctions of the type  $\phi_1\phi_2 \pm \phi_2\phi_1$  due to Coulomb interactions; to avoid confusion, we instead use the term  $E_K$  for our situation [48]).

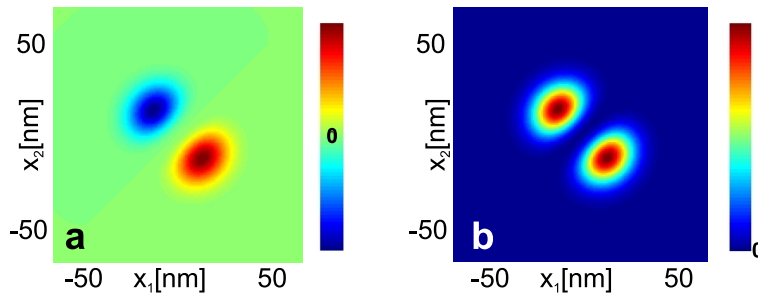


**Figure 2.14: Singlet and triplet wavefunctions** Two-electron wavefunctions  $\phi(x_1, x_2)$  in a CNT-QD as a function of the two electron coordinates  $x_1, x_2$ . Numerical simulations by T. Balder [31] (a) Triplet: the two electrons occupy two separated sections of the CNT. The wavefunction is antisymmetric. (b) Singlet: again the two electrons occupy two separated sections of the CNT, instead of having overlapping wavefunctions. In fact, the wavefunction is - apart from the (anti)symmetry - almost indistinguishable from the one for the triplet. (Note, that the color scales are different in (a) and (b))

We discuss the singlet-triplet splitting on the basis of numerical simulations [31, 49, 50, 51] of the two electron states in a CNT-QD. One finds that for a typical CNT-QD with a length of  $\sim 100nm$ ,  $E_{ST}$  is only  $\sim 5\mu eV$ . However, the level spacing between the first two longitudinal modes is  $\sim 10meV$ , i.e. more three orders of magnitude larger. An explanation for this effect can be found when looking at the charge distribution for the singlet and the triplet: Figure 2.15 shows that rather than being smeared out over the whole length of the CNT-QD, the two electrons are spatially separated for both the singlet and the triplet.

<sup>3</sup>we do not include a Zeeman splitting here, i.e. at a finite magnetic field we only refer to the  $T_0$  triplet.

<sup>4</sup>in a double QD there can also be a contribution from hybridization of the (1,1) and (0,2) states, which we will neglect in our discussion here

Hence it is not appropriate to describe the two-electron states using the single electron wavefunctions and include some modification  $E_K$ . It is more that the Coulomb interaction is the dominant contribution and forces the two electrons in two entirely new, spatially separated orbitals [49, 50, 51, 52]. These orbitals are similar for the singlet and triplet (figure 2.14); this is the reason that  $E_{ST}$  almost vanishes (exchange effects are now negligible since the wavefunctions hardly overlap). This effect is reminiscent of a Wigner crystal [53], where Coulomb repulsion leads to a lattice of localized electrons. Therefore, we call this two electron state a “Wigner molecule”. Besides the charge distribution, a key feature of such a Wigner-molecule in a CNT is a spin- and valley-polarized ground state (already at very small magnetic fields) [49, 51]. This effect has been found both for harmonic [31, 50, 51] and potential-well like [49] confinement potentials. [49, 50, 51] have also included the effect of spin-orbit coupling in their models.

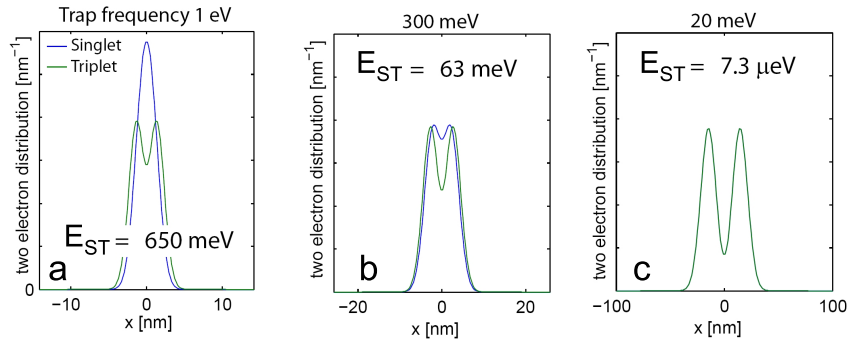


**Figure 2.15: Singlet and triplet charge distributions** Numerical results for the two-electron charge distribution in a CNT-QD with harmonic confinement potential [31]. Higher confinement energies correspond to smaller QDs (a) Very small QD: different charge distribution for singlet and triplet. (b) At smaller confinement energies, the charge distribution for the singlet starts to separate. (c) Already for a 100 nm large QD the singlet and triplet charge distributions are indistinguishable. This is a “Wigner molecule”. As a consequence,  $E_{ST}$  vanishes.

For an experimentalist who wants to use spin blockade as a tool to investigate spin states, the crucial question is whether there are any parameters one can change to enhance  $E_{ST}$ . The first parameter one can change is the size of the QD. In a smaller QD it costs more kinetic energy (zero point motion) for the two electrons to sit in almost separate orbitals next to each other. At some point this kinetic energy is larger than the Coulomb repulsion and the electron wavefunctions will start to overlap (shell filling) and thereby  $E_{ST}$  will increase

(figure 2.15). This crossover happens at a dot size of  $\sim 20\text{nm}$  for a suspended CNT.

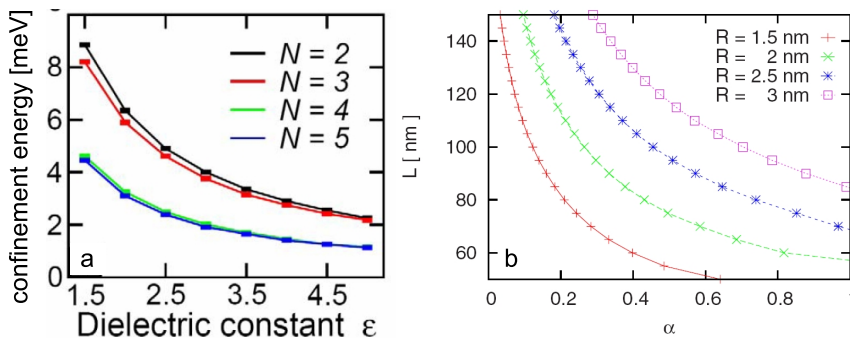


**Figure 2.16: Transition to a Wigner-molecule (a)** Phase diagram for a CNT-QD with harmonic confinement. Below the lines, the  $N$ -electron ground state is a Wigner molecule.  $R = 3\text{nm}$  was assumed. Graph from ref. [51]. **(b)** Critical length in a 2-electron CNT-QD: Above the critical length,  $L$ , the two-electron ground state is a spin- and valley-polarized Wigner-molecule with vanishing  $E_{ST}$ . Numerical calculation of  $L$  as a function of the interaction parameter  $\alpha \approx 2.2/\epsilon$  and the CNT radius,  $R$ . The effect of spin-orbit coupling is included, as well. Graph from ref. [49].

Another possibility is to screen the electron-electron interactions by embedding the CNT in a material with a large dielectric constant. The simulations in figures 2.14 and 2.15 have been carried out for a suspended CNT, i.e. the dielectric constant of the environment is  $\epsilon = 1$ . One can define a critical length, above which the two electron ground state is a “Wigner molecule” with a spin- and valley polarized ground state and vanishing  $E_{ST}$ . This critical length depends exponentially [49] on  $\epsilon$ , as shown in figure 2.16. One finds that  $\epsilon \sim 5$  gives a critical length on the order of 100 nm, i.e. the typical size of CNT-QDs in recent experiments. Possible materials to embed the CNT in are e.g. silicon dioxide ( $\epsilon = 3.9$ ) or aluminium oxide ( $\epsilon = 9.3$ ). Indeed, spin blockade has been observed in CNTs covered with such a dielectric [54] but not in suspended CNTs (chapter 7 of this thesis).

### Mott insulating state

Another consequence of electron-electron interactions could be linked to the small-bandgap CNTs, discussed earlier in this chapter. It has been claimed that the existence of small, non closing bandgaps in CNTs (as shown in section 2.1.3)

can be explained by a Mott insulating state [15]. Such a state has been predicted theoretically for CNTs [55]. In general, a Mott insulator is a type of material which is expected to be a conductor when not taking electron-electron interactions into account; but the Coulomb repulsion of the electrons opens up a gap (usually at half-filling, when there is one electron per lattice site) [56]. For CNTs, such a insulating state around  $E_F$  would open up a gap in the band structure (not only a shift of the quantized wave vector), as shown in figure 2.9b. However, there is also experimental data showing CNTs without any gap, i.e. true metallic behavior [57]. Therefore, this subject is still asking for further investigation.





# Chapter 3

## Fabrication

In this chapter, we describe the fabrication of our CNT samples. We have used two very different types of devices: For the first type, CNTs are grown on a substrate and thereafter electrical contacts, top gates and SET charge detectors are fabricated. For the second type of devices, structures like trenches, contacts and gates are fabricated first and the CNT are grown over these structures in the very last fabrication step. For the first type of devices, we use very much standard recipes. Therefore, we will not give a detailed step-by-step description of the fabrication but instead present the used techniques (electron beam lithography, double angle shadow evaporation) and discuss the limitations they impose on possible devices. Thereafter, we will explain how we grow the CNTs. Again, this is a well tested standard recipe. In the second part of this chapter, we present the fabrication of gates and trenches in Si/SiO<sub>2</sub> substrates for the suspended CNT devices. Finally, we discuss the fabrication of narrow gates for suspended CNT devices.

### 3.1 Electron beam lithography

To fabricate a CNT device, a number of different small structures have to be defined on a Si/SiO<sub>2</sub> substrate. The method to do this is electron beam (ebeam) lithography. Each ebeam lithography cycle consists of the steps shown in figure 3.1. The smallest structures we can define by this method are around 35 nm. One can improve this number down to  $\sim 20\text{nm}$  by optimizing the ebeam focusing, which is usually done by focusing on on-chip markers close to the exposed areas. The relative alignment accuracy between different ebeam steps is typically better than 50 nm, if we use alignment markers close enough to the exposed areas.

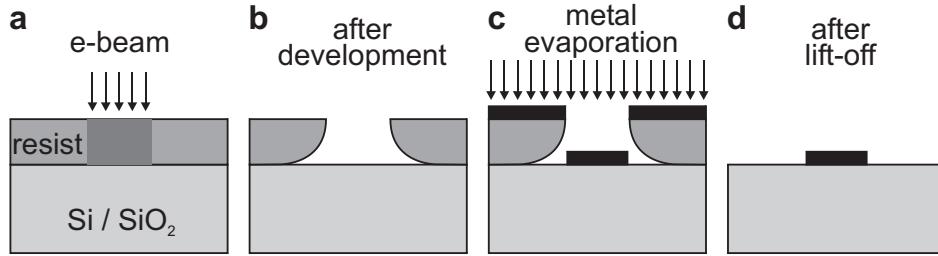


**Figure 3.1: Electron beam lithography** (a) A double layer of resist is spun on the substrate and the desired pattern is exposed with a beam of high energy electrons. (b) A chemical developer removes the irradiated areas of the resist. Since the bottom layer is more sensitive to ebeam radiation there is a so called *undercut* (c) One or more layers of metal (or dielectric) are evaporated on top of the developed resist layer. (d) A chemical solvent (usually acetone) removes the resist with the metal on top of it. Metal remains on the sample only at the predesigned areas. The undercut ensures a proper lift-off.

#### Disorder and fabrication

For the CNT-on-substrate type of devices, we have to do four ebeam lithography cycles after CNT growth (ohmic contacts, top-gates, SETs and bonding pads). We observe from low-temperature transport measurements that the disorder in the CNTs is very high after these processing steps. Already short CNT segments (typical CNT-QDs have a length of less than 500nm) break up in multiple QDs at low carrier densities. Only at high carrier densities, when the Fermi energy is higher than the disorder potential, the CNTs behave as single QDs. This is demonstrated in figure 3.2. It should be noted, that this data is taken from a semiconducting CNT. Semiconducting CNTs are generally more suscep-

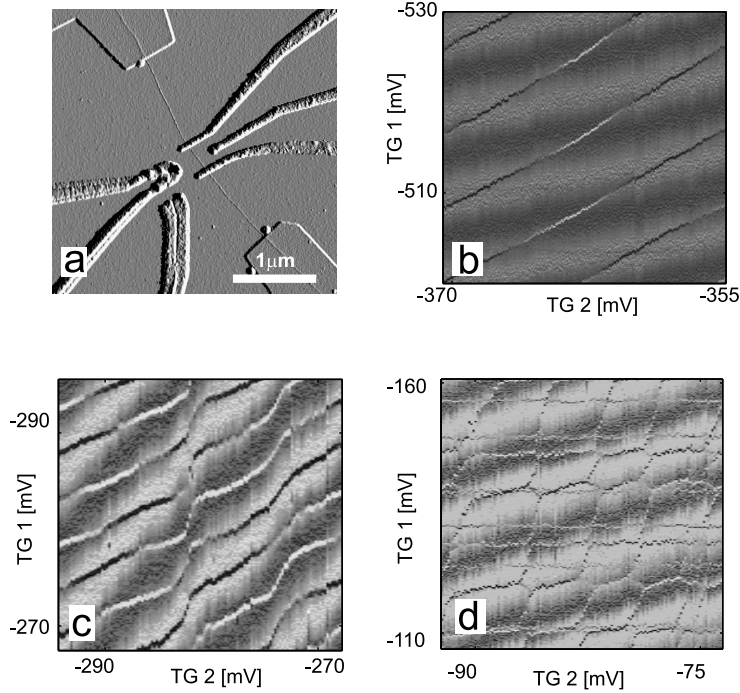


**Figure 3.2: Disorder at different electron densities** Stability diagrams of a CNT with two top-gates (TG1 and TG2) which are separated by 400nm. The sample is the same, we have used for the experiments in chapter 6. The stability diagrams are obtained with a SET charge detector, positioned between the two top-gates (and therefore sensitive to the CNT segment between the top-gates). (a) shows an AFM image of the device. The electron density is controlled with the back gate voltage (BG). If disorder is weak, we expect a single QD behavior, i.e. diagonal lines in the stability diagrams. (b) High electron density (BG = 6.25 V): Diagonal lines indicate single QD behavior. (c) Intermediate electron density (BG = 5V). The CNT starts to break up into a coupled double QD. (d) Low electron density (BG = 2.5 V): Disorder is dominant. The CNT section between the two TGs has broken up in multiple islands. This is evident from the multiple and crossing sets of charging lines in the stability diagram.

tible to disorder than metallic / small bandgap CNTs [58]. Therefore it would be desirable to use small bandgap CNTs, however for the top-gate design this is not possible since we found that small bandgaps ( $\leq 40$  meV) are not enough to pinch off a barrier with top gates<sup>1</sup> (with a typical width of 40nm). On the other hand, for the clean, suspended CNTs, where we define barriers by pn-junctions,

<sup>1</sup>this is necessary e.g. for relaxation time measurements

we find this is possible very well with small bandgap CNTs. Because of the small disorder, the width of pn-junction in a suspended CNT can be made much larger than the typical width of topgates in the CNT-on-substrate type of devices.

There are two main reasons why ebeam lithography based fabrication can induce disorder in CNTs: (i) The chemical processing leaves some residue of resist (or chemicals used for development and lift-off) on top of the CNT (ii) the ebeam radiation can induce defects in the CNTs [59].

To prevent fabrication induced disorder, we obtained the best results by growing the CNTs in the very last fabrication step, as described in chapter 7. Also, covering CNTs with a noncovalent functionalization layer followed by an  $\text{Al}_2\text{O}_3$  layer, deposited by atomic layer deposition, has shown to yield clean QD devices [54].

## 3.2 SET fabrication

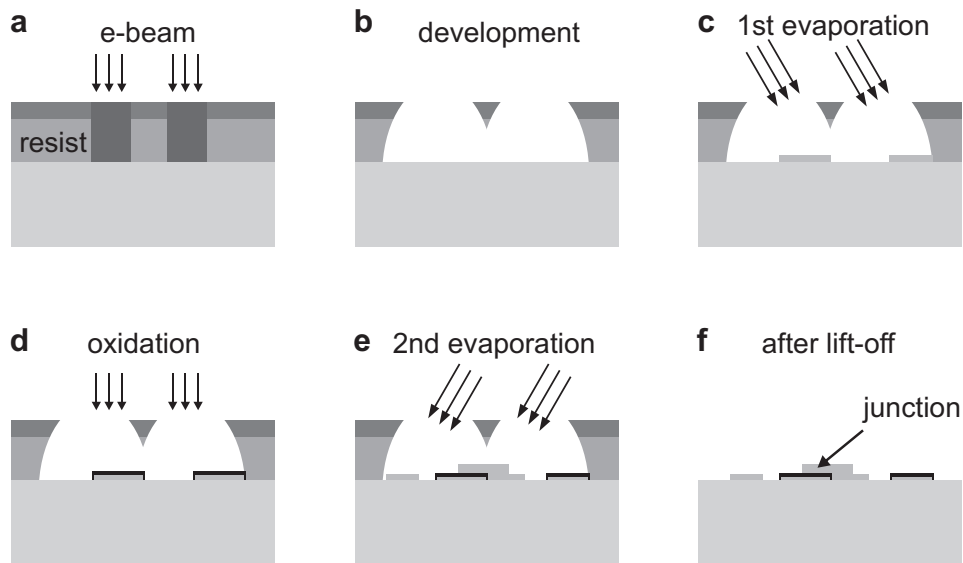


**Figure 3.3: Fabrication of small Al /  $\text{Al}_2\text{O}_3$  junctions** (a) A double layer of resist is spun on the substrate and a bridge shaped pattern is exposed with a beam of high energy electrons. (b) A chemical developer removes the irradiated areas of the resist. It is necessary that all bottom layer resist under the bridge is removed. (c) A first layer of Al is evaporated under an angle (d) Controlled oxidation creates a thin layer of  $\text{Al}_2\text{O}_3$  (e) The second Al evaporation step, this time with an opposite evaporation angle. A junction is created under the resist bridge. (f) Chemical lift-off finishes this fabrication cycle.

We use aluminium single electron transistors (Al-SETs) as charge detectors for CNT-QDs. An Al-SET consists of a small aluminium island, connected to leads via  $\text{Al}_2\text{O}_3$  tunnel junctions. These junctions have a size of about  $60\text{nm} \times 60\text{nm}$ . To fabricate these junctions with ebeam lithography one has to use a double angle shadow evaporation technique [60], as shown in figure 3.3. We use resist bridges with a width of 70 nm. To fabricate those resist bridges, a bottom layer resist has to be used which can have a large enough undercut. We use a 250nm thick layer of PMGI as bottom layer. This resist has the advantage that the undercut can be controlled by a developer which does not attack the top layer resist (PMMA) and thereby allows to fabricate resist bridges with good precision and reproducibility. After ebeam exposure, the pattern in the top layer is developed in MIBK : IPA (1:3) for 70 seconds (followed by 70 seconds in IPA), with a successive development in Concentrate :  $\text{H}_2\text{O}$  (1:1) for 3 min (followed by 60 seconds in  $\text{H}_2\text{O}$ ). This results in a 500nm large undercut in the PMGI bottom layer.

The next step is the double angle evaporation. We evaporate two layers (30nm and 40nm) of aluminium, under angles of  $\pm 15^\circ$ . In between the two evaporation steps we do a controlled oxidation for 12 min at an oxygen pressure of  $100\mu\text{bar}$ . This results in a junction resistance of  $\sim 100k\Omega$ . To change the junction resistance we typically change the junction area by either changing the evaporation angle or the resist bridge width. In principle it is also possible to vary the junction resistance by changing the oxygen pressure during the oxidation step.

### 3.3 Carbon nanotube growth

We fabricate our CNTs using chemical vapor deposition (CVD) growth [61]. First, spots for the catalyst, from which the CNTs will grow, are defined in a PMMA mask via ebeam lithography. The catalyst consists of 40 mg  $\text{Fe}(\text{NO}_3)_3 \cdot 9\text{H}_2\text{O}$ , 4 mg  $\text{MoO}_2$  (acac)<sub>2</sub> and 30 mg Alumina nanoparticles (Degussa Aluminium Oxide C), dissolved in 30 ml methanol. A few droplets of the catalyst are deposited on the substrate with the developed PMMA mask. After baking 10 min at  $150^\circ$  we do a lift-off in hot acetone, leaving catalyst only at the predefined spots on the substrate. Special care has to be taken not to end up with catalyst all over the sample (the catalyst sticks extremely well to  $\text{SiO}_2$ ) and not only at the predefined spots. We usually ensure this by doing a two step lift-off. First, we move the sample quickly through a beaker of warm acetone inside a sonicator. Then the sample is immediately (without letting it become dry) transferred to a second beaker of acetone, where it is left for 5 min.

For growth, the sample is put in a quartz tube inside a furnace. The CVD growth is performed at 900 °C under 700 sccm H<sub>2</sub> and 520 sccm CH<sub>4</sub> gas flow for 12 min. Heating up and cooling down is done under Ar flow. Now, from the catalyst spots CNTs have grown in random direction with typical lengths of 1 - 20 μm. The CVD growth parameters (catalyst composition, temperature and gas flow rates) are optimized to produce a high yield (> 90%) of single-wall CNTs with diameters of 1 - 5 nm. The peak of the diameter distribution is between 1 and 2 nm [61]. There is no control over the CNT chirality, meaning we probably get a random distribution of chiralities (within the given diameter distribution). Indeed, we find that roughly ~ 1/3 of the CNTs are metallic or small bandgap and ~ 2/3 are semiconducting, as expected. The CVD growth works equally well for growing CNTs on a flat SiO<sub>2</sub> substrate or over predefined W/Pt metal contacts and trenches.

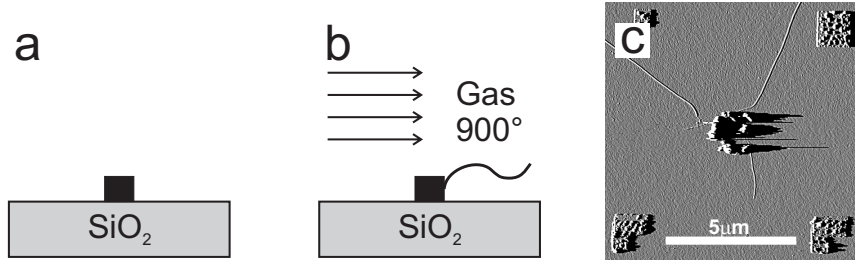


**Figure 3.4: CVD growth of CNTs** (a) Small islands of catalyst are deposited at predefined positions via ebeam lithography (b) A mixture of growth gases flows over the sample at high temperatures inside a furnace. CNTs grow from the catalyst spots. (c) AFM image of CVD-grown CNTs. From the catalyst island several CNTs have grown in random directions. The typical length is between 1 and 20 μm. The four markers at the corners are for alignment purposes.

### 3.4 Etching of silicon structures

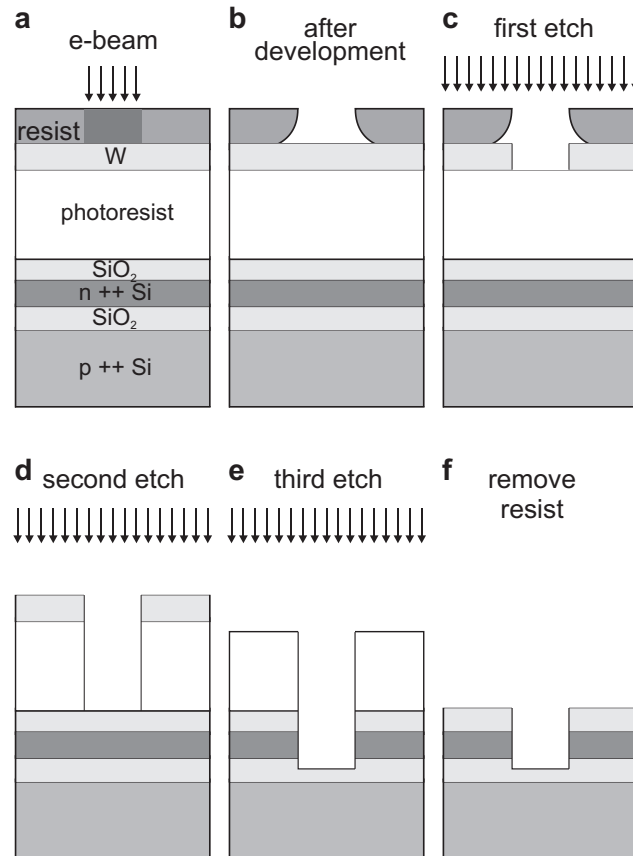


**Figure 3.5: Etching of structures into Si/SiO<sub>2</sub> substrates** (a) Resist layer profile and ebeam irradiation. (b) Chemical development after ebeam irradiation (c) Creating an etch mask in the W layer for the second etch. (d) Creating a mask in the photoresist layer for the Si / SiO<sub>2</sub> etch. (e) Etching through the Si and SiO<sub>2</sub> layers. (f) Removing the leftover photoresist

Here we describe the method used to etch small structures (trenches and gates) into a Si/SiO<sub>2</sub> substrate. This is used for the clean, as-grown CNT samples in chapter 7. The fabrication scheme is shown in figure 3.5. First, the desired pattern is defined by ebeam lithography in a PMMA top layer. Then, the pattern is transferred to a underlying 7nm thick layer of W by a Fluorine based dry etch. In a second dry etching step, the pattern is now transferred to a 500nm thick layer of photoresist, using an oxygen plasma. The photoresist will now serve as an etch mask for the Si/SiO<sub>2</sub> etch, which is done by dry etching with an CHF<sub>3</sub> / O<sub>2</sub> plasma. The O<sub>2</sub> is necessary to prevent the formation of teflon on the sam-

ple. By carefully adjusting the amount of  $O_2$ , the anisotropy of the etch can be improved significantly. This is, because the oxygen ions in the plasma etch the photoresist also in the horizontal direction which leads to a non-vertical etch of the underlying Si/SiO<sub>2</sub>.

While this fabrication scheme works well for creating split-gates (as used in chapter 7), it is not suitable for creating narrow gates. We find that gates with a width of less than 400nm (and a typical length of 5  $\mu\text{m}$ ) show carrier localization at temperatures below 1K. Probably the gates break up in several electrically isolated islands, which means they can not be used as local gates for QD devices.

### 3.5 Fabrication of narrow gates for clean, suspended CNT devices

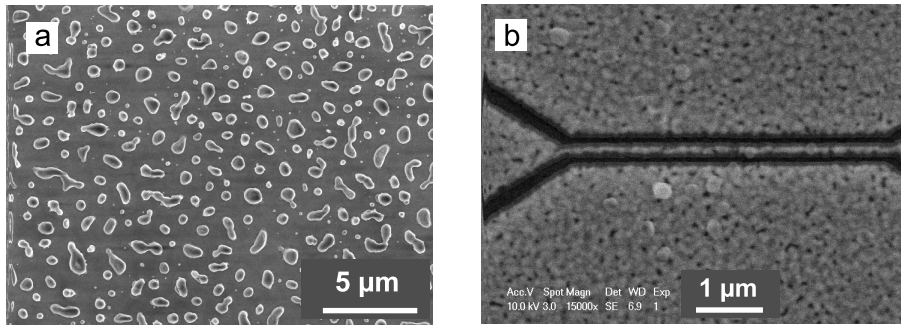


**Figure 3.6:** Thin metal films after heating up to 900°C in the CVD oven. SEM images (a) A 50nm thick film of Co (on a SiO<sub>2</sub> substrate) after CVD-growth. Despite the high melting point of > 1400 °C, the thin film has transformed to a layer of disconnected islands. (b) Rhenium: although thin layers are not affected visibly by the CVD-growth, the grain-size is too large for the fabrication of narrow gates.

To perform experiments with tunable single and double QDs in clean CNTs, it is desirable to combine local electric gates with a fabrication scheme where CNTs are grown in the last fabrication step across a predefined trench (as described in chapter 7). Also, these gates should ideally be suited for applying high-frequency pulses, to make experiments like relaxation-time measurements or coherent spin manipulation possible.

The main challenge is to find a metal or alloy, such that even even narrow ( $\simeq 100\text{nm}$ ) gates survive the high temperatures (900° C) during the CVD-growth of the CNTs. Some metals, e.g. Cr or Co have a high (>1000 ° C) melting point, but thin films of these metals partially melt, thereby forming a carpet



### 3.5 FABRICATION OF NARROW GATES FOR CLEAN, SUSPENDED CNT DEVICES

---

of disconnected islands. For other metals, e.g. Re, thin films survive the high temperatures but they have a too large grain size for the fabrication of narrow gates. Typical problems are shown in figure 3.6.

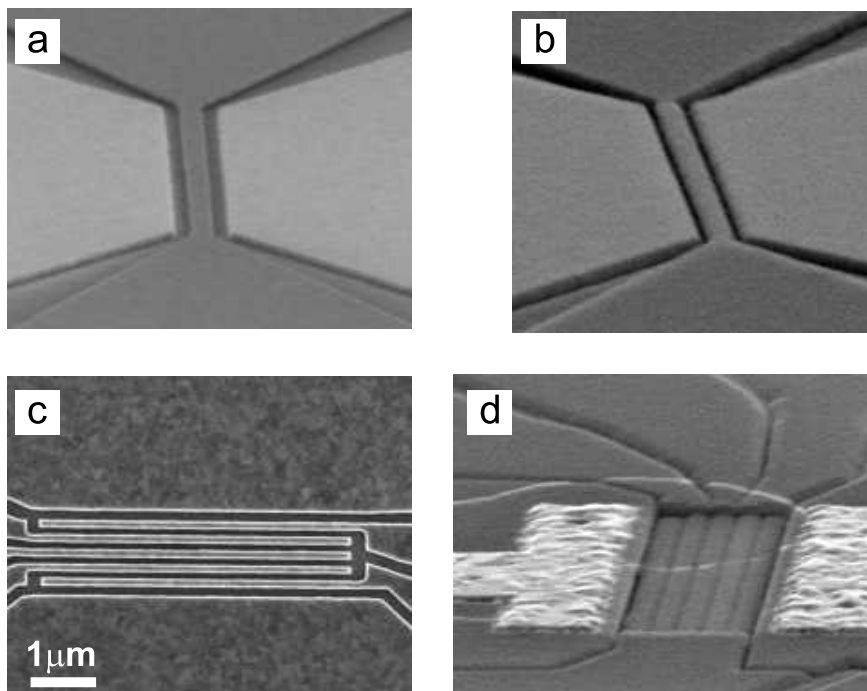


**Figure 3.7: Fabrication of narrow gates from W.** SEM images of test- and final devices (a) A  $\sim 200nm$  wide gate is fabricated from a 50 nm thick layer of W by a reactive ion etching process. (b) The chip is covered with a dielectric (here:  $Si_3N_4$ ); both sputtering and ALD result in a conformal covering of the structures. The high temperatures (900 °C) inside the CVD oven have not lead to any damage of the structure. (c) SEM image of five gates, fabricated with the method described above. The gray-black patterned areas are W; areas where the W has been etched show up black. The smallest gates, still working reliable, are around 100nm wide, with a pitch of 250nm. (d) A complete device: CNTs are bridging a trench between two W/Pt contacts. In this case, the CNT is touching the dielectric at the bottom of the trench (CNTs show up brighter in SEM images, when they touch a dielectric). Note that the quality of the W/Pt on the  $Si_3 N_4$  after CVD growth is worse than on a  $SiO_2$  substrate.

The best results so far are obtained with sputtered tungsten (W). The fabrication steps are shown in figure 3.7. A 50nm thick layer of W is sputtered on a  $SiO_2$  surface and afterwards the desired gate pattern is created by ebeam lithography and reactive ion etching, using the same etch mask as in section 3.4. Afterwards, the gates are covered with a dielectric, typically PECVD -  $SiO_2$ ,

$\text{Al}_2\text{O}_3$  or sputtered  $\text{Si}_3\text{N}_4$ . Gates with dimensions of  $100\text{nm} \times 5\mu\text{m}$  have a room-temperature resistance of  $\sim 700\Omega$  which is further reduced to  $< 200\Omega$  below 1K. This means the gates are also suitable for application of high-frequency electrical pulses. Also, voltage differences up to  $> 10\text{V}$  can be applied to these gates (with a spacing of 100-150 nm) without observing electrical leakage.

Fabrication now continues by deposition of contacts made of  $W/\text{Pt}$  (5nm/25 nm) and etching a trench into the dielectric between the contacts. The trench should be deep enough, to ensure that the CNTs do not touch the dielectric at the bottom of the trench if one aims for ultra-clean devices. Experience shows that a ratio of 3:1 between the width and depth of the trench is sufficient for the majority of the grown CNTs to be fully suspended. If one wants to have CNTs in contact with the dielectric substrate (to screen electron - electron interactions, as discussed in chapter 2.3) it is important to make sure that the dielectric which is covering the gates does not have any sharp edges to prevent kinks in the CNT. After catalyst deposition at predefined spots near the trench, CNTs can be grown on the samples (see section 3.3).

It seems still possible to reduce the width and spacing of the W-gates to obtain smaller QD devices. Both optimizing the etching process (thinner resist mask and different plasma conditions to increase the anisotropy of the etch) and switching to a evaporation-based fabrication [46, 62] might bring an improvement.

### 3.6 Room temperature characterization

Not every CNT device is suited for low-temperature measurements. Since wire bonding and cooling down devices to cryogenic temperatures is time consuming, it is desirable to preselect as much as possible by comparably easy and fast tests at a room-temperature (RT) probe station. By measuring the conductance as a function of gate voltage one can determine whether a CNT is semiconducting or metallic / small bandgap. For small bandgap CNTs, one can also get a rough estimate of the bandgap magnitude. Furthermore, the measured conductance gives an indication of the quality of the CNT-metal contacts.

For the CNT-on-substrate type of devices, we use RT measurements after the fabrication of metal contacts to select semiconducting CNTs for further processing. The testing of top-gates is more critical: we found that applying voltages to the top-gates under ambient conditions often results in damage of the CNTs, possibly via electrical break-through due to the very thin insulating layer between top-gates and CNTs.

For the suspended CNTs, where CNT-growth is the last fabrication step, we

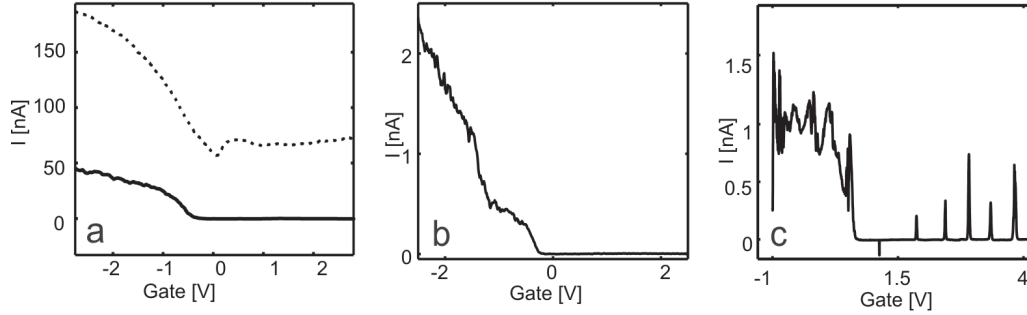


**Figure 3.8: Room temperature testing (I)** At room temperature, we perform measurements of the CNT conductance versus the voltage applied to a gate (usually the back gate or split-gates). Such a measurement is also called a “transistor curve”. Here, we show measurements from suspended CNT devices. **(a)** A semiconducting (solid line) and a small bandgap (dashed line) CNT. For semiconducting CNTs, we find usually no measurable n-type conductance (positive gate voltages) if the contact metal (here W/Pt) is making better contact for holes than for electrons due to its work function. **(b)** A step in the transistor curve indicates that there is more than one CNT between the contacts. The step is due to the different bandgaps and/or different positions of the Dirac point (with respect to zero gate voltage) of the CNTs. Such devices are not selected for low-temperature measurements **(c)** Measurement of the small bandgap device from (a) at 2K. On the p-side conductance is high, while on the n-side electrons are added to a QD potential. The first few electrons are clearly visible, indicating the low level of disorder in this device.

use room temperature measurements to select small bandgap CNTs with low contact resistance. Also it is sometimes possible, to exclude devices with more than one CNT crossing the trench between the metal contacts. Our experience with these ultra-clean CNTs is that devices with a smooth room temperature transistor curve, small contact resistance and a Dirac point near zero gate voltage are likely to reach the few electron regime at low temperatures without showing significant disorder (figure 3.8). When CNTs are grown at the last step across several narrow gates, RT measurements can also yield information about the position of the CNT with respect to these gates, as shown in figure 3.9.

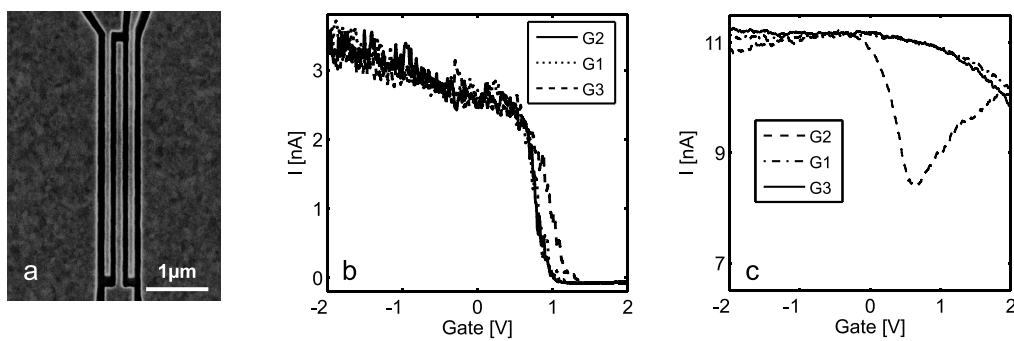


**Figure 3.9: Room temperature testing (II)** For devices, where CNTs are grown over several narrow gates, the RT transistor curves can provide information over the position of the CNT with respect to the gates. We show transistor curves of CNTs which are suspended over three narrow gates. The current is measured as a function of the voltage, applied to the three gates (a bias voltage of 1mV is applied between source and drain). **(a)** Gate pattern. SEM image. The middle gate and the outer gates run from opposite directions into the trench. **(b)** All three gates couple equally strong to the (semiconducting) CNT. Therefore, we conclude that the CNT is placed above the gate area. **(c)** The middle gate (G2) is coupling much stronger to the (small bandgap) CNT than the two outer gates (G1 and G3): the CNT is running between the two ohmic contacts outside the central gate area.

# Chapter 4

## Charge detection with single electron transistors

### 4.1 Charge detection in CNT-QDs

Transport measurements are a powerful tool and can provide a great variety of information on single and double QD systems. However, there are also situations where transport measurements cannot provide the desired information. First, transport measurements are not suitable for single shot measurements (e.g. single shot spin readout). Also it is not possible to investigate processes (e.g. a tunneling rate or a relaxation time) which are slower than the timescale given by the minimal measurable current.

Therefore, it can be desirable to read out the charge state of a QD independently of the current by an external charge detector. This is some device sitting next to the QD and telling us its charge state. In principal, any device with a highly gate-dependent resistance and strong capacitive coupling to the QD can fulfill this task. A change of the electron number on the QD will induce a change in the resistance of the detector, which then can be measured. It should be mentioned that a charge detector measurement is not restricted to single shot measurements. A charge detector can also be used to investigate processes which are faster than its measurement time; in this case the charge detector will just measure an average property (comparable to a transport measurement).

What are possible charge detectors for CNT-QDs? Quantum Point contacts (QPCs) are the most basic nanoscale devices with a gate dependent resistance. For QDs in GaAs-2DEG heterostructures, they have proven to be excellent charge detectors [63, 64]. For CNTs, however, a QPC does not seem a suitable choice. CNTs would have to be fabricated on top of a heterostructure instead of the

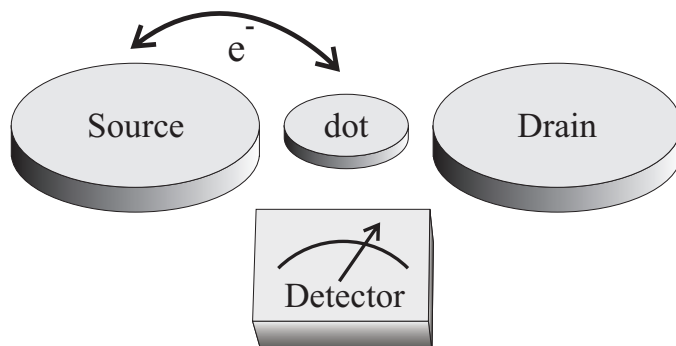


**Figure 4.1: Schematic of charge detection** A charge detector is a device which is capacitively coupled to the QD and thereby allows a readout of the charge state of the QD

usual Si/SiO<sub>2</sub> substrates. Also geometrically, using a QPC is difficult to combine with typical top-gate designs, used for CNTs and nanowires [65, 66]. Therefore, we decided to use a metallic single electron transistor (SET) in close vicinity to the CNT-QD as a charge detector [67, 68, 69].

## 4.2 Aluminium single electron transistors

We briefly discuss the properties of aluminium single electron transistors (Al-SETs) and the implications for charge detection. Al-SETs consist of a small metallic island connected to a source and a drain via Al<sub>2</sub>O<sub>3</sub> tunnel junctions (figure 4.2 a). The tunnel junctions are fabricated by a standard double angle shadow evaporation technique, resulting in a few nm thick oxide layer which forms the junctions. An additional side gate allows to tune the electrical potential on the island. The island has a typical size a few  $(100\text{nm})^2$  and can have almost any shape. The tunnel junctions have a size of at least  $50\text{nm} \times 50\text{nm}$ , limited by the grain size of Aluminium (we found that smaller junctions give a very unreliable junction resistance). The total thickness of the Aluminium is around 70nm for our fabrication recipe (see chapter 3 for details). If the junctions are sufficiently opaque (i.e. with a conductance of the order of the conductance quantum  $e^2/h$  or lower), the Al-SET will show Coulomb blockade at low temperatures. In particular, the conductance exhibits Coulomb oscillations as a function of the

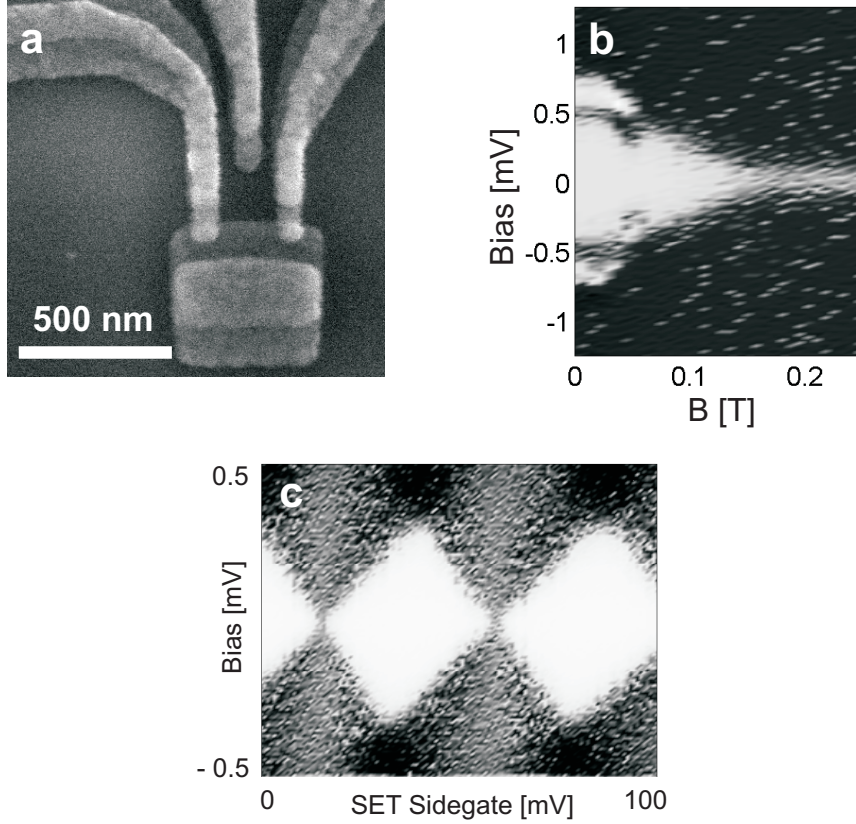


**Figure 4.2: Aluminium single electron transistors** (a) Scanning electron micrograph of an Al-SET. A doubling of the structures results from the shadow evaporation. (b)  $dI/dV$  for a SET as a function of applied bias voltage and perpendicular magnetic field. Dark colors correspond to high  $dI/dV$ . At high magnetic fields, a small gap exists around zero bias voltage due to Coulomb blockade. At low magnetic fields, there exists (in addition to the Coulomb gap) also the superconducting gap. The transition from the superconducting to the normal conducting state takes place between 50 and 150 mT. (c)  $dI/dV$  as a function of applied bias and gate voltage. Dark colors correspond to high  $dI/dV$ . At low temperatures (here  $T = 40\text{mK}$ ) Coulomb interaction blocks the current inside the white, diamond-shaped regions, where the electron number on the island is fixed. A perpendicular magnetic field of 0.5 T was applied.

electrical potential on the island. The typical charging energy is  $E_C = 100 - 500\mu\text{eV}$ . This means Coulomb blockade will vanish at temperatures above  $\sim 1\text{K}$ . The total capacitance of such a SET is  $C_\Sigma = e^2/E_C \approx 10^{-15}\text{F}$ , with its largest contribution coming from the capacitance to the back gate. Figure 4.2 c shows the charge stability diagram of a typical Al-SET. We should mention that because of the small  $k_F$  in metals, no effects related to the quantization of energy levels

will play a role. An important parameter of the SET is the junction resistance,  $R$ . A large  $R$  results in a good sensitivity but on the other hand also reduces the signal and can thereby decrease the signal to noise ratio. We found that a junction resistance of  $\sim 100k\Omega$  results in acceptable charge sensitivities on the one hand, and can be fabricated with a good reproducibility on the other hand. Aluminium is superconducting at low temperatures. Bulk aluminium has a critical temperature of  $T_C = 1.2\text{K}$  and a critical magnetic field of  $B_C = 10\text{mT}$ . For our Al-SETs we use thin aluminium films with a total thickness of  $\sim 70\text{nm}$ . Compared to bulk aluminium, these thin films have a similar  $T_C$  but a higher critical magnetic field. This is shown in figure 4.2c, where we extract  $B_C \approx 0.1\text{T}$  for a temperature of  $50\text{mK}$  (the field orientation is perpendicular to the film). In our measurements, we typically operate the Al-SET in the normal conducting state by applying a magnetic field of at least  $0.3\text{T}$ .

### 4.3 Sensitivity

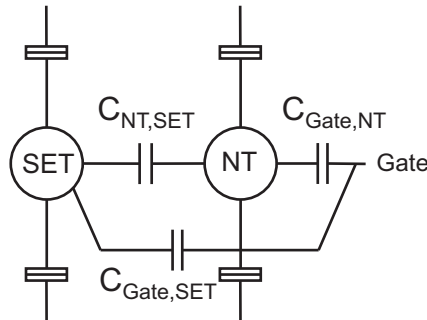


**Figure 4.3: Circuit diagram** Schematic circuit diagram of a SET coupled to a CNT-QD. Both SET and CNT-QD are coupled to source and drain contacts by tunnel junctions. The capacitance between CNT-QD and SET is  $C_{NT,SET}$ . A (back- or side-) gate is used to tune the CNT but also has a finite capacitance to the SET. We often also use an additional gate which couples mainly to the SET (not shown in this diagram).

In this section, we explain what the term “sensitivity” of a charge detector means [70] and how it can be optimized. The capacitance<sup>1</sup> between the CNT-QD

<sup>1</sup>The relation between the charge and voltage of several capacitively coupled components is described by the capacitance matrix. One can think of each element of the capacitance matrix  $C_{A,B} = Q_A/V_B$  as the amount of charge induced on component  $A$ , divided by the voltage applied to component  $B$ , while the voltages on all other components are set to zero. Because of



and the SET is defined as

$$C_{NT,SET} = \frac{Q_{NT}}{V_{SET}} = \frac{Q_{SET}}{V_{NT}} = C_{SET,NT} \quad (4.1)$$

Here  $Q_{NT(SET)}$  is the charge on the CNT (SET) and  $V_{SET(NT)}$  is the electrical potential on the SET (CNT). Note, that we have used that the capacitance matrix is symmetric. The self capacitances of the CNT-QD and SET are defined as

$$C_{NT,\Sigma} = \frac{Q_{NT}}{V_{NT}}; C_{SET,\Sigma} = \frac{Q_{SET}}{V_{SET}} \quad (4.2)$$

The coupling between CNT-QD and SET is defined as the amount of charge  $Q_{SET}$ , induced on the SET when a charge  $Q_{NT}$  is put on the CNT-QD. From Equations 4.1 and 4.2 we find for the coupling

$$\alpha_{NT,SET} = \frac{Q_{SET}}{Q_{NT}} = \frac{C_{SET,NT}}{C_{NT,\Sigma}} \quad (4.3)$$

However, there cannot be a detection without a backaction (basically, this follows from the symmetry of the capacitance matrix). Since we measure the current through the SET, the electron number on the SET is fluctuating between  $N$  and  $N+1$  (if we apply a sufficiently low bias). Similarly to equation 4.3, the change of one electron on the SET induces a charge on the CNT-QD:  $Q_{NT} = Q_{SET} C_{SET,NT}/C_{SET,\Sigma}$ . In terms of voltage this is

$$V_{NT} = Q_{SET} \frac{C_{NT,SET}}{C_{SET,\Sigma} C_{NT,\Sigma}} \quad (4.4)$$

This is something to keep in mind for experiments, where small energy transitions on the CNT-QD are possible: The fluctuating charge on the SET island is some extra charge noise in the environment that can induce such transitions!

Now we want to explain what we call the ‘‘sensitivity’’ of a charge detector. Basically it means how long we have to average the current through the detector to measure a change of the electron number by one on the CNT-QD. Because of noise this time is not arbitrarily short, but we have to average over

---

the linearity of the charge-voltage relation, this is equivalent to the excess charge  $\Delta Q_A$  induced on  $A$ , when the voltage on  $B$  is changed by  $\Delta V_B$  and all the other components are at an arbitrary but fixed voltage. In the following we will for brevity talk about the ‘‘capacitance’’ between components  $A$  and  $B$ , but one should keep in mind that we are always meaning the corresponding element of the capacitance matrix.

some finite time. Let us consider the noise in the current of the SET,  $\delta I_{SET} = \sqrt{\langle (I_{SET} - \langle I_{SET} \rangle)^2 \rangle} / \sqrt{B}$ , where  $B$  is the bandwidth. This current noise can be converted into an equivalent charge on the SET-island via  $\delta Q_{SET} = (dI_{SET}/dV_G)^{-1} \Delta_V^{-1} \delta I_{SET}$ . Here  $\Delta_V$  is the gate voltage difference, needed to put one more electron on the SET island. Together with the coupling  $\alpha_{NT,SET}$  this gives the sensitivity  $\delta q$  of the charge detector :

$$\delta q = \alpha_{NT,SET}^{-1} \delta Q_{SET} \quad [e/\sqrt{Hz}] \quad (4.5)$$

From equations 4.1 and 4.5 it is clear that for a good sensitivity we need a high coupling, low noise and a strong gate dependence of the detector.

## 4.4 Experimental demonstration

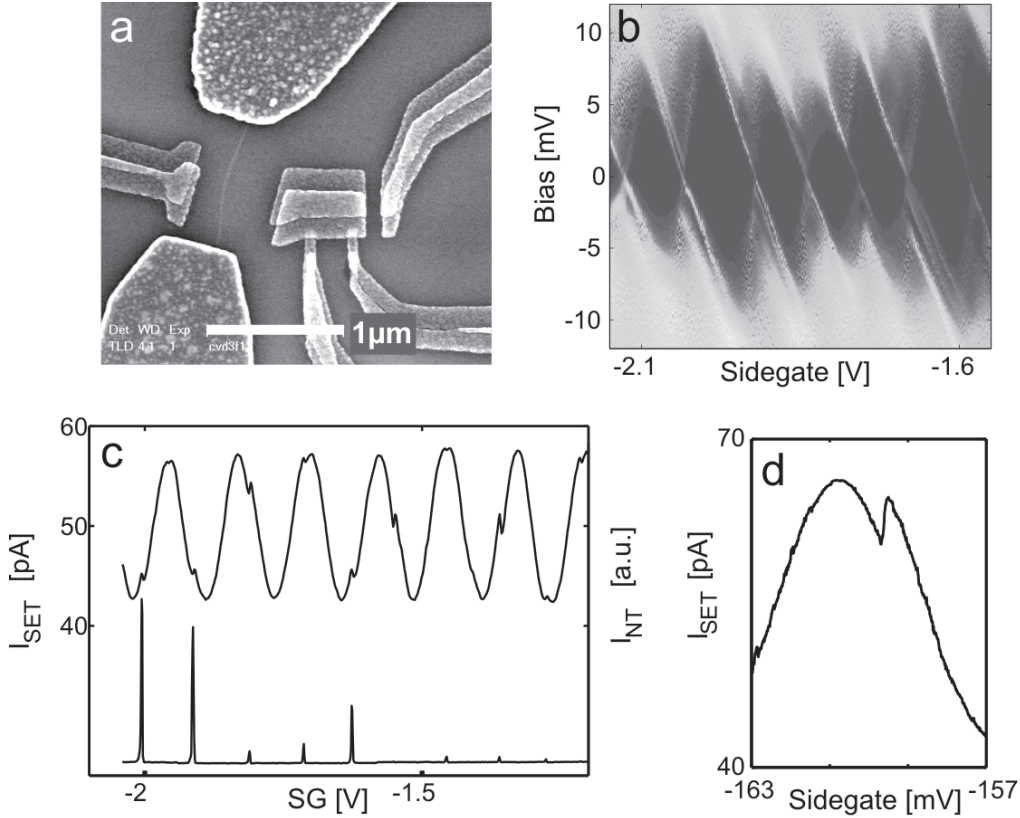


**Figure 4.4: Demonstration of charge detection on a CNT-QD** (a) Scanning electron micrograph of the device: A QD is defined in a small-bandgap CNT between source and drain contacts. An Al-SET is placed in close proximity to the CNT. (b) CNT-QD:  $dI/dV$  through the CNT as a function of applied bias and gate voltage. High  $dI/dV$  corresponds to bright colors. Coulomb diamonds indicate a single QD with a charging energy of 5–10 meV. (c) Measurement of the current through SET (top) and CNT (bottom) as function of applied gate voltage. For the CNT, peaks in the current indicate where the electron number changes by one. In  $I_{SET}$ , the large scale oscillations are due to Coulomb blockade of the SET. Additionally, sharp phase shifts in  $I_{SET}$  occur exactly at the positions where the electron number on the CNT-QD changes. These shifts are due to capacitive coupling of single electrons on the CNT-QD to the SET. The measurement of the upper curve was taken with zero bias voltage applied to the CNT. (d) Zoom in on a charge detection event.

We demonstrate the working principle of the SET charge detector for a simple system: We have defined a QD in a CNT by source and drain contacts, that is by means of the Schottky barriers at the metal-CNT interface [26, 27]. CNTs are grown on a Si/SiO<sub>2</sub> substrate by CVD growth. The CNTs are contacted by evaporating Cr / Au (5 / 30 nm) electrodes. An additional sidegate allows to tune the electrical potential on the CNT-QD. Next to the CNT, we have fabricated an Al-SET by a shadow angle evaporation technique. The measurements are carried out in a dilution refrigerator with a base temperature of about 40 mK. A magnetic field of 0.5T has been applied to keep the Aluminium in the normal conducting state.

In figure 4.4 we demonstrate how the Al-SET serves as a charge detector for single electrons on the CNT-QD. First, we demonstrate the QD behavior of the CNT by usual transport measurements, as shown in figure 4.4 b. In figure 4.4 c we show how the SET reflects the charge state of the CNT-QD. The effect of single electrons added to the CNT-QD can be seen in the current through the Al-SET. The charge of a single electron, added to the CNT-QD, causes a phase shift in the Coulomb oscillation of the SET and thereby a change in  $I_{SET}$ . For a bias voltage of  $50\mu V$  applied to the SET, a charge detection event corresponds to a change in  $I_{SET}$  of a few pA (if we are at the steepest slope of a SET Coulomb oscillation). We find a coupling of about  $\alpha_{NT,SET} = 0.08$ , i.e. one electron on the CNT-QD induces the equivalent of 0.08 electrons on the SET island. This is in good agreement with electrostatic simulations for such a device.

#### 4.4.1 Noise and sensitivity

We have fabricated a number of devices and estimated the SET sensitivity in the low frequency range. We have measured the noise at the operation point with a bandwidth of  $\sim 10Hz$  and assumed a white noise spectrum at these frequencies to calculate the sensitivity. For our SET charge detectors, we usually find a coupling of  $\alpha_{NT,SET} = 0.01 \dots 0.2$ , limited by the distance between CNT-QD and SET. The accuracy of the AFM imaging of the CNT positions and the alignment precision of the ebeam lithography require a minimal distance between SET and CNT of about 150nm.

The SET sensitivity to electrons *on the SET island* is typically between  $10^{-2}e^-/\sqrt{Hz}$  and  $10^{-4}e^-/\sqrt{Hz}$  for our devices. The theoretical limit for a SET with similar device parameters as ours is  $\sim 10^{-5}e^-/\sqrt{Hz}$  [70, 71]. This limit describes the ideal situation where the sensitivity is limited by the SET's own shot noise. Therefore, for our SETs there must be other noise sources which are dominating, probably charge noise in the environment. Also a better control over the tunnel

junction transparency and symmetry could improve the SET sensitivity. For the sensitivity to electrons on the CNT-QD we find values of  $10^{-1} - 10^{-2} e^- / \sqrt{Hz}$ , demonstrating the good quality of our charge detectors.

#### 4.4.2 Active feedback

From equation 4.5 it follows that the sensitivity is largest when the SET is at the steepest point of its Coulomb oscillation (= point of maximal sensitivity). For a Lorentzian peak shape, this point is at approximately three quarters of the maximum peak height. To operate the charge detector efficiently it is important to keep it at this point of maximal sensitivity. A typical experiment measures the charge state of the CNT-QD as a function of one or several gate voltages. However, these gates also have a capacitance to the SET and therefore can move it away from its point of maximal sensitivity. To compensate for this effect we can use linear compensation and change the voltage on the SET side gate (which couples mainly to the SET and has a very weak coupling to the CNT-QD). However, we find in practice this approach not to work sufficiently precise, especially when more than one gate voltage is changed. Therefore, we use active feedback instead.

To keep the SET at the point of maximal sensitivity, we have incorporated a feedback loop in our measurement software. We use the SET sidegate to keep  $I_{SET}$  at a value  $I_{const}$ , corresponding to maximal sensitivity. The feedback is then simply realized by modifying the voltage on the SET-sidegate by an amount  $\Delta V_{SET}$  on each measurement step:

$$\Delta V_{SET} = (I_{SET} - I_{const})G \quad (4.6)$$

G is here the gain of the feedback loop. For positive G, the feedback loop will converge to a point where  $I_{SET} = I_{const}$  and  $dI_{SET}/dV_{SET} < 0$ . The numeric value of G has to be chosen, taking specific parameters of the experiment into account (coupling of the gate to the SET, sweep speed of the performed measurement).

Now, charging events of the CNT-QD appear in the feedback signal instead of in  $I_{SET}$  (figure 4.5).

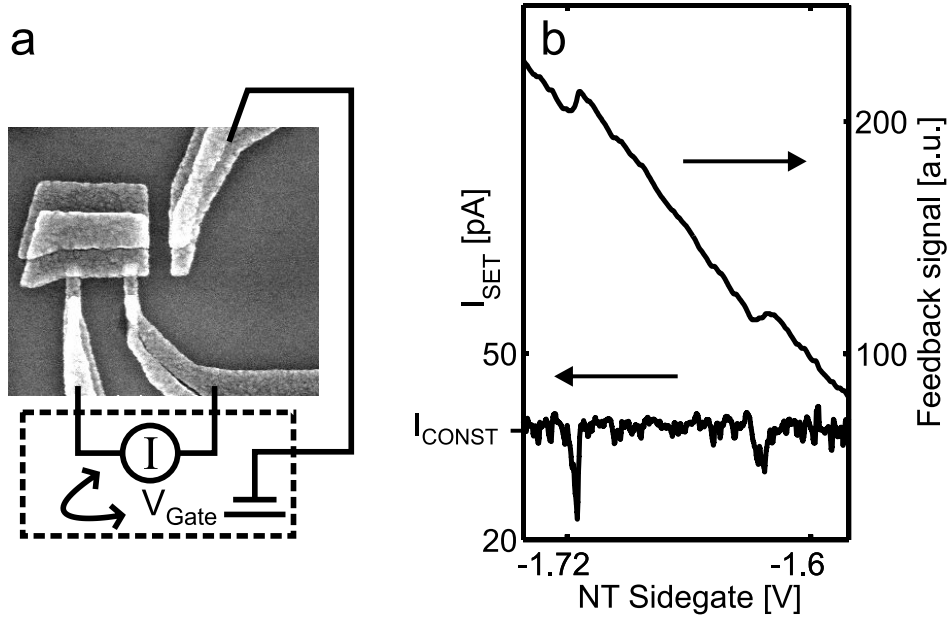


**Figure 4.5: Active feedback** (a) Working principle of the feedback loop: The voltage on the SET gate is constantly adjusted to keep  $I_{\text{SET}}$  at a constant value. (b) Feedback signal and  $I_{\text{SET}}$  during a measurement, where we use the NT sidegate to change the electron number on CNT-QD.  $I_{\text{SET}}$  is kept at a  $I_{\text{CONST}}$  by adjusting the voltage on the SET-sidegate. The feedback signal has a constant slope (compensation for the cross-coupling from the NT sidegate). The charging events now appear as sharp steps in the feedback signal.

#### 4.4.3 Quantum dots at the end of a CNT

Finally we demonstrate the use of the SET charge detector by looking at a system not accessible to transport measurements at all: A CNT-QD connected to only one lead [72], as shown in figure 4.6. Again, we have fabricated an Al-SET in close proximity to the CNT. Phase shifts in  $I_{\text{SET}}$ , of regular magnitude and comparable to the ones showed in figure 4.4, appear as a function of the side gate voltage. This suggests strongly that we detect single electrons, added to the CNT segment. Measuring these charging events as a function of both side gates (measurement not shown here) shows that the electrons in fact are added to a double QD potential in the CNT.

Furthermore, in chapter 6 we present the use of Al-SETs for real time charge detection, determination of tunneling rates and excited state spectroscopy.

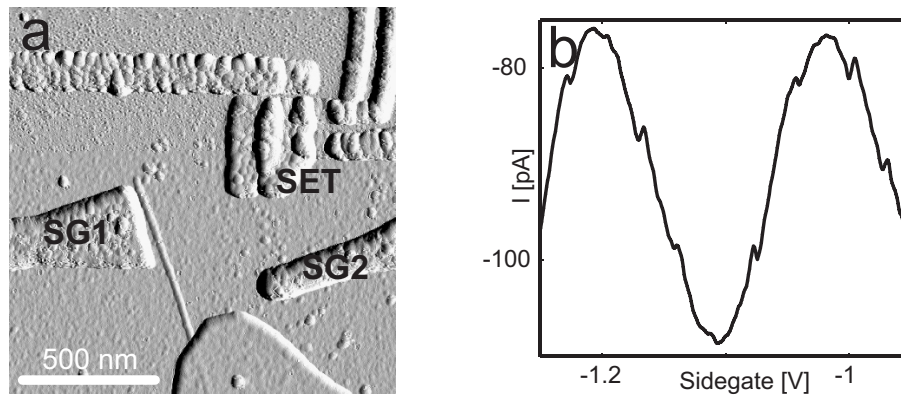


**Figure 4.6: A QD at the end of a CNT** (a) AFM image of the end section of a CNT connected to one metal contact. Two gates allow to tune the electrical potential on the CNT. Nearby, an Al-SET is fabricated. (b) Current through the SET as a function of the voltage applied to one of the gates. Sudden changes in the current are visible, comparable to those in figure 4.4





# Chapter 5

## Coupling effects between a carbon nanotube quantum dot and a SET charge detector

We describe coupling effects between a CNT-QD and a SET charge detector. We present experimental data showing that the backaction from the SET to the CNT-QD is very small, even for a large electrical current passing through the SET. On the other hand, a similar or even smaller current passing through the CNT has a huge effect on the SET. We explain this asymmetry by the difference in charging energies of the two device components and discuss possible mechanisms for this effect.

## 5.1 Introduction and device

In the previous chapter, we have described how an Al-SET can be used to detect single electrons in a CNT-QD. Here, we examine the backaction between the Al-SET and the CNT-QD. Measurements have been carried out in a dilution refrigerator with a base temperature of 40 mK. To keep the Al in the normal conducting state, a magnetic field of 0.5 T is applied in all measurements presented in this chapter. The device and the working principle of the charge detection are shown in figure 5.1. The coupling from the CNT-QD to the SET is  $\alpha_{NT,SET} = 0.08$ , i.e. one electron added to the CNT-QD induces a charge of 0.08 electrons on the SET island. For a more extensive discussion, we refer to the previous chapter.

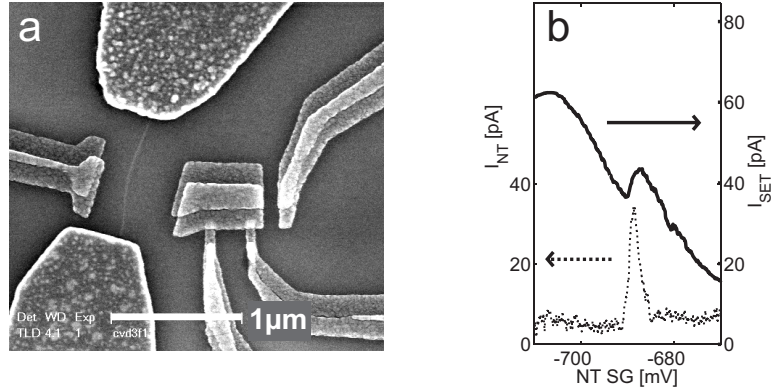


**Figure 5.1: Carbon nanotube with SET charge detector** (a) Scanning electron micrograph of a CNT device with a SET charge detector. The distance between the CNT and the SET is around 400nm. (b) Simultaneous measurement of  $I_{CNT}$  and  $I_{SET}$ . Bias voltages of 1 mV and  $75\mu V$  are applied to the CNT and SET, respectively. The charge of one electron, added to the CNT-QD, causes a phase shift in the Coulomb oscillations of the SET and thereby a change in current. This is due to the capacitive coupling between the two device components.

## 5.2 Backaction effects

We have investigated how the two device components, the CNT-QD and the SET, influence each other besides the charge detection. In particular, we examine the effect of an electrical current passing through one device component on the other

component. Such a measurement is shown in figure 5.2.

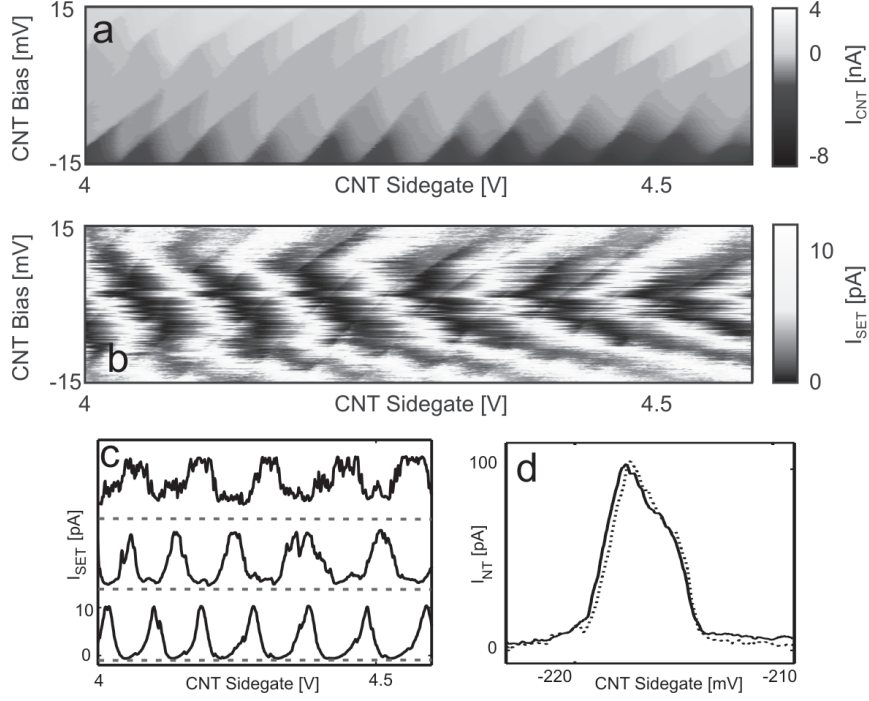


**Figure 5.2: Backaction** (a)  $I_{CNT}$  as a function of applied gate voltage and bias. Coulomb diamonds with a charging energy of  $\sim 10\text{meV}$  indicate a single QD. (b) Measurement of  $I_{SET}$ , performed simultaneously to (a).  $I_{SET}$  is measured as a function of applied gate voltage and CNT bias. The bias voltage applied to the SET is  $20\mu\text{V}$ . The large scale oscillations are Coulomb oscillations, resulting from the direct coupling of the gate to the SET. Furthermore, a huge effect of  $I_{CNT}$  on the SET can be seen: A high  $I_{CNT}$  causes both a higher noise in  $I_{SET}$  and also an increase of  $I_{SET}$  in its Coulomb valleys. (c) Line cuts through (b) for bias voltages of 0, 7.5 and 15 mV applied to the CNT, respectively. Traces have been offset for clarity, the dashed lines indicate the zero current level for each trace. A high  $I_{CNT}$  both raises level of  $I_{SET}$  in its Coulomb valleys and increases the noise dramatically. (d) A Coulomb peak in  $I_{CNT}$  for SET bias voltages of 0 mV (solid line) and 1 mV (dashed line) (corresponding to  $I_{SET}$  being 0 and  $5\text{nA}$ , respectively). Backaction from the SET to the CNT is almost absent.

First, we look at the backaction from the SET to the CNT-QD. An electrical current through the SET,  $I_{SET}$ , has almost no effect on the Coulomb peak shape of the CNT-QD (figure 5.2 d). This is the case, even for  $I_{SET}$  being two orders of magnitude larger than during normal operation of the SET as a charge detector

1.

The situation changes dramatically when a current of similar magnitude is passing through the CNT. In figure 5.2 a and b, we show simultaneous measurements of  $I_{CNT}$ , the current through the CNT-QD, and  $I_{SET}$ . We measure these two currents as a function of the bias applied to the CNT-QD and the voltage on the CNT-sidegate. The SET bias is kept constant.  $I_{CNT}$  shows Coulomb diamonds, indicating a QD with a charging energy of  $\sim 10\text{meV}$  (figure 5.2 a). Outside the Coulomb diamonds,  $I_{CNT}$  increases up to  $+4\text{nA}$  ( $-9\text{nA}$ ) for  $+15\text{mV}$  ( $-15\text{mV}$ ) bias voltage. The SET shows two effects (figure 5.2 b): First, Coulomb oscillations are visible, due to the direct coupling of the CNT-sidegate to the SET island. But in addition, a huge effect of  $I_{CNT}$  on the SET is visible. A high  $I_{CNT}$  increases the noise in  $I_{SET}$  significantly and also raises the level of  $I_{SET}$  in its Coulomb valleys, i.e. it lifts the Coulomb blockade of the SET. These effects become most clear from figure 5.2 c, where we show  $I_{SET}$  as function of the voltage on the CNT-sidegate for different bias voltages applied to the CNT-QD.

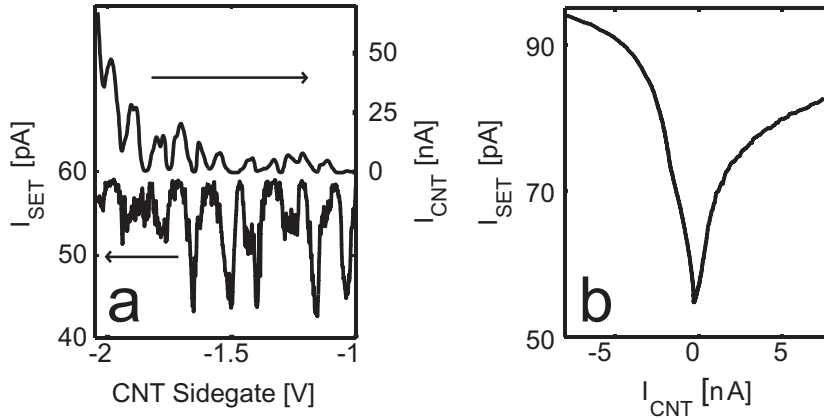


**Figure 5.3: Correlation between  $I_{CNT}$  and  $I_{SET}$**  (a) Simultaneous measurement of  $I_{CNT}$  (top) and  $I_{SET}$  (bottom) in a region in gate space where  $I_{CNT}$  varies strongly with the applied gate voltage. It is apparent that a large  $I_{CNT}$  lifts the value of  $I_{SET}$  in its Coulomb valleys while the value of  $I_{SET}$  at its Coulomb peaks remains unchanged. (b)  $I_{SET}$  inside its Coulomb valley as a function of the current through the CNT-QD. SET-bias:  $50\mu\text{V}$ . The asymmetry for positive and negative currents is probably caused by an asymmetry of the two contacts to the CNT.

<sup>1</sup>If we operate the SET as a charge detector, typical currents are of the order of  $50\text{pA}$ . In figure 5.2 d, we have  $I_{SET} \approx 5\text{nA}$

The clear correlation between the magnitude of  $I_{CNT}$  and these backaction effects is illustrated in figure 5.3. In figure 5.3 a, we show a simultaneous measurement of  $I_{CNT}$  and  $I_{SET}$  as function of applied gate voltage; this time in a region of gate voltage, where  $I_{CNT}$  varies a lot with gate voltage (due to a changing charging energy of the CNT-QD). Figure 5.3 b summarizes how the magnitude of  $I_{SET}$  inside a Coulomb valley depends on  $I_{CNT}$ .

### 5.3 Mechanisms

First, we discuss the small backaction from the SET to the CNT-QD. We have already mentioned that one electron on the CNT-QD induces a charge of  $\alpha_{NT,SET} = 0.08$  electrons on the SET island. This coupling allows us to use the SET as a charge detector. However, there cannot be a working charge detector without a backaction [73, 74] to the QD. Basically, this follows from the symmetry of the capacitance matrix. An extra electron on the SET will induce a charge  $Q_{NT} = e C_{SET,NT}/C_{SET,\Sigma}$  on the CNT. Therefore, the coupling of the SET to the CNT is given by:

$$\alpha_{SET,NT} = \frac{Q_{NT}}{Q_{SET}} = \frac{C_{SET,NT}}{C_{SET,\Sigma}} = \alpha_{NT,SET} \frac{C_{NT,\Sigma}}{C_{SET,\Sigma}} \quad (5.1)$$

From the charging energies of the CNT-QD ( $\sim 7.5$  meV) and the SET (0.1 meV), we get  $C_{NT,\Sigma}/C_{SET,\Sigma} = 0.013$ , which gives  $\alpha_{SET,NT} \approx 0.001$ . This means the backaction effect of the SET on the CNT-QD is expected to be very small (if we compare to the “action” from the CNT-QD to the SET). And indeed, this is what we observe (figure 5.2 d). For the use as a charge detector this is desirable, since the backaction of the detector to the QD should be as small as possible. The reason for the small backaction is the small charging energy of the SET in comparison to the CNT-QD. Replacing the SET with an object with larger charging energy (e.g. a second CNT-QD) would therefore worsen these kind of backaction effects (or one has to decrease the coupling  $C_{NT,SET}$ ).

Now, we discuss the huge effect of  $I_{CNT}$  on the SET. First, we would like to point out that the much larger effect of the CNT on the SET than vice versa can be understood from the difference in charging energies of these two device components (figure 5.4a). To gain more insight in the specific processes that take place, we discuss two mechanisms: (i) Effective heating due to the fluctuating electron number on the CNT-QD and (ii) A photoionization process that can lift

Coulomb blockade

### Effective heating

When a current is passing through the CNT-QD, the electron number on the CNT-QD,  $N_{NT}$ , is fluctuating by  $\Delta N_{NT}$ . The value of  $\Delta N_{NT}$  depends on the applied bias voltage. The fluctuating  $N_{NT}$  causes a fluctuating voltage on the SET island:

$$\Delta V_{SET} = e \Delta N_{NT} \frac{C_{SET,NT}}{C_{NT,\Sigma} C_{SET,\Sigma}} = e \Delta N_{NT} \alpha_{NT,SET} \frac{1}{C_{SET,\Sigma}} \quad (5.2)$$

This fluctuating voltage can be understood as an effective heating of the SET, since it smears out the energy over a range  $\Delta V_{SET}$  [75]. However, this energy range is smaller than  $E_C^{SET}$ , the charging energy of the SET, by a factor  $\Delta N_{NT} \times \alpha_{NT,SET} \approx \Delta N_{NT}/12$ . Note, that in figure 5.2 a and b, the bias voltage across the CNT is less than twice the charging energy of the CNT-QD, meaning  $\Delta N_{NT} \leq 2$  (if we neglect higher order tunneling processes). This means the Coulomb oscillations should be smeared out over a range not larger than  $\sim 1/6$  of a Coulomb oscillation. So it seems that this mechanism alone cannot explain the huge effects we observe.

### Photoionization

The stochastic nature of electron tunneling causes the current through a QD to exhibit temporal fluctuations, i.e shot noise. The shot noise can induce a current through the SET inside the Coulomb blockade region via a photoionization process [76]. An electron on the SET can absorb energy and leave the island; subsequently a transient current can flow through the SET as long as the SET is not in its ground state again, as shown in figure 5.4b. Since there is no quantized excitation spectrum for a SET, this process can lead to a transient current at any gate voltage setting (in contrast to a QD, where an excited state needs to be resonant, in order to have a current flowing [76]). Since a SET has no quantized energy spectrum, we expect no energy dependence of the tunneling rate (in a QD, there can be a huge difference of the tunneling rates into ground states and excited states [76]).

The shot noise spectral density of  $I_{CNT}$ ,  $S_I$ , can be expressed as  $S_I = 2eI_{CNT}F$ .  $F$  is the Fano factor, which for elastic transport through a QD is between  $F = 0.5$  (symmetric barriers) and  $F = 1$  (highly asymmetric barriers) [77]. For inelastic

cotunneling through a QD,  $F$  can also exceed 1 [78].  $S_I$  has a white spectrum with a cut-off frequency,  $\nu_{CO}$ , which is given by  $\nu_{CO} = eV/h$ , corresponding to the maximum frequency that can be emitted. Here  $V$  is the maximum voltage drop that occurs for a tunneling event, such that  $V \leq V_{Bias}^{CNT}$  (depending on the configuration of the QD). A more extensive discussion can be found in [79].

Let us have a look at the parameters of this process for our experiment. Due to the small charging energy of the SET,  $E_C^{SET} = 0.1$  meV, the photoionization process can lift the Coulomb blockade of the SET in its valleys already for very small bias voltages applied to the CNT: already for  $V_{Bias}^{CNT} \geq E_C^{SET}/e$ , the photoionization process can take place across the entire Coulomb blockade region of the SET. Furthermore, the increase of the shot noise spectral density  $S_I$  with  $I_{CNT}$  is consistent with the increase of  $I_{SET}$  inside its Coulomb valleys with  $I_{CNT}$  (figure 5.3 b).

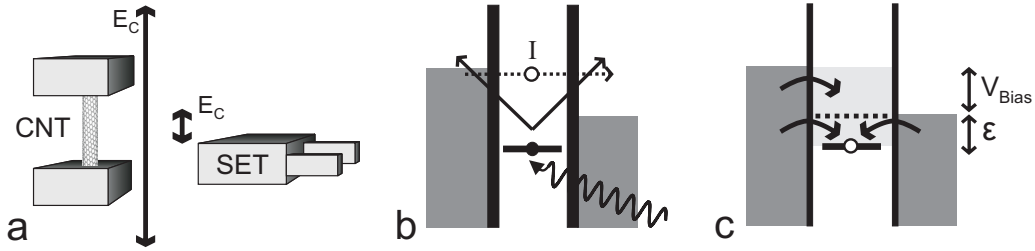


**Figure 5.4:** (a) The large difference in charging energies between the CNT-QD and the SET is the reason for the asymmetry in backaction between these two device components (b) Schematic of the photoionization process: A photon is absorbed by an electron on the SET island, giving it enough energy to leave the island. Subsequently, Coulomb blockade is lifted and a transient current can flow. (c) Different tunneling processes that can take place when the SET island is ionized. There is no quantized energy spectrum; an electron can tunnel on the SET at any energy inside the gray energy window. If an electron enters at an energy below the dashed line, the SET is in Coulomb blockade again. If it enters above the dashed line, it can tunnel out to the right and thereby contribute to the transient current.

## Conclusions

We have investigated how a CNT-QD and a SET charge detector influence each other. The backaction from the SET to the CNT-QD is found to be very small due to the huge difference in charging energies between these two device components. This is very favorable for the use of the SET as a charge detector. On the other hand, we found that a current passing through the CNT-QD has a huge

effect on the SET. We discussed two mechanisms for this effect: effective heating due to direct gating of a SET by the fluctuating charge on the CNT-QD and a photoionization process. In fact, the SET can be used as a detector for the shot noise in the current through the CNT-QD, similar to the experiment presented in [76]. However, since during operation of the SET as a charge detector the current through the CNT-QD is typically very small, this effect does not spoil the charge detection itself.



# Chapter 6

## Real time electron tunneling and pulse spectroscopy in carbon nanotube quantum dots

G. Gotz, G.A. Steele, W.E. Vos & L.P. Kouwenhoven

We investigate a Quantum Dot (QD) in a Carbon Nanotube (CNT) in the regime where the QD is nearly isolated from the leads. An aluminum single electron transistor (SET) serves as a charge detector for the QD. We precisely measure and tune the tunnel rates into the QD in the range between 1 kHz and 1 Hz, using both pulse spectroscopy and real - time charge detection and measure the excitation spectrum of the isolated QD.

---

This chapter (except section 6.5) has been published in Nano Letters, vol. 8 (11), p.4039 - 4042 (2008)

## 6.1 Introduction and device fabrication

A quantum dot (QD) defined in a carbon nanotube (CNT) is a very interesting and unique physical system for studying individual electron spins [20, 21, 22, 23, 80, 81]. In particular, the spin relaxation and coherence times are expected to be as long as seconds [23, 80], which makes this system attractive for quantum information processing. However, both precise control over the tunnel rate into a QD and real - time read out of the charge state of the QD have not been demonstrated yet for CNTs.

QDs can be defined in CNTs by using top gates (TGs) as shown in Figure 6.1. Suitable voltages applied to these TGs create local tunnel barriers in semiconducting CNTs. In this way, single and double QDs have been realized [28, 29, 82]. In this letter we use TGs to precisely tune the tunnel rates into a CNT-QD all the way down to  $\sim 1Hz$ . We use a metallic SET as a charge detector, sensitive to single electron charges in the CNT-QD [67, 68, 69], since transport measurements are not possible at such low tunnel rates. Finally, we measure the excitation spectrum of a nearly isolated CNT-QD. Samples are fabricated on highly p-doped Si substrates with 280 nm thermally grown silicon oxide, such that the Si substrate can serve as a global back gate (BG). CNTs are grown from Fe/Mo catalyst islands using chemical vapor deposition [61]. The CNTs are located with atomic force microscopy and CNTs with diameters  $< 4nm$  (probably single walled) are chosen for further sample fabrication. First, ohmic contacts are made with thermally evaporated Pd (15 nm). The entire sample is then coated with 35 nm  $Al_2O_3$ , deposited with Atomic Layer Deposition. Room temperature conductivity measurements as function of applied BG voltage allow us to select semiconducting CNTs. We define two TGs and one SG by evaporating Ti/Au (10/20 nm). In close proximity ( $< 500nm$ ) to the CNT we fabricate an aluminum single electron transistor (SET) using a standard double angle evaporation technique [60]. Figure 6.1a shows an atomic force microscopy image of a device from the same fabrication run as the one from which we present data here. After evaporation of Ti/AuPd bonding pads, devices are wire bonded and cooled down in a dilution refrigerator with a base temperature of 50 mK. The CNT-SG is connected to a bias tee (at room temperature), allowing us to apply DC- and AC-voltages at the same time to this gate. We show data from one device, but similar circuits have been realized three times indicating the reproducibility of our approach.

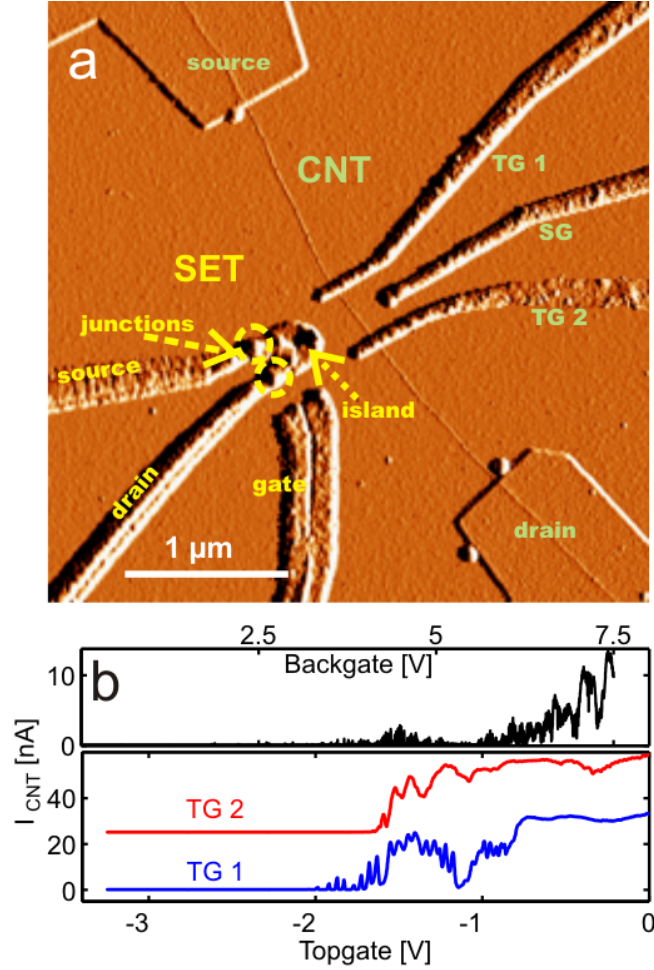


**Figure 6.1: Sample characterization** (a) Atomic force microscopy picture of a device similar to the one from we present measurements here. The semiconducting CNT is contacted with Pd ohmic contacts, separated by  $\sim 3\mu\text{m}$ . Two 40 nm wide top gates (TG1 and TG2) cross the CNT with a 400nm separation with a side gate (SG) located between them. On the lower side of the picture, an Al - SET is fabricated close to the CNT segment between the two TGs. (In contrast to the measured device, this picture shows a sample with a dielectric only below the TGs instead of an  $\text{Al}_2\text{O}_3$  layer covering the entire sample. Therefore, the CNT is clearly visible here.) (b) Top: Current through the CNT ( $V_{SD}^{CNT} = 2\text{mV}$ ) as function of applied back gate voltage (all other gates at 0 V); bottom: current through the CNT ( $V_{SD}^{CNT} = 2\text{mV}$ ) as function of either the voltage applied to  $TG_1$  (blue) or  $TG_1$  (red). Traces are offset for clarity. The other TG is set to 0 V, the back gate to 7.5 V. Both TGs pinch off the current for voltages  $\leq -2\text{V}$  whereas a large current flows for voltages  $\geq -0.75\text{V}$ . This demonstrates local, tunable barriers.

## 6.2 A tunable CNT QD with a SET charge detector

First, we characterize our device. Figure 6.1b shows the current through the CNT,  $I_{CNT}$ , versus back gate voltage, BG, and versus TG voltages. The two TGs show similar behavior, albeit with a smoother pinch-off curve for TG2. The oscillations in the trace for TG1 are likely due to disorder at low electron densities [28]. This residual disorder leads to resonances and charging effects in the small regions underneath the TGs.

Despite the remaining disorder, we create a QD in the CNT segment between the two TGs by choosing appropriate TG voltages (figure 6.2a, inset). The addition energy of a few meV is typical for a CNT-QD with a length of  $\sim 500nm$ , i.e. consistent with the distance between our TGs [28, 29, 82]. Moreover, we find that the QD couples equally to both TGs (measurements not shown here), which indicates that the QD is indeed formed between the two TGs. From the voltages applied to the BG and SG, we estimate the number of electrons in the CNT-QD,  $N$ , to be several 100. We use the SET as a charge detector for our CNT-QD [67, 68, 69]. The SET consists of a small aluminum island, connected to source and drain via  $Al_2O_3$  tunnel junctions, with a charging energy of a few  $100\mu eV$ . An additional gate allows us to tune the electrical potential on the SET island. In all measurements presented here, a perpendicular magnetic field of at least 0.2 T was applied, in order to keep the aluminum SET in the normal conducting state.

Figure 6.2a shows simultaneous measurements of the CNT-current,  $I_{CNT}$ , and the SET-current,  $I_{SET}$ , while changing the voltage on SG.  $I_{CNT}$  shows Coulomb peaks when one more electron is added to the QD.  $I_{SET}$ , shows two features: first, we see periodic Coulomb oscillations of the current, resulting from the capacitive coupling of the SG to the SET island. Additionally, these oscillations undergo a number of sharp phase shifts. The phase shifts coincide with the Coulomb oscillations of the CNT-QD and are caused by the additional electron charge on the CNT-QD. If this phase shift happens at a point of steepest slope of the oscillations in  $I_{SET}$ , the change in  $I_{SET}$  and thus the sensitivity is maximal. In all measurements, we apply an appropriate voltage to the SET side gate, such that the investigated electron transition of the CNT-QD coincides with the SET at a point of highest sensitivity. For this sample, the coupling between SET and CNT-QD is about 0.2 (i.e. adding one electron to the CNT-QD induces an effective charge of 0.2 electrons on the SET island). The low frequency sensitivity to electrons on the CNT-QD is about  $10^{-2}e/\sqrt{Hz}$ , demonstrating a high quality

of our charge detector. The sensitivity is obtained from noise measurements of  $I_{SET}$  at the operation point and is limited by the charge noise in our system.

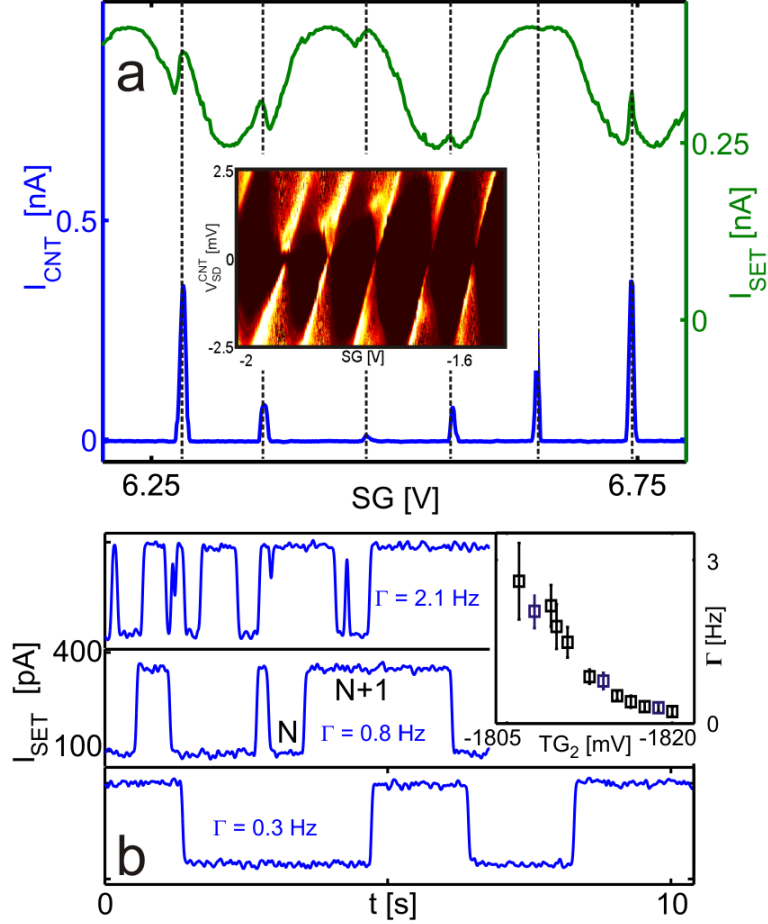


**Figure 6.2: Charge detection of single electrons in the CNT - QD** (a) Simultaneous measurement of the current through the CNT (blue,  $V_{SD}^{CNT} = 0.6mV$ ) and SET (green,  $V_{SD}^{SET} = 70\mu V$ ). Inset: differential conductance  $dI/dV$  of  $I_{CNT}$  as function of  $V_{SD}^{CNT}$  and SG voltage. Regular Coulomb diamonds indicate a single QD with an addition energy of  $\sim 3mV$ , formed between the TGs. (b) Real time detection of electron tunneling into the CNT-QD. Almost entirely pinched-off TGs result in extremely low tunneling rates, such that single tunneling events are visible in the SET-current. The two levels in the SET-current correspond to the two configurations of the CNT-QD being occupied with  $N$  or  $N+1$  electrons. The three traces are taken for different voltages, applied to  $TG_2$ . The other topgate is completely closed ( $TG_1 = -2400$  mV) while we use  $TG_2$  to precisely tune the tunneling rate into the QD to values around 1 Hz (top to bottom). Inset: Tunneling rate as a function of the voltage on  $TG_2$ . Rates are obtained from real-time traces. The blue data points correspond to the three traces shown in (b).

### 6.3 Real time charge detection

The charge sensing also works for opaque tunnel barriers. An extreme example is shown in figure 6.2b with a real-time measurement [68, 83, 84] of the SET-current when the CNT-QD potential is tuned close to a charge transition. We observe single electrons tunneling in and out the CNT-QD in real time with tunneling rates around  $\Gamma = 1Hz$ . The fact that we only see two stable levels in ISET over such long timescales demonstrates the excellent stability of the combined system of CNT-QD and charge detector. In particular, we do not observe any bistabilities or disturbing effects from nearby charge traps. We precisely control the tunneling rate by the voltages applied to the topgates (figure 6.2b, inset). This demonstrates that it is possible to tune the TG-controlled barriers to tunnel rates as slow as  $\Gamma \sim Hz$ , i.e. the interesting range of the expected life time of electron spins.

### 6.4 Pulse spectroscopy

Real-time detection of electron tunneling is a direct and elegant way for measuring tunneling rates of nearly closed QDs. However, it is time consuming in terms of data analysis and technically demanding already for frequencies in the kHz range or higher. A more efficient data taking technique is based on a Lock-In (LI) measurement as reported by Elzerman et al. [85] Again, we first pinch off one barrier completely by applying a sufficiently negative voltage to TG1 (the barrier with more disorder is now completely closed). We then tune TG2 to a desired tunnel rate. The CNT source and drain are both kept at ground potential and the SET charge detector is operated at a point of maximal charge sensitivity. Additional to the DC voltage, we apply a square pulse with equal up-down-times,  $\tau$ , to SG. We measure the SET response to this pulse train using a LI measurement at frequency  $f = 1/2\tau$ . We denote this response as the SET-LI signal. Schematically, the method is shown in figure 6.3. The essential point is that electron tunneling into and out of the CNT-QD causes a dip in the SET-LI signal.

This depth of the dip depends strongly on the ratio of the pulse frequency,  $f$ , and the tunneling rate,  $\Gamma$ : If  $f \ll \Gamma$ , there is enough time for an electron to tunnel into the QD during the high phase of the pulse. In this case the dip has a 100% depth. Raising  $f$  above  $\Gamma$ , electron tunneling becomes too slow to occur within a pulse cycle. As a result the dip depth will gradually decrease when increasing  $f$  compared to  $\Gamma$ . Analytically, the dip depth is proportional to  $1 - \pi^2/(\Gamma^2\tau^2 - \pi^2)$ , under the assumption that rates for tunneling in and out are equal [85].

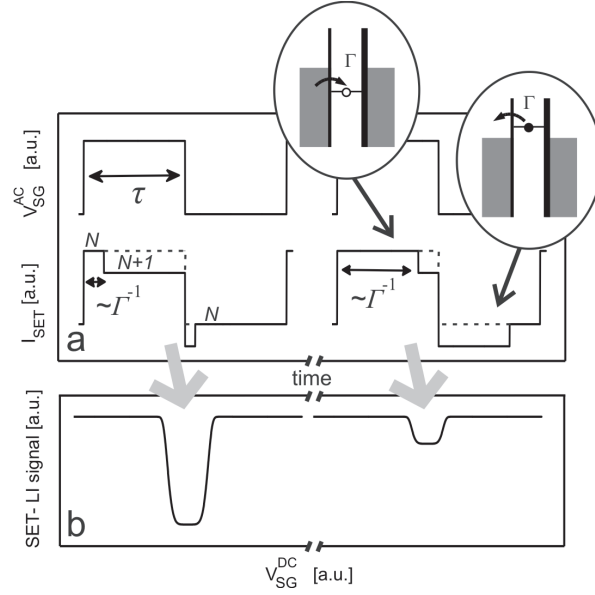


**Figure 6.3: Pulse spectroscopy scheme to determine the tunnel rate  $\Gamma$**  (a) Square pulses with equal up and down times,  $\tau$ , are applied to the SG (top). Bottom: Schematic response of  $I_{SET}$  to the pulse train. When the electron number on the CNT-QD remains constant (away from the charge transition),  $I_{SET}$  is only changed via the cross-coupling to the SG (dashed line). However, if we set the value of the SG voltage close to a charge transition of the CNT-QD, electron tunneling will also affect  $I_{SET}$ . During the high phase of the pulse an electron can tunnel into the QD on a timescale  $\Gamma^{-1}$  (the tunnel rate through the open barrier) and leave it again during the low phase. This lowers (raises)  $I_{SET}$  during the high (low) phase of the pulse (solid line) To illustrate why this method is sensitive to the tunnel rate, we plot  $I_{SET}$  for a high tunnel rate ( $\Gamma \gg f$ , left) and a lower tunnel rate ( $\Gamma \geq f$ , right). The schematic energy diagrams show the electrochemical potential of the CNT-QD. (b) Expected SET Lock-In (LI) signal as function of the DC voltage applied to the SG. The SET signal is measured with a LI technique at frequency  $f = 1/2\tau$ . Without electron tunneling, the SET-LI signal stays constant. If electrons tunnel in and out the CNT-QD with a rate  $\Gamma \gg f$ , the SET-LI signal is lowered and shows a deep dip (left). If  $\Gamma \geq f$  (right), the dip is less deep. And finally, if  $\Gamma < f$ , electron tunneling is too slow to occur within a pulse cycle and the dip will disappear completely. Therefore, measuring the SET-LI signal as a function of pulse frequency,  $f$ , allows us to determine  $\Gamma$ .

Figure 6.4a shows the SET-LI signal for different pulse frequencies. For low  $f$  the effect of electron tunneling is large (pronounced dip) while the dip gradually disappears when raising  $f$ . From the fit in figure 6.4c we obtain a tunnel rate  $\Gamma = 1.4kHz$ . In order to set a desired value for the rate, we tune the voltage on TG2. Indeed, figure 6.4b shows that the size of the dip can be set to any value, each value corresponding to a particular rate. Again, this demonstrates the pre-

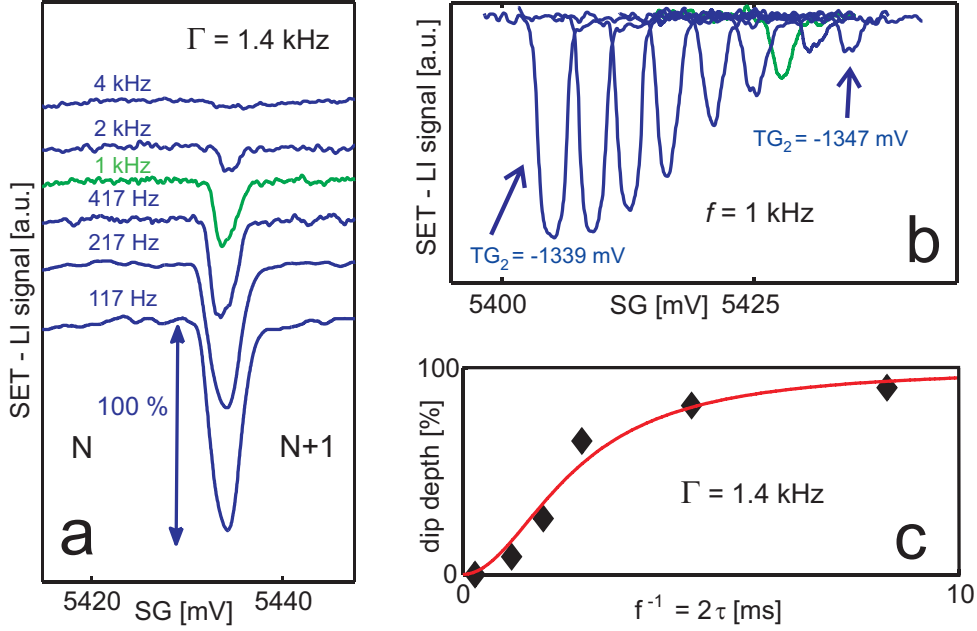


**Figure 6.4: Tuning and measuring the tunnel rate  $\Gamma$**  (a) SET-LI signal for different pulse frequencies  $f = 1/2\tau$  as a function of the DC-voltage applied to the SG. The SET is set to a configuration of highest sensitivity. For low pulse frequencies we observe a deep dip due to electron tunneling into the CNT-QD. At higher frequencies the dip gradually disappears. Curves are offset for clarity. (b) SET-LI signal for a fixed pulse frequency  $f = 1$  kHz for different voltages applied to TG2. By lowering the voltage at TG2 (from left to right), the dip becomes less deep. This shows that the tunnel rate into the CNT-QD changes from  $\Gamma \gg 1kHz$  ( $TG_2 = -1339$  mV) to  $\Gamma \leq 1kHz$  ( $TG_2 = -1347$ ) (note that when lowering the voltage on TG2, the charge transition moves to a higher SG voltage due to the capacitive coupling of TG2 to the CNT-QD). The green curves in a and b are taken at the same gate voltage and pulse frequency. We have used  $TG_1 = -1800$  mV and  $BG = 5$  V. (c) Fit of the analytic expression for the dip depth in the LI signal to the measured data from a. The fit gives a tunnel rate  $\Gamma = 1.4kHz$ . The 100% scale corresponds to the 100% arrow in a.

cise control over the tunnel rate in the interesting range of very long timescales. So far we have only considered tunneling into the ground state (GS) of our CNT-QD because we used relatively low pulse amplitudes. In the following, we investigate excited states (ES) of our closed CNT-QD. We use the same pulse spectroscopy scheme as described above, but apply larger pulse amplitudes [85]. Now, we observe a shoulder-like feature in the dip of the SET-LI signal (figure 6.5a). This feature is due to an ES of the CNT-QD: If the pulse amplitude exceeds the splitting between GS and ES, the effective tunneling rate into GS and ES is larger than the rate into the GS only. This results in a deeper dip in the



SET-LI signal.

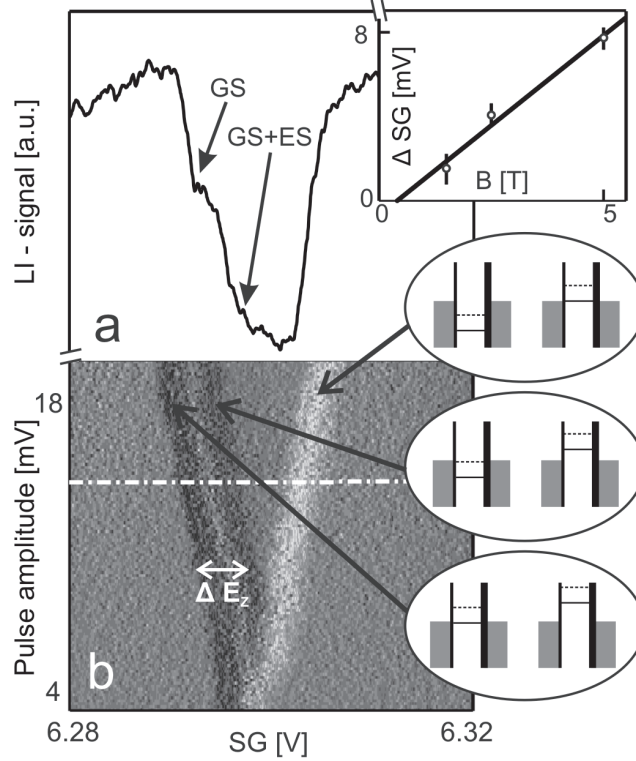


**Figure 6.5: Excited state spectroscopy** (a) SET-LI signal for a high pulse amplitude of 15 mV at  $B = 2.5\text{T}$ . The gate settings are  $BG = 6.25\text{ V}$ ,  $TG1 = -2225\text{ mV}$ ,  $TG2 = -1870\text{ mV}$  and the pulse frequency is  $f = 0.5\text{ kHz}$ . The dip now shows a shoulder like feature which is due to an increased tunnel rate into the CNT-QD when an excited state becomes accessible. Tunneling into both GS and ES state has a higher effective tunnel rate than tunneling into only the GS. Therefore, the dip becomes deeper when tunneling into the ES becomes energetically possible as well. **Inset:** splitting between GS and ES as function of magnetic field (b) Derivative with respect to the sidegate voltage of the SET-LI signal as function of the DC voltage on the SG and pulse amplitude. Three lines are visible, whose meaning become clear when comparing to the single trace in (a) and the schematic energy diagrams at the high and low phases of the pulse. The leftmost black line represents the onset of tunneling into the GS (lowest energy diagrams). The middle black line (which runs parallel to the first line) indicates where the dip becomes deeper because tunneling into the ES is possible as well (middle energy diagrams). The rightmost white line shows the end of the dip (highest energy diagrams). The Zeeman splitting between GS and ES is indicated with the white arrow. The trace in (a) is taken along the dashed-dotted line.

In figure 6.5b we plot the derivative of the SET-LI signal as function of pulse amplitude and DC voltage on the SG. The excited state appears as a line, par-

allel to the onset of the dip. The distance between this line and the onset of the dip is the energy difference between GS and ES, converted to SG voltage by a factor  $\alpha$ , the capacitance lever arm of the SG to the CNT-QD. We identify the nature of the excited state by investigating its dependence on perpendicular magnetic field. We find that the splitting between GS and ES depends linearly on the magnetic field (figure 6.5a, inset). Therefore, we conclude that GS and ES are spin-up and spin-down states of the same orbital level in the CNT-QD. Indeed, we expect that the Zeeman splitting at a magnetic field of a few Tesla is much smaller than orbital excitations. If we assume a length of 500 nm for our CNT-QD, the orbital level spacing is on the order of meV [28, 29]. For the Zeeman splitting  $E_Z = g\mu_B$ , however, we expect  $E_Z = 0.3meV$  at  $B = 2.5$  T (assuming  $g = 2$  [21, 27, 86]). We can use the energy of the Zeeman splitting to obtain the lever arm  $\alpha$  of the SG to the isolated CNT-QD and find  $\alpha = 0.065$ .

In conclusion, we have investigated a CNT-QD that is nearly isolated from its leads. We have used an aluminum SET as a charge detector to read out the charge state of the isolated CNT-QD and measured the tunnel rate into the CNT-QD using both real-time charge sensing and pulse spectroscopy. We have found that it is possible to tune an individual tunnel barrier with high accuracy to very low tunnel rates, comparable to the expected spin relaxation and coherence times in CNTs. Finally, we measured the spin states of the nearly closed CNT-QD. We acknowledge technical assistance from R. Schouten, B. van der Enden and R. Roeleveld. We thank R. Hanson for discussions, C. M. Marcus and H. Churchill for allowing the use of their ALD - deposition equipment and M. Rinkiö for experimental help and discussion.

## 6.5 Upper bound for the spin relaxation time $T_1$

Finally, we want to comment on our attempts to measure the spin relaxation time  $T_1$ . We have applied a three step pulse scheme as described in the Appendix to measure  $T_1$  using an averaging charge detector technique. We found that for waiting times  $T_W \geq 500\mu s$  after injecting an electron into a statistical mixture of GS (spin-down) and ES (spin-up) there was no measurable fraction left in the ES. That means all electrons have relaxed to the GS (spin-up) within this time. We know, that we have injected a substantial fraction into the ES from the LI-measurements described above. Thus, our findings set an upper bound for the

spin relaxation time:  $T_1 < 200\mu s$ .<sup>1</sup> We have carried out this measurement at magnetic fields between 1.5 and 8 T and for different electron numbers  $N$  on the CNT-QD.

This is in agreement with measurements of the singlet-triplet relaxation time in a  $^{13}C$  CNT, where the longest obtained relaxation time was  $4\mu s$  [41]. Theoretically, much longer spin relaxation times (several ms up to s) are expected, both for spin-orbit interaction [23] and hyperfine interaction with the carbon nuclei [80] as the spin relaxation mechanism. Possible reasons that  $T_1$  is considerably shorter in our case could be for example: (i) interactions of the electrons with the surrounding dielectric (ii) A different confinement potential, compared to the calculations in [23] (iii) Additional relaxation mechanisms (e.g. spin-orbit mediated deflection coupling [87]).

It would be interesting to measure  $T_1$  in a clean, suspended CNT, where the few electron regime can easily be reached and interactions with the environment are minimized due to the suspended sample geometry.

---

<sup>1</sup>our sample and measurement setup did not allow for resolving shorter  $T_1$  's with the used charge detection technique.



# Chapter 7

## Tunable few-electron double quantum dots and Klein tunnelling in ultra-clean carbon nanotubes

G.A. Steele, G. Gotz & L.P. Kouwenhoven

Quantum dots defined in carbon nanotubes are a platform for both basic scientific studies [29, 48, 82, 88, 89] and research into new device applications [90]. In particular, they have unique properties that make them attractive for studying the coherent properties of single electron spins [21, 23, 24, 36, 38]. To perform such experiments it is necessary to confine a single electron in a quantum dot with highly tunable barriers, but disorder has until now prevented tunable nanotube-based quantum-dot devices from reaching the single-electron regime [29, 82, 88, 89]. Here, we use local gate voltages applied to an ultra-clean suspended nanotube to confine a single electron in both a single quantum dot and, for the first time, in a tunable double quantum dot. This tunability is limited by a novel type of tunnelling that is analogous to that in the Klein paradox of relativistic quantum mechanics.

---

This chapter has been published in Nature Nanotechnology, Vol. 4, p. 363 - 367 (2009)

## 7.1 Introduction and device fabrication

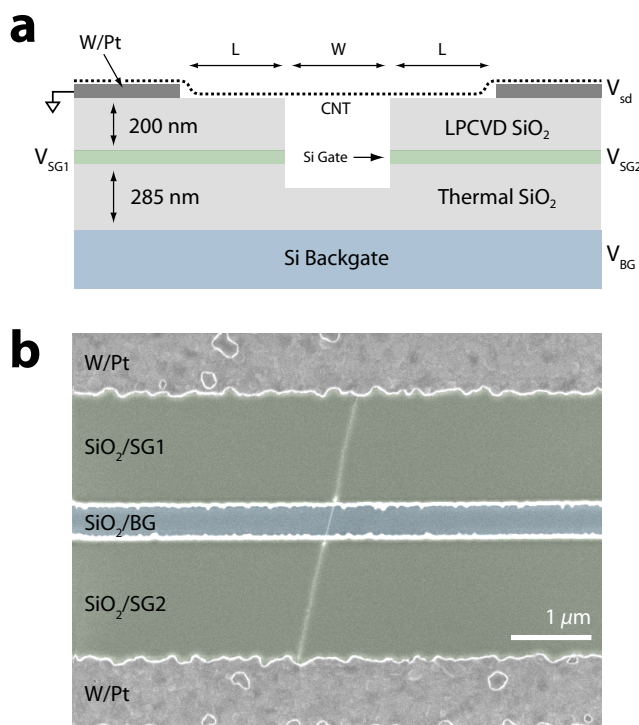


**Figure 7.1: Integrating local gates with ultra-clean carbon nanotubes.** (a) A schematic of the device. A predefined trench is etched to create two splitgates from a 50 nm thick n++ polysilicon gate layer between two silicon oxide layers. A Pt metal layer is deposited to act as source and drain contacts, and a nanotube is then grown from patterned catalyst. Device D1 has  $L = 1.5 \mu\text{m}$ ,  $W = 300 \text{ nm}$ , and D2 has  $L = 300 \text{ nm}$ ,  $W = 500 \text{ nm}$ . (b) In a subset of devices, a single nanotube bridges the trench, contacting the metal source and drain electrodes, as shown in this coloured SEM micrograph. The micrograph shows an example of a device with the same dimensions as device D1.

Single spins in carbon nanotube quantum dots are expected to be very stable against both relaxation and decoherence [23]. Nuclear spins, the principal source of spin decoherence [38, 36] in GaAs, can be completely eliminated and, furthermore, a strong spin-orbit interaction recently discovered in carbon nanotubes [21] enables all-electrical spin manipulation [23, 24], while preserving long spin relaxation and decoherence times [23]. Electron spins in carbon nanotube quantum dots are therefore attractive for implementation of a quantum bit (qubit) based on spin for applications in quantum-information processing [90]. In double quan-

tum dot systems, precise control of the tunnel coupling between the two quantum dots, and between the quantum dots and the leads attached to them, is critically important for spin readout schemes [48, 91, 92], and also to prevent loss of spin and phase information through exchange of an electron with the leads.

Double quantum dots can also be used to explore novel quantum tunnelling phenomena. In Klein tunnelling [93, 94, 95], for example, an electron tunnels with a high probability through a long and tall potential energy barrier when the height of the barrier is made comparable to twice the rest mass of the electron. It is not feasible to create such a barrier for free electrons due to the enormous electric fields required, but the low effective rest mass of the electrons in small bandgap nanotubes makes the observation of such Klein tunnelling in nanotube devices possible [95].

By depositing metallic gates isolated by a dielectric layer on top of a nanotube, several groups have demonstrated tunable double quantum dots in nanotubes lying on a substrate [29, 82, 88, 89]. These are tunable in the sense that the height and width of energy barriers between dots can be controlled by the gate. A disadvantage of this technique is that nanotubes in these devices suffer from significant disorder induced by the substrate and by the chemical processing required to fabricate the device. As the electron density is reduced, this random potential dominates and breaks the segment of nanotube into multiple disorder-induced “intrinsic” quantum dots before reaching the few-electron regime.

Wet etching of the device after fabrication to remove the substrate-induced disorder has been used previously to obtain single electron quantum dots in carbon nanotubes [13, 27], although experience has shown that the yield of such devices is quite low. Recently, a new fabrication method has been developed for producing ultra-clean quantum dots in suspended carbon nanotubes with a high yield in which all chemical processing is done before nanotube growth [57]. Studying single quantum dots in these devices has uncovered new carbon nanotube physics, including a strong spin orbit interaction due to the nanotube curvature [21] and evidence of Wigner crystallization of electrons at low density [52]. While devices fabricated in this way are extremely clean, they have some significant limitations: in particular, the confinement is produced only by Schottky barriers, which cannot be easily tuned in-situ. Furthermore, due to an insufficient number of local gates, it has not been possible to create a tunable double quantum dot in these ultra clean devices.

To overcome these limitations, we have developed a new method of integrating multiple local gates with the ultra clean fabrication. A schematic of the device is shown in Figure 7.1. As described in the Methods section, we grow a carbon nanotube over gates that are patterned in a thin doped silicon layer. Our cur-

rent design provides three independent gates, although fabrication can easily be modified to include a scalable number of gates inside the trench (see Supplementary Information). In this letter, we use these three gates in two different ways. In device D1, with  $L = 1.5 \mu\text{m}$ , the gates are used to define a single electron and single hole quantum dot where electrons and holes are confined by tunable  $pn$ -junctions instead of Schottky contacts. In device D2, with  $L = 300 \text{ nm}$ , we rely on tunnel barriers from the Schottky contacts, but now use the three gates to create a tunable single electron and single hole double quantum dot.

## 7.2 Single quantum dots defined by p-n junctions

In all previous measurements of quantum dots in carbon nanotubes containing a single electron, carriers were confined by Schottky barriers formed [21, 27] at the metal contacts, or by potentials defined from trapped oxide charges [13]. In figures 7.2 and 7.3, we demonstrate a single electron quantum dot defined only by gate voltages. We begin by applying a negative voltage to the splitgates, creating a p-type nanotube source and drain on top of the oxide. Sweeping the backgate voltage  $V_{\text{BG}}$ , shown in figure 7.2a, the current initially shows weak modulations from resonances in the leads when the suspended segment is p-type ( $ppp$  configuration), and is then completely suppressed as the suspended segment is depleted ( $pip$  configuration). As we sweep further, we form a  $pnp$  quantum dot showing clean Coulomb blockade, where single electrons in the suspended segment are confined by p - n junctions to the leads. Figure 7.2c shows a stability diagram as a function of both backgate and bias voltage, demonstrating that we have reached the single electron regime. As the confinement potential and doping profile are determined by our local gates, we can also confine single holes in an  $nnp$  configuration in the same device simply by inverting the gate voltages, shown in figure 7.2d. In figure 7.3e we show the current as a function of the backgate voltage and the voltage on the splitgates. In the left of the plot, the leads are doped p-type, and a positive backgate induces a single electron  $pnp$  quantum dot. In the right of the plot, the leads are doped n-type and a negative backgate induces a single hole  $nnp$  quantum dot. By adjusting the splitgate voltages, the  $pn$  junction width, and thus the tunnel barriers, can be tuned while keeping the electron number fixed (see figure 7.3f).



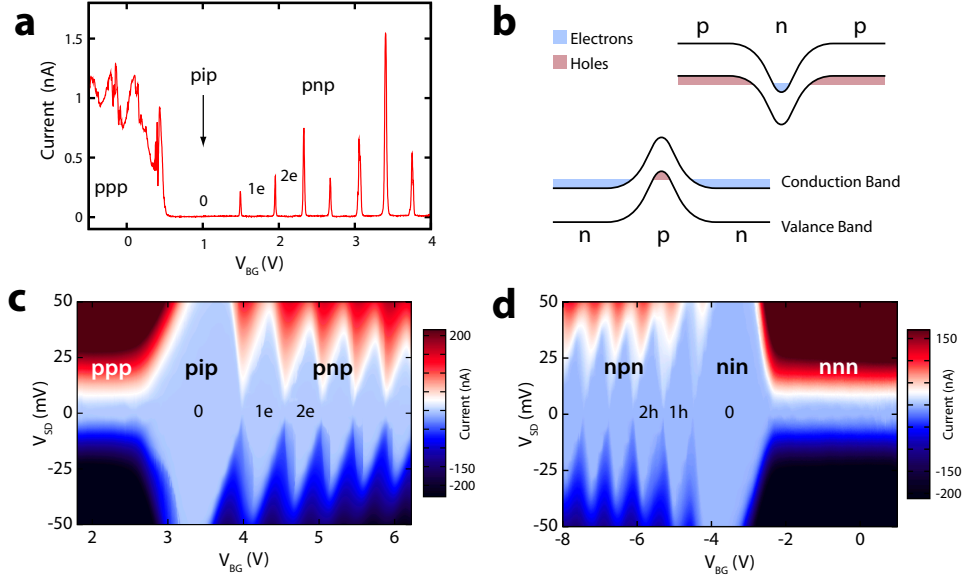


**Figure 7.2: Gate defined single-electron and single-hole quantum dots.** (a) Coulomb peaks of a *pnp* quantum dot in device D1 taken at a  $V_{SG1} = V_{SG2} = -50$  mV and  $V_{SD} = 1$  mV. The splitgates are used to dope the NT source and drain leads with holes. As  $V_{BG}$  is swept from negative to positive voltages, the suspended segment is depleted giving a *pip* configuration, followed by a *pnp* configuration as single electrons are filled in an n-type quantum dot, as illustrated in the energy diagrams in (b). (c) Stability diagram of the *pnp* dot: the charging energy of the first electron  $E_c^{1e} \sim 40$  meV is remarkably large due to the weak capacitive coupling of the suspended segment to the gates and the metal source drain layers. (d), The potential landscape in the device can be completely controlled by the gate voltages: by reversing the gate voltages, single holes are confined in a *nnp* configuration.

### 7.3 Few electron double quantum dots

In device D2, we use the gates in our design for a different purpose: here, we rely on less transparent Schottky contacts as incoming and outgoing tunneling barriers, and now use the backgate and the two splitgates as three independent local gates to create a double quantum dot potential in the nanotube with a tunable interdot coupling. Figure 7.4 shows the current through the device as a function of the two splitgate voltages. In the lower left and upper right regions of the plots, the two splitgates dope the two segments of the nanotube with carriers of opposite sign, resulting in a *pn* double quantum dot with an interdot barrier formed from a *pn* junction. In the upper left (bottom right) corner, the two splitgates dope both sides of the nanotube p-type (n-type). In figure 7.4a,  $V_{BG}$  is set to ground, which gives a potential in the middle of the nanotube that is

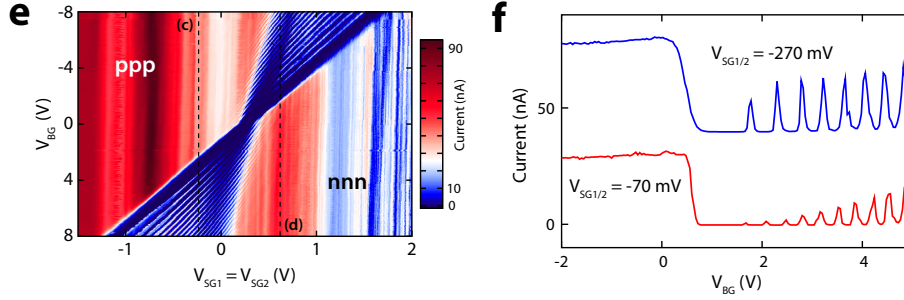


**Figure 7.3:** (cont. of figure 7.2) (e), A 2D plot showing backgate sweeps at different splitgate voltages and  $V_{SD} = 10$  mV. The two splitgates are set to the same voltage. The stability diagrams in 7.2(c) and (d) are taken at  $V_{SG1/2}$  values indicated by the dashed lines. (Resonances from residual disorder in the long NT leads can be seen as oscillations as a function of  $V_{SG1/2}$  in the *ppp* and *nnn* configurations.) (f) Using the splitgates, we can tune the width of the *pn* junction depletion region, and hence the tunnel barriers: at  $V_{SG1} = V_{SG2} = -70$  mV, the potential from the splitgates is shallow, giving a wide depletion region and a current of 0.5 nA for the first electron Coulomb peak at  $V_{SD} = 10$  mV. At  $V_{SG1} = V_{SG2} = -270$  mV, the potential across the *pn* junction is steeper, now giving a narrower depletion region and a current of 13 nA for the first electron. (The  $V_{SG1/2} = -270$  mV trace has been offset in  $V_{BG}$  and in current.)

attractive for holes but repulsive for electrons. We consequently observe single dot behavior for the first hole and weakly coupled double dot behavior for the first electron. In figure 7.4b, we apply a positive backgate voltage,  $V_{BG} = 250$  mV. The potential in the middle of the nanotube is now repulsive for holes: the first hole enters a weakly coupled double dot, while electrons fill a mostly single dot potential. (At some gate voltages, the presence of the oxide creates a non uniform potential which results in strongly coupled double dot instead of purely single dot behavior. See section S1 of the Supplementary Information for further discussion.) By changing  $V_{BG}$ , we can continuously tune the interdot coupling in the few-electron and few-hole regime from weakly coupled double dot to single dot behavior.

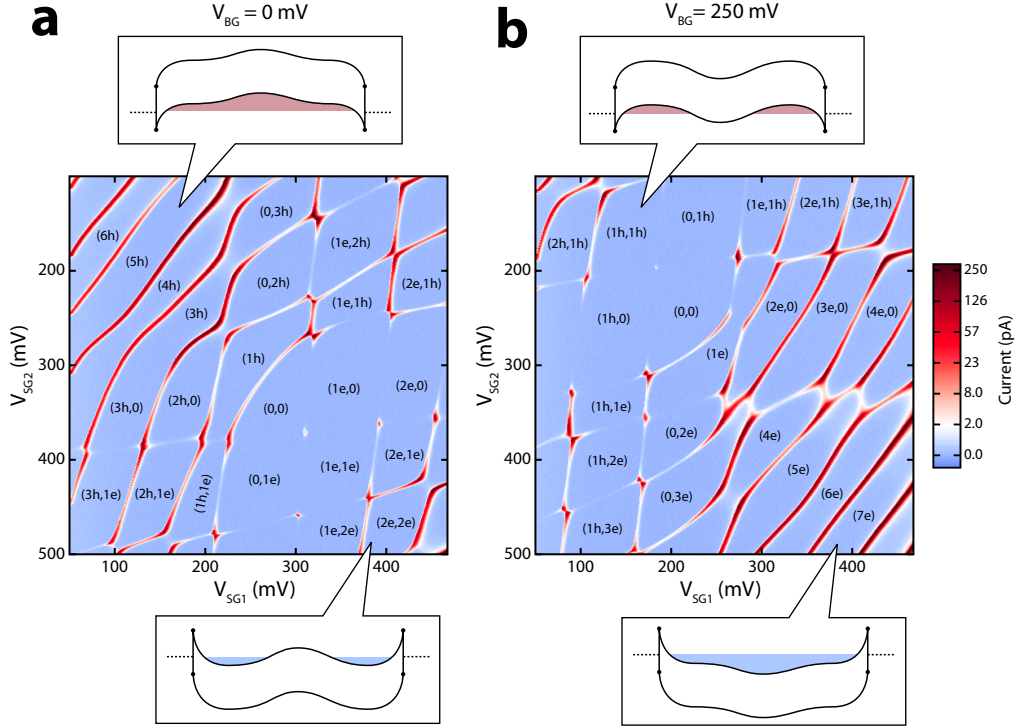


**Figure 7.4: A tunable double quantum dot in the few-electron and few-hole regime.** Current as a function of the two splitgate voltages at  $V_{SD} = 0.5$  mV for device D2. In device D2, electrons are confined in the nanotube by Schottky barriers at the metal contacts, with a potential that is tunable using the three gates. Electron and hole occupation numbers are determined from the transition to a  $pn$  double quantum dot, as described in the Supplementary Information. **(a)**  $V_{BG} = 0$ . At this voltage, a barrier for electrons is induced in the middle of the device. Electrons are added to a weakly coupled double dot potential, while holes are added to a single dot potential. **(b)**,  $V_{BG} = 250$  mV. A more positive  $V_{BG}$  creates a double dot potential for holes and a single dot potential for electrons. The interdot coupling for both the electron and the hole double dot can be tuned continuously using the backgate voltage.

## 7.4 Klein tunneling

In figure 7.5, we investigate the tunable interdot coupling in our double quantum dot more detail by studying current at the  $(0,1e) \leftrightarrow (1e,0)$  triple point transition of a weakly coupled double quantum dot. In a weakly coupled double quantum dot, current can only flow at specific values of the gate voltages, known as triple points, where the levels in the two dots are aligned, allowing an electron to tunnel from one dot to the other [96]. In figures 7.5a to c,  $V_{BG}$  is made more negative, creating a larger barrier for electron tunnelling between the dots, suppressing the

current at the triple point. However, as we sweep  $V_{\text{BG}}$  further, shown in figures 7.5d and e, the current increases again, despite creating an even larger barrier for electron tunnelling.

The explanation of this curious increase of the current is a novel tunnelling process analogous to the tunnelling paradox in high energy physics proposed by Klein [93, 94, 95]. Specifically, we will define Klein tunnelling as any enhancement of the tunnelling of an electron through a barrier due the so-called negative energy solutions (positron states) that arise in relativistic quantum mechanics (see Supplementary Information for further discussion). In figure 7.5, the enhancement of the interdot coupling we observe at large tunnel barrier heights is an example of Klein tunnelling in a carbon nanotube, where now the valance band of the nanotube plays the role of the negative energy solutions in relativistic quantum mechanics. What is unique about the data in figure 7.5 is that we have created a direct implementation of Klein’s *gedanken* experiment in our double quantum dot device, where we are able to tune continuously from the normal tunnelling regime to the Klein tunnelling regime simply by changing the barrier height with a gate voltage. We have also observed Klein tunnelling for holes (see Supplementary Information). In figure 7.5, what we observe is a kind of “virtual” Klein tunnelling, where the electron virtually occupies a state in the empty valance band in order to tunnel from the left to the right dot, similar to a cotunnelling process [97]. In addition to our observations in a double quantum dot, the *npn* data in figure 7.2 can be thought of as a type of Klein tunnelling in a different regime, where the valance band is now occupied with holes, and where Klein tunnelling occurs by the electron sequentially tunneling across the two *pn*-junctions. This also emphasizes the close relation between Klein tunnelling in high energy physics and interband tunnelling phenomena in semiconductor physics, such as Zener tunnelling in insulators [98] and direct interband tunnelling in an Esaki diode [99].

Analyzing the current at the  $(0,1e) \leftrightarrow (1e,0)$  transition quantitatively using the result from Stoof and Nazarov [100, 101], we calculate the tunnel rates  $\Gamma_L$  and  $\Gamma_R$  of the barriers to the leads, and the interdot tunnel coupling  $t_c$ , shown in figure 7.5h. At these gate voltages, we are in the limit of weak interdot coupling:  $t_c \sim 5 \mu\text{V} \ll \Gamma_L, \Gamma_R \sim 0.6 \text{ mV}$ . The interdot coupling,  $t_c$ , is decreased from an initial value of  $9 \mu\text{V}$  to a minimum of  $3 \mu\text{V}$  as a function of backgate, before the onset of Klein tunnelling results in an increase up to  $9 \mu\text{V}$  as we approach gate voltages where an *npn* triple dot is formed.  $\Gamma_L$  and  $\Gamma_R$  are found to be independent of the backgate voltage, indicating that the backgate is not influencing the Schottky barrier transparency.

Finally, note that although we are in the appropriate double quantum dot

coupling regime, we have not found evidence of spin blockade at any of the expected transitions [39]. (A parallel magnetic field of 1.5T was applied to ensure that the nanotube valley degeneracy was lifted). One possible explanation for this is a singlet-triplet splitting in the (0,2e) state that is much smaller than the 3 mV single particle spacing we observe in the single electron quantum dot. This could be an indication of Wigner crystal [52], in which the electron wavefunction overlap is very small, and consequently the single-triplet splitting is strongly suppressed. This possibility will be investigated further using devices with more gates, which could allow us to probe the Wigner crystallization transition by tuning the quantum dot confinement potential.

We have presented a new technique for confining single electrons and single holes in ultra-clean carbon nanotubes. By eliminating disorder and incorporating local gates, a new level control over single electron confinement has been achieved, allowing us to observe a novel type of tunnelling in a single electron carbon nanotube device. Although our motivation for such a device comes from the spin physics of carbon nanotubes [54], the fabrication itself could have a much broader use in carbon nanotube applications, such as electrically doped *pn* junctions for carbon nanotube optical emission [102], where low disorder and multiple gates for electrical control of p-n junctions could allow the development of new types of optically active devices.

## Methods

Fabrication begins with a p++ Si wafer with 285 nm of thermal silicon oxide. On top of this, a 50 nm thick n++ polysilicon gate layer is deposited, followed by a 200 nm LPCVD-TEOS oxide layer. Using electron-beam lithography and dry etching, a trench of approximately 300 nm deep is etched, forming the two splitgates from the n++ Si gate layer. A 5/25 nm W/Pt layer is deposited to serve as source and drain contacts, and nanotubes are then grown from patterned Mo/Fe catalyst [61].

In about half of the devices, a single carbon nanotube is suspended across the trench making electrical contact to the source and drain. Transport through the devices is characterized at room temperature, and selected devices are cooled to <300 mK for low temperature transport measurements. In total, we have measured 11 devices at low temperatures, of which 4 reached the single electron regime. Here we present data from two small bandgap devices: D1 with  $L = 1.5 \mu\text{m}$ ,  $W = 300 \text{ nm}$  and bandgap  $E_g = 60 \text{ mV}$ , and D2 with  $L = 300 \text{ nm}$ ,  $W = 500 \text{ nm}$  and  $E_g = 25 \text{ mV}$ , where bandgaps are determined by subtracting the charging energy from the size of the empty dot Coulomb diamond.

**Acknowledgments** It is a pleasure to acknowledge P. L. McEuen for the suggestion of using  $pn$  junctions as tunable barriers, as well as D. Loss, T. Balder, I. T. Vink, R. N. Schouten, L. M. K. Vandersypen, and M. H. M. van Weert for useful discussions and suggestions. Supported by the Dutch Organization for Fundamental Research on Matter (FOM), the Netherlands Organization for Scientific Research (NWO), and the Japan Science and Technology Agency International Cooperative Research Project (JST-ICORP).

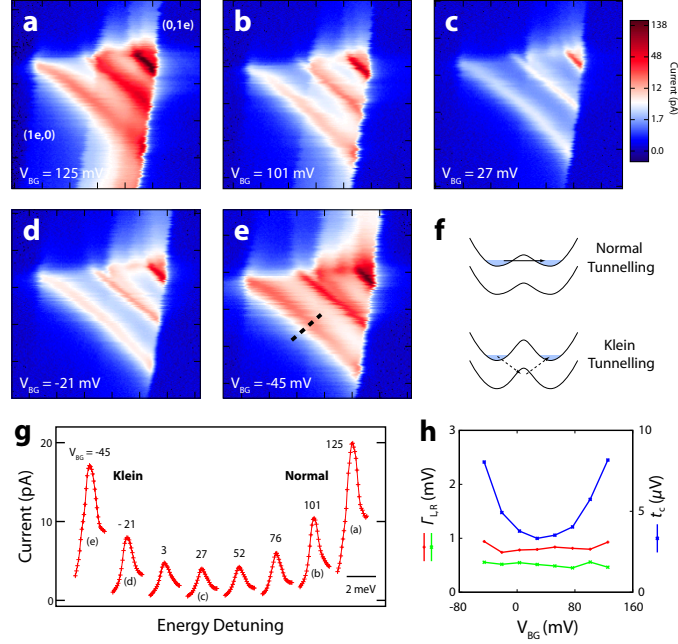


**Figure 7.5: Klein tunnelling in a single electron double quantum dot.** Current at the  $(1e,0) \leftrightarrow (0,1e)$  triple point for a single electron double quantum dot at  $V_{SD} = 5$  mV. (Note that the interdot capacitance  $E_c^{\text{inter}} \sim 0.2$  mV is much smaller than the bias, and thus the triple point bias triangles for the electron and hole cycle[96] strongly overlap.) Transitions to the excited state of the outgoing dot are visible as lines in the triangle running parallel to the baseline give a quantized level spacing of 3 mV, consistent with a dot length of  $\sim 500$  nm. In (a) through (c), the backgate is made more negative, creating a larger barrier for electron tunnelling. As a result, the current through the double dot is decreased. In (d) and (e), however, the current begins to increase again despite a larger barrier for electron tunnelling. (f), This increase in current results from tunnelling of an electron below the barrier through a virtual state in the valence band, analogous to Klein tunnelling in high energy physics. (g) Line cuts of the triple point data in (a)-(e) showing the current for the ground state baseline transition at different backgate voltages. The line cuts are taken along the dashed line in (e). The x-axis shows the distance along this line converted into the energy detuning between the left and right dot ground state levels. For the rightmost traces, interdot tunnel coupling is mediated by normal electron tunnelling, while for the leftmost traces, Klein processes provide the interdot tunnel coupling. (h) Parameters from a fit to the Stouf-Nazarov equation. The interdot tunnel coupling initially decreases as the barrier height increases ( $V_{BG} = 125$  to 27 mV), and then increases due to the onset of Klein tunnelling as the barrier height becomes comparable to the bandgap ( $V_{BG} = 27$  to -45 mV).

## 7.5 Supplementary information

### S1 Determining electron numbers

Absolute electron numbers in the device are identified by the transition from a  $nn$  or a  $pp$  single dot to a  $pn$  or  $np$  double dot, as shown in figure 7.6. For example, at  $V_{SG1} = -250$  mV and  $V_{SG2} \sim 260$  mV, we remove the last hole from the right side of the nanotube,  $(p,p) \rightarrow (p,0)$ . As we sweep  $V_{SG2}$  further, at  $V_{SG2} \sim 380$  mV, we fill an electron into the right dot. Here we see an abrupt transition from single dot behavior to double dot behavior, signaling the transition to a  $(p,n)$  double dot. This transition allows us to clearly identify the electron numbers in the device. The electron number assignment was also confirmed by large bias Coulomb diamond measurements such as those shown in figure 7.2 of the main text.

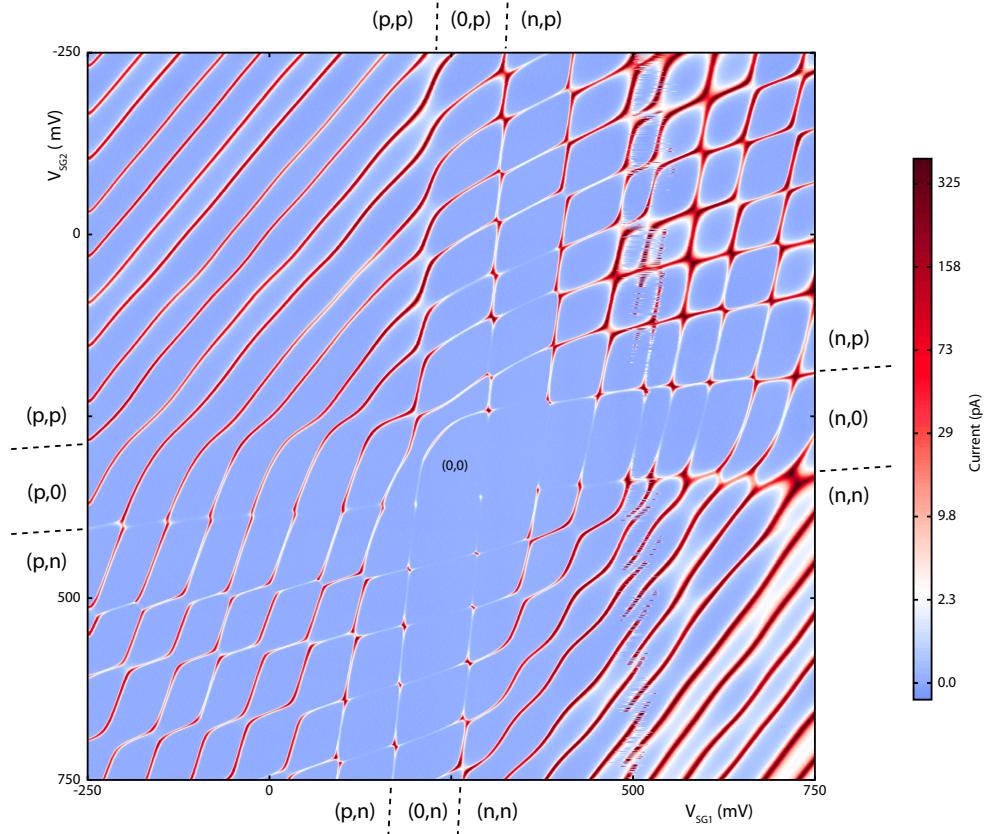


**Figure 7.6:** A 2D splitgate sweep over a larger range used to determine electron numbers from the transition to a  $pn$  double quantum dot. Data is taken at  $V_{BG} = 50$  mV and  $V_{SD} = 0.5$  mV.



At  $V_{SG1} \sim 500$  mV, the device suffers from a “switch” in gate voltage: this switch, which appeared on the third cooldown of the device, is likely due to a charge trap in the oxide. Aside from this, the device is extremely stable. It is also very robust with respect to thermal cycling: after 2 thermal cycles including exposure to air, the barrier transparencies were unchanged and the position of the first Coulomb peak moved by less than 50 mV in gate space.

Note also that although the backgate voltage used in figure 7.6 should result in single dot behavior for holes, the data show some bending of the Coulomb peak trajectories along the (p,p) to (0,p) and (p,0) transitions, indicating a strongly tunnel coupled double dot type of behavior. It is also visible along the (n,n) to (n,0) and (0,n) transitions in figure 7.4(b) of the main text, and at higher electron numbers in figure 7.6. This results from a somewhat non uniform potential induced by the presence of the oxide under part of the tube, likely due to a combination of trapped charges in the oxide and the abrupt change in dielectric constant.

## S2 Stoof-Nazarov Equation

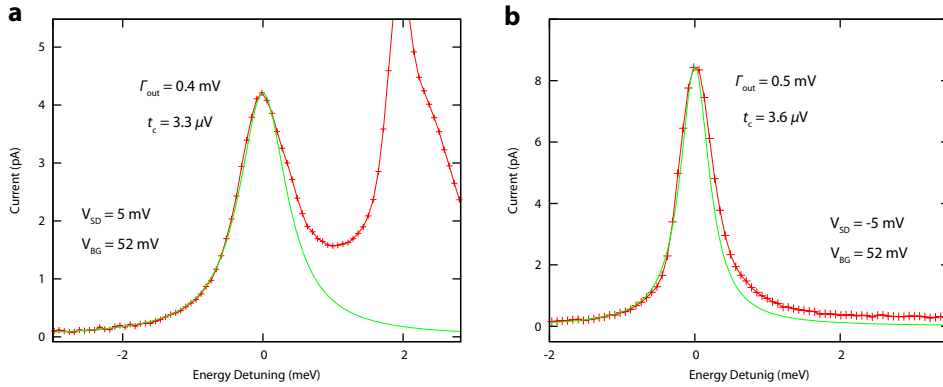


**Figure 7.7:** Fit of  $(0,1e) \leftrightarrow (1e,0)$  transition at  $V_{BG} = 52$  mV to the Stoof-Nazarov theoretical result for **a**, positive and **b**, negative bias. A detuning independent inelastic contribution to the current of 350 fA is clearly visible in the reverse bias trace. This inelastic current is also present in **a**, but is more difficult to identify due to a nearby excited state of the outgoing dot in forward bias.

To analyze the data quantitatively, we fit the current at the ground state to ground state transition along the baseline of the triple point bias triangle as a function of energy detuning  $\epsilon$  to the expression from Stoof and Nazarov [100, 103]. By performing such an analysis, we are able to isolate the contribution of the middle tunnel barrier from the measurement of the current through the double

quantum dot. For an interdot tunnel coupling  $t_c$  and tunnel rates  $\Gamma_{L,R}$  to the left and right leads, the elastic current in a double quantum dot is given by:

$$I_{el}(\epsilon) = \frac{et_c^2\Gamma_R}{t_c^2(2 + \Gamma_R/\Gamma_L) + \Gamma_R^2/4 + (\epsilon/h)^2} \quad (7.1)$$

In the limit of weak interdot tunnel coupling,  $t_c \ll \Gamma_L, \Gamma_R$ , this reduces to a simple Lorentzian line shape of the form:

$$I_{el}(\epsilon) = \frac{4et_c^2/\Gamma_R}{1 + (2\epsilon/\Gamma_R h)^2} \quad (7.2)$$

A fit of the data to equation 7.2 for a single electron double dot is shown in figure 7.7. The fit was performed for  $\epsilon < 0$  to isolate the purely elastic contribution to the current. For  $\epsilon > 0$ , the fit deviates from the Lorentzian lineshape due to inelastic processes [104].

### S3 Relativistic tunnelling through a barrier and the Klein Paradox

Consider an electron of energy  $E$  and momentum  $\hbar k$  incident on a square barrier of height  $V$  as shown in figure 7.8. We are interested in the probability that the electron is transmitted to  $x > L$  using the Dirac equation. The solutions of the Dirac equation have two branches [105]: a set of positive energy solutions with  $E > 0$  and a set of negative energy solutions with  $E < 0$ . The two branches are separated by an energy gap  $2mc^2$ . The vacuum state is interpreted as having the negative energy solutions filled with electrons (the ‘‘Dirac sea’’), and a hole in the Dirac sea is then interpreted as a positron. For a barrier height that is small compared to  $2mc^2$ , shown in figure 7.8a, the Dirac equation gives a wavefunction that decays exponentially inside the barrier: for an incident energy  $E \ll V$ , the probability of the electron tunnelling to the region  $x > L$  is small. This is also what is predicted by the non-relativistic Schrodinger equation.

However, if the barrier height becomes very large, so that  $V$  is comparable to  $2mc^2$ , the negative energy solutions of the Dirac equation strongly modify the tunnelling process. In particular, Klein noticed that for  $V \sim 2mc^2$ , as shown in figure 7.8(b) and 7.8(c), an electron moving at non-relativistic speeds incident on the barrier at position  $x = 0$  can tunnel to  $x > L$  on the other side of the barrier with nearly unity probability. In the context of the non-relativistic Schrodinger equation, such a high tunnelling probability would be completely unexpected, hence the idea of such tunnelling as a paradox.

The tunnelling enhancement can be divided into two regimes, illustrated in figures 7.8b and 7.8c. We will refer to the first, illustrated in figure 7.8b, as the

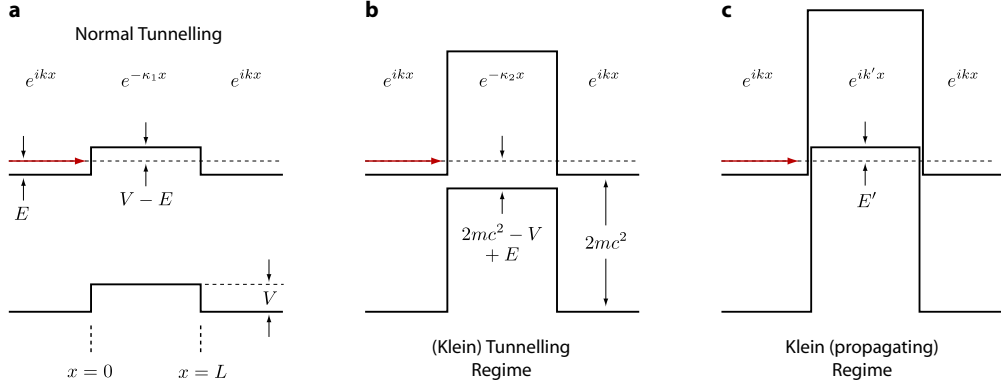


**Figure 7.8:** Relativistic tunnelling through a barrier. Positive energy solutions of the Dirac equation are separated from the negative energy solutions by an energy gap  $2mc^2$ . We consider the probability that an electron incident on a barrier of height  $V$  at  $x = 0$  with energy  $E$  is transmitted to the region  $x > L$ . **(a)** For  $V \ll 2mc^2$ , the wavefunction inside the barrier decays exponentially with a decay length  $\kappa_1 = \sqrt{2m(V - E)/\hbar}$ , as predicted by the non-relativistic Schrodinger equation. We refer to this as the “Normal” tunnelling regime. **(b)** For  $V$  slightly less than  $2mc^2$ , the wavefunction also decays exponentially inside the barrier. However, due to the nearby negative energy solutions of the Dirac equation, the decay length is now much longer, given by  $\kappa_2 = \sqrt{2m(2mc^2 - V + E)/\hbar}$ , and the transmission probability is much higher than that predicted by the Schrodinger equation. We refer to this as the (Klein) Tunnelling regime. **(c)** For  $V > 2mc^2$ , the electron now propagates inside the barrier without decaying by occupying a negative energy solution of the Dirac equation. Inside the barrier, the wavefunction is a plane wave  $e^{ik'x}$  with energy  $E' = V - 2mc^2 - E$ . We refer to this as the Klein (propagating) regime.

(Klein) Tunnelling regime [106]. Here, the electron propagates inside the barrier as an evanescent wave, but the transmission probability can be very high since the decay length is significantly longer than that from the Schrodinger equation due to the negative energy solutions. We will refer to the second regime, shown in figure 7.8c, as the (propagating) Klein regime. Here, the wavefunction in the barrier is oscillatory in nature and does not decay. Both cases are examples of what we will call non-classical “Klein Tunnelling” in which the electron emerges at  $x > L$  with a much higher probability than that predicted by the Schrodinger equation.

The electronic spectrum of a carbon nanotube at low energies is also given by a Dirac equation that is the same as that for normal electrons [23, 95], but with  $2mc^2$  replaced by the bandgap  $Eg$ , and the speed of light  $c$  replaced by the Fermi velocity of graphene  $v_F$  ( $\sim 0.9 \times 10^6$  m/s). Free electrons in the Dirac equation

correspond to electrons in the conduction band of the nanotube, and positrons in the Dirac equation correspond to holes in the valance band. Thus, it should be possible to observe phenomena analogous to the two Klein tunnelling regimes of 7.8 b and c in a carbon nanotube device.

In figure 7.2 of the main text, we present data demonstrating a single hole  $npn$  and single electron  $pnp$  quantum dot. The current that we observe at the Coulomb peaks can be considered as an example of the (propagating) Klein regime illustrated in figure 7.8c, where the potential barrier from our gate voltages is larger than the bandgap. Figure 7.2d from the  $pnp$  configuration corresponds to the (propagating) Klein regime for positrons, and figure 7.2c from the  $npn$  configuration corresponds to the same regime for electrons.

In figure 7.5 of the main text, we show an example of the (Klein) tunnelling regime of figure 7.8b. In the data, we observe a continuous transition from the normal tunnelling regime to that where the negative energy solutions of the Dirac equation provide an enhancement of electron tunnelling, as in the original Klein *gedanken* experiment. We also note that the unusual tunnelling process shown in figure 7.8b, where the decay length in the barrier is increased due to the negative energy states, has recently been proposed as a mechanism of generating exchange coupling between two distant quantum dots in graphene nanoribbons [95]. Our experiment demonstrates explicitly such tunnelling in a carbon nanotube.

### S4 Klein tunnelling for a single hole double quantum dot

In figure 7.5b, we show Klein tunnelling for a single hole double quantum dot. Qualitatively, the process is the same as that for the single electron double dot. In the single hole double dot, the tunnel rates to the leads are smaller by a factor of 2-3 compared to the single electron double dot: in the device, the Fermi level pinning at the metal contacts is such that electrons see a smaller Schottky barrier. This can also be seen in figure 7.7, where the electron single dot peaks show more current and broadening than those of the hole single dot.

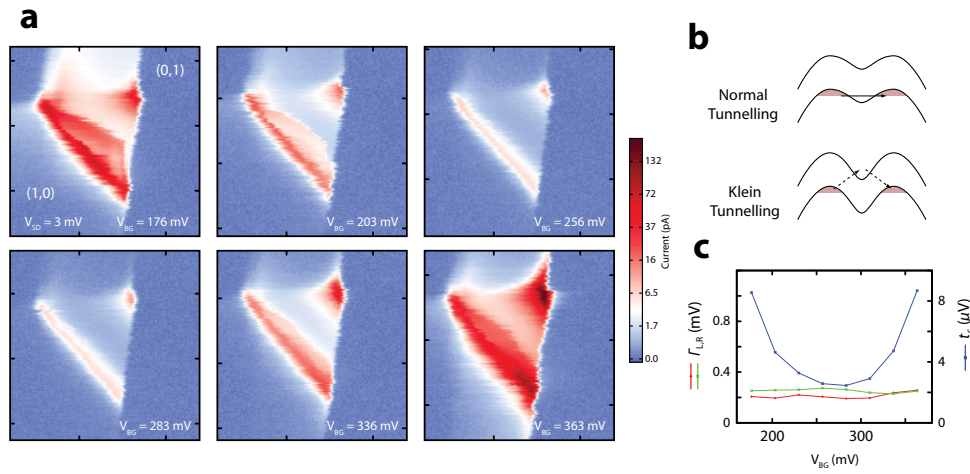


**Figure 7.9:** (a),(b) Klein tunnelling at the  $(0,1h) \leftrightarrow (1h,0)$  single hole double dot transition and (c), parameters from a fit to the Stoof-Nazarov expression.



# Chapter 8

## Towards local gate control over clean, as-grown carbon nanotubes

In this chapter, we present measurements on the samples described in chapter 3.5. Clean, suspended CNTs are combined with narrow, local gates to achieve tunability over all crucial QD parameters. Also, these gates allow application of high frequency pulses. We demonstrate the functionality of a five-gate device by realizing a tunable few-electron triple QD. At the end of this chapter, we discuss the possibilities of these devices for spin based quantum information processing.

## 8.1 A tunable triple quantum dot

As described in the previous chapter, the tunability of an electrostatic barrier, separating two sections of a CNT, is limited by tunneling through states in the valence band (Klein tunneling). Here we explore this regime further by observing the effect of discrete energy levels in the valence band. These discrete energy levels are a manifestation of Coulomb blockade and level quantization in the CNT section where the barrier is created.

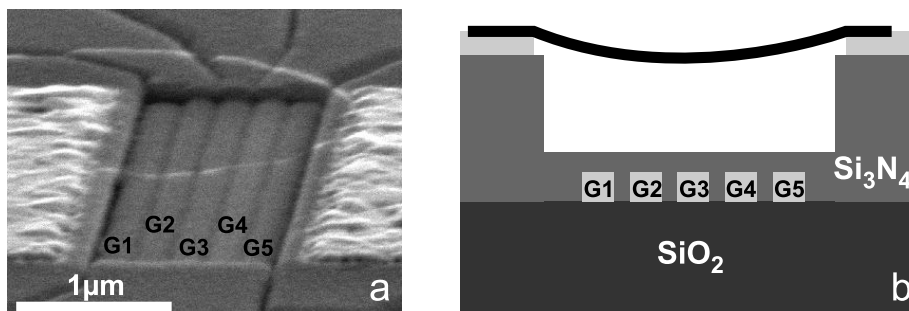


**Figure 8.1: Device:** (a) SEM image of a device similar to the measured one. (b) Schematic of the device: A CNT is grown over two W / Pt ohmic contacts, with a trench in between. At the bottom of the trench, there are five local gates, G1 - G5, with a width of  $\sim 120$  nm and a spacing of  $\sim 140$  nm.

The sample (figure 8.1) consists of a small-bandgap CNT crossing a trench between two W/Pt contacts. Underneath the CNT, there are five  $\sim 120$  nm wide gates, which allow us to locally adjust the electrical potential along the CNT. The ohmic contacts are isolated from the gate layer by 250nm of  $\text{Si}_3\text{N}_4$ . The horizontal distance between the two metal contacts is  $1.4\mu\text{m}$ .

In the sample that we present data from, there is a second CNT connecting the two metal contacts, running around the gate area (similar to the device shown in figure 8.1a). We conclude this from a nonzero background current, when the investigated CNT is in Coulomb blockade. This background current strongly depends on  $V_{G1}$  and  $V_{G5}$ , the voltages on G1 and G5, but hardly on  $V_{G2}$ ,  $V_{G3}$  and  $V_{G4}$ . Since G2, G3 and G4 run from the upper side into the trench but G1 and G5 from the lower side, we conclude that this second CNT is running around the gate area on the lower side of the trench. In our measurements, we use G1 and G5 to tune the barriers at the contacts, meaning that they are usually set to a constant voltage during a measurement. Therefore, the current through the second CNT does not obstruct most of the measurements presented here (mainly stability diagrams). To make this background current even less visible, we typically do



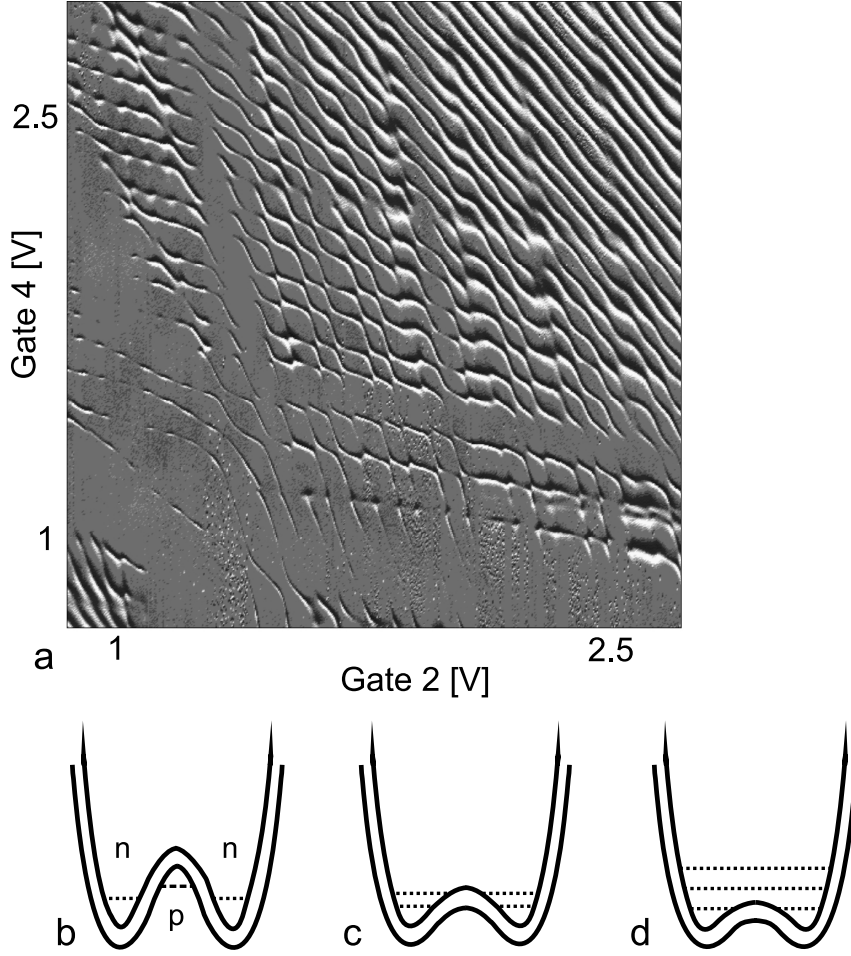


**Figure 8.2: Transition from a triple to a single QD** (a)  $dI / dV_{G4}$  as a function of the voltages on G2 and G4. The voltages on the other gates are:  $V_{G1} = V_{G5} = -1.5$  V and  $V_{G3} = -0.15$  V. For  $V_{G2}, V_{G4} < 1$  V, the entire CNT-section above G2-G4 is p-type. For  $V_{G2}, V_{G4} > 1.2$  V, there are three different regimes visible. Close to the depletion region, electrons are added to a n-p-n triple QD potential (as sketched in (b)). When making G2 and G4 more positive, the middle section is depleted from holes, because of the cross-coupling from G2 and G4 to the middle section of the CNT. This is sketched in (c). Now electrons are added to a n-n double QD. Finally, when making G2 and G4 even more positive, cross-coupling further lowers the barrier in the middle; electrons feel a single QD potential (d). Hence the diagonal lines at the upper right of the stability diagram.

not plot the current or conductivity but instead show the differential conductance  $dI/dV_{Gate}$ . Measurements were performed at  $T = 2$  K.

We apply negative voltages to G1 and G5 to make the left and right segment of

the CNT (next to the contacts) p-type. Figure 8.2 shows a large stability diagram. Depending on the voltage applied to G2 and G4, we observe different regimes: In particular, for  $V_{G2}, V_{G4} > 1.2$  V, we observe the transition from a triple QD via a double QD to a single QD. The reason for this transition is the finite cross-coupling from G2 and G4 to the middle section of the CNT. For voltages  $< 1$  V on these gates, the whole CNT-section above G2 - G4 is p-type. Raising the voltage on G2 and G4 adds electrons to the left and right CNT segments while the middle segment first stays p-type (triple QD), then is gradually depleted (now there is a double QD potential) and finally also becomes n-type (resulting in a single QD potential). The potential landscapes corresponding to these regimes are shown in figure 8.2 b-d. In the following section, we discuss the triple QD behavior in detail.

Triple QDs have been investigated in GaAs systems [107, 108, 109] and in the many electron regime also in CNTs [110]. Besides scaling they are also interesting from a quantum information point of view [109, 111, 112] Here we demonstrate a tunable few-electron triple QD in the n-p-n configuration. The charge carriers are electrons in the left and right QD, but holes in the middle QD. Since in this configuration, the type of charge carriers is alternating in adjacent sections of the CNT, all barriers are created by p-n junctions.

### 8.1.1 Stability diagrams

We discuss the stability diagrams (figure 8.3), obtained by plotting the conductance through the device as a function of  $V_{G2}$  and  $V_{G4}$ . G3, which mainly couples to the middle dot, is kept at a constant voltage for each of these plots. We denote charge states by a set of three numbers  $(k,l,m)$ , corresponding to the left, middle and right QD. Positive numbers mean electrons, negative numbers holes. The tunnel barriers are rather small, due to the small value of the CNT bandgap. Therefore, most cotunneling lines between the different charge states of the triple QD are clearly visible.

We start by observing that there are different slopes, corresponding to changing the number of charge carriers in each of the three QDs. Diagonal lines indicate charge transitions which couple equally to G2 and G4 and are therefore identified as charge transitions of the middle QD. Charging lines that couple mainly to G2 correspond to transitions of the left QD, lines that couple mainly to G4 correspond to transitions of the right QD. We start by assigning the first diagonal line (from the upper right) to emptying the middle section from the last hole  $(k,-1,m) \rightarrow (k,0,m)$ . Also, the area where the left and right sections of the CNT are emptied of charge carriers can be clearly identified. Now, we can assign a

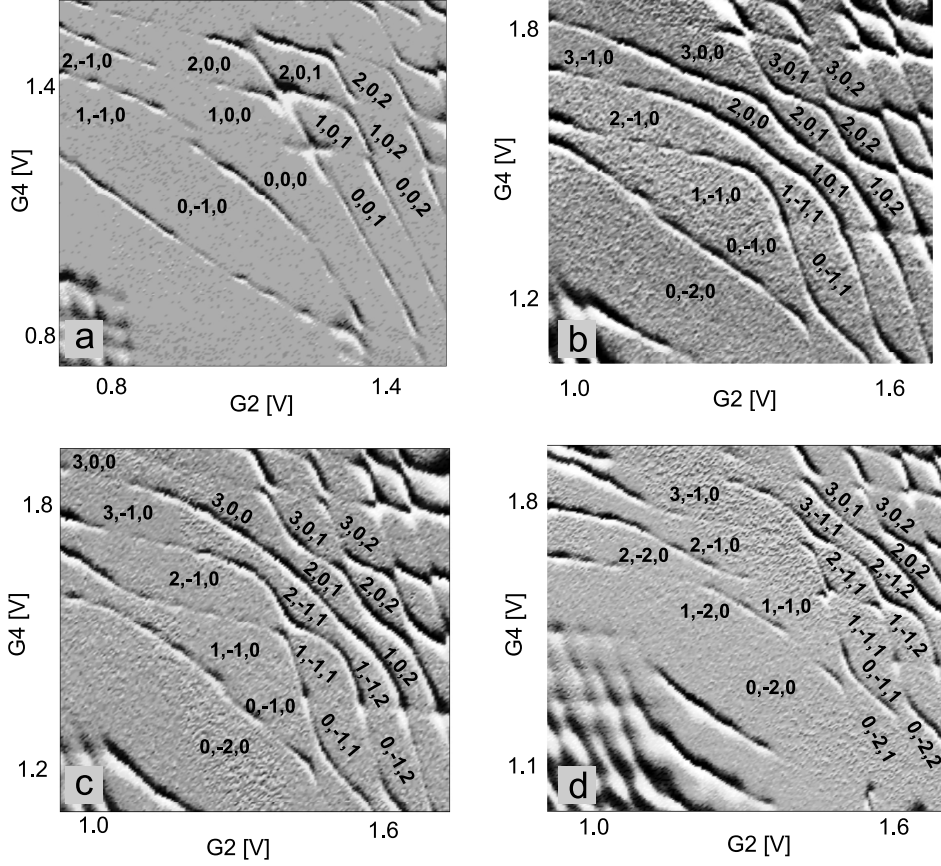


**Figure 8.3: Stability diagrams of the n-p-n triple QD** We plot  $dI/dV_{G4}$  as a function of  $V_{G2}$  and  $V_{G4}$ . We show stability diagrams for different  $V_{G3}$ , demonstrating the tunability of our triple QD. A bias voltage of 2 mV is applied across the CNT.  $V_{G1} = V_{G5} = -1.5V$  for all plots. (a)  $V_{G3} = 0V$ . The middle dot is depleted of holes before electrons are added to a few-electron double QD. (b)  $V_{G3} = -0.2V$ . Now the middle QD is not emptied when the first electrons are added to the left and right QDs (e.g., we now find the state  $(1, -1, 1)$  in the stability diagram). (c)  $V_{G3} = -0.25V$ . (d)  $V_{G3} = -0.3V$ .

charge state to each region of the stability diagram. The large anticrossings at the top left regions of the stability diagrams indicate that the inter-dot coupling between the middle and left QD is very large. Comparing stability diagrams with different  $V_{G3}$  shows that a given charge transition of the middle QD (e.g. the  $(k, -1, m)$  to  $(k, 0, m)$  transition) moves to higher electron numbers of the left and right QDs as  $V_{G3}$  is decreased.

## 8.2 Towards spin-manipulation

CNTs are a promising material for spin-based quantum information processing: Spin-orbit coupling allows all-electrical spin manipulation and, if CNTs made from purified  $^{12}\text{C}$ , nuclear spins are absent. In this section, we present future plans to use the clean, as-grown samples presented above for spin manipulation. In particular, we discuss the difficulties connected with electron-electron interactions and electro-mechanical coupling.

### Bandgap

For many of the following experiments, it is necessary to tune the tunneling rates into and between the QDs over a wide range. In particular, it is desirable to reduce the tunneling rates to values of  $\Gamma \leq 5\text{MHz}$ , corresponding to a current of  $I \leq 1\text{pA}$ . This requires a minimal bandgap  $E_G$  for the used CNTs. E.g. when using a square barrier as a first simple approximation, one requires  $E_G > 250\text{meV}$  for a barrier width of  $100\text{nm}$ <sup>1</sup>. Instead of using CNTs with such a large bandgap, one can also make the barriers wider. However, this requires a careful device design since one wants to keep the QDs itself small, as discussed in the following.

### 8.2.1 Electron-electron interactions

Pauli blockade [39] is the most important and powerful mechanism to probe spin states in QDs [48]. In section 2.3.2, we explained how electron-electron (e-e) interactions in CNTs can significantly reduce the singlet-triplet splitting and thereby prevent Pauli blockade. To change this, one either has to reduce the QD size or screen the e-e interactions.

With the current devices, it seems difficult to reduce the QD size to  $\leq 20\text{nm}$  and get a large enough singlet-triplet splitting for a 2-electron QD in a suspended CNT. Nevertheless, a significant reduce in the QD size seems still within reach (compare e.g. [62, 46]) by optimizing the fabrication recipe. The effect of e-e interactions on shell filling in a QD is reduced for larger carrier densities, as shown in [52] and [51]. This means it should be possible to observe Pauli blockade in a large, suspended CNT-QD for higher electron numbers. Pauli blockade has indeed been demonstrated for higher electron numbers in various systems [45, 54, 113].

Another possibility is to screen e-e interactions by a dielectric. Our fabrication scheme easily allows to grow CNTs at the surface of such a dielectric (instead

---

<sup>1</sup>We have calculated the transmission for a barrier height of  $E_G/2$ . For higher barriers, the transmission increases again due to Klein tunneling.

of growing them across a trench). The experiment in chapter 7 shows that it is possible to reach the few-electron regime in as-grown CNTs, even when a significant part of the CNT is not suspended but in contact with a dielectric substrate. Experiments with  $\sim 200$  nm long CNT-QDs on a  $\text{SiO}_2$  substrate have shown shell-filling behavior in the few-electron regime [21]. Since one can use dielectrics with much higher  $\epsilon$  than  $\text{SiO}_2$  ( $\epsilon = 3.9$ ), e.g.  $\text{Al}_2\text{O}_3$  with  $\epsilon = 9.3$ , it should be possible to use even larger CNT-QDs. Also, completely embedding the device in a thin layer of dielectric [114] (as the very last fabrication step) is possible with our devices.

### 8.2.2 Electro-mechanical coupling

Suspended CNT-QDs show a large coupling between their mechanical motion (namely, the bending mode phonons) and the electrical current [115, 116, 117]. This can easily obstruct detection of small signals such as Pauli blockade. This effect will however be almost absent in CNTs on a substrate, since the bending mode phonons are highly damped then. But also in suspended CNTs, the electro-mechanical coupling can be strongly suppressed. As shown in [117], the backaction from mechanical motion on the electron transport through QDs in the Coulomb blockade regime is suppressed when lowering the tunneling rates through the QD(s). The instabilities disappear when the tunneling rate through the QD,  $\Gamma$ , is lower than the mechanical resonance frequency,  $f_0$ . For a  $1\mu\text{m}$  long CNT with  $f_0 = 80$  MHz, this requires a current  $I < 10\text{pA}$ , which is a typical value for Pauli blockade experiments.

### 8.2.3 Schemes for coherent spin manipulation

Different schemes are possible to perform coherent spin manipulation in CNT double QDs, many of them have been investigated already in GaAs QDs:

Spin rotations can be driven directly by an oscillating magnetic field [37], generated on-chip. This, however, is difficult to integrate in the current device design with as-grown CNTs.

Another possibility is to create a magnetic field gradient and move the confined electron forth and back through this field gradient with an oscillating electric field. This creates an effective oscillating magnetic field, felt by the electron spin, and can thereby induce spin rotations [118]. For a CNT, one would apply a static magnetic field along the CNT-axis (thereby also splitting off one of the two valley-states) and create a gradient in a magnetic field component perpendicular to the CNT axis by putting a micromagnet in close vicinity.

The most promising scheme for spin manipulation uses spin-orbit coupling in CNTs. In presence of spin-orbit coupling, spin rotations of a confined electron can be induced by an oscillating electric field [24]. A detailed scheme making use of spin-orbit coupling and bends in CNTs was proposed in [25]. The scheme uses the fact, that the effective magnetic field (which consists of an applied external field and an effective spin-orbit field) changes along a bent CNT. Rabi frequencies of several MHz up to GHz have been proposed for realistic device geometries and parameters. This approach also allows to link electron spins in different CNTs via capacitive coupling, making two-qubit operations and scaling possible. While bent CNTs seem difficult to achieve controllably in suspended CNTs, this is very well possible for CNTs on a substrate.

As well as a single spin qubit, a two-electron singlet-triplet qubit has been successfully demonstrated in GaAs double QDs [36]. This approach has already been used to determine an inhomogeneous spin dephasing time of  $T_2^* = 3.2ns$  in a  $^{13}C$  - CNT [41]. Since this dephasing time has been explained by hyperfine interactions with the  $^{13}C$  nuclei, investigating purified  $^{12}C$ -CNTs might indeed result in considerably longer spin dephasing times in CNTs.

Many of these experiments can be carried out by measuring the current transport through a double QD. Nevertheless, it is desirable to make use of an external charge detector, namely for investigating slow processes (if the coherence times are very long) and single shot read out. Therefore, one important step will be to integrate a charge detector with the clean, as-grown CNT devices.

# Appendix A

## Pulse scheme to measure $T_1$ , using an averaged charge detector signal

In this appendix, we describe a three level pulse scheme to measure a relaxation rate  $T_1$  in a QD using a charge detector. We are not interested in single shot measurements but in an averaged charge detector signal. The rate equations describing this process are introduced and solved and we explain how to extract  $T_1$  from averaged charge detector measurements.

## A.1 The pulse scheme

We want to measure the relaxation time  $T_1$  from an excited state (ES) to the ground state (GS) of a QD. Long  $T_1$  ( $\gtrsim 100\mu s$ ) cannot be measured in transport but one must use a charge detector. The pulse scheme to measure  $T_1$  has been introduced by Elzerman et al. [91] and used in many different experiments. The difference for us is that we do not want to obtain  $T_1$  from single traces but instead measure an averaged charge detector signal. We find that it is not feasible to measure only the average QD occupation (as a function of the waiting time  $T_{wait}$ ) during the pulse train since the fidelity for extracting  $T_1$  from this measurement is extremely low<sup>1</sup>. But one can make an averaged measurement in the sense that one averages over many pulse cycles. It is assumed that one barrier of the QD is completely closed, such that electron tunneling can only take place through the other barrier.

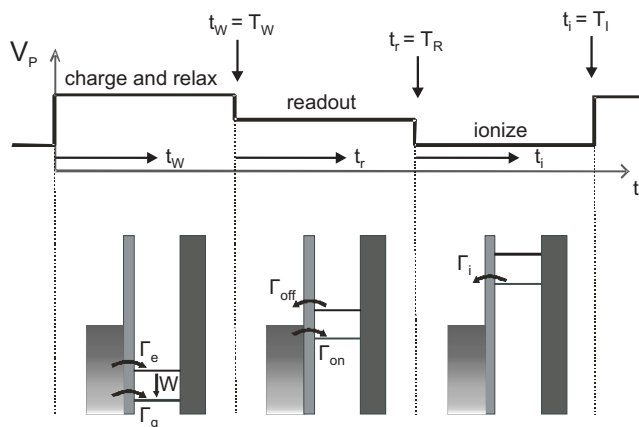


**Figure A.1: 3-level pulse scheme** During the “charge and relax” stage, both GS and ES are below the Fermi level of the leads. An electron can enter either GS or ES. If an electron enters ES it may relax to GS.  $\Gamma_e, \Gamma_g \gg W$  is required for a good fidelity of the scheme. During the “readout” stage an electron in ES may tunnel out of the QD and after some time an electron may enter the QD again into GS. This will be detected by the charge detector. An electron in the GS cannot leave the QD. We assume a splitting between GS and ES, which is larger than  $k_B T$ . During the “ionize” stage, an electron in GS or ES tunnels out, leaving the QD empty. Measuring the fraction of electrons in ES after as a function of  $T_W$  allows to determine  $W = 1/T_1$ . The right barrier to the QD is completely closed such that electron tunneling can only take place through the left barrier.

<sup>1</sup>The reason why this works if one measures the current through a QD is that the current carries one additional information compared an averaged charge detector signal: the direction of electron flow.



## A.2 The rate equations

First, we give an overview over the symbols, used in this section:

Used symbols	
$P_i$	Probability that the dot is ionized
$P_e$	Probability that the dot is filled in the excited state
$W$	Relaxation rate ( $= 1/T_1$ )
$\Gamma_e$	Tunneling rate into the excited state (“charge and relax” stage)
$\Gamma_g$	Tunneling rate into the ground state (“charge and relax” stage)
$\Gamma_t$	$= \Gamma_e + \Gamma_g$ ; total tunneling rate into the QD (“charge and relax” stage)
$\Gamma_{off}$	Tunneling rate out of the excited state during the “readout” stage
$\Gamma_{on}$	Tunneling rate into the ground state during the “readout” stage
$\Gamma_i$	Tunneling rate out of the QD during the “ionize” stage (we assume the same rate for the QD being in GS and ES)
$t_w$	time (during the “charge and relax” stage)
$t_r$	time (during the “readout” stage)
$t_i$	time (during the “ionize” stage)

**Table A.1: Symbols and abbreviations used in this section**

Let us consider a pulse scheme as shown in figure A.1. During the first part (“charge and relax”) of the pulse the rate equations are

$$\dot{P}_i(t_W) = -\Gamma_t P_i \tag{A.1}$$

$$\dot{P}_e(t_W) = \Gamma_e P_i - W P_e \tag{A.2}$$

Solving these equations gives the probabilities that the QD is ionized, in the excited state or in the ground state during  $t_W$ :

$$P_i(t_W) = P_i(0)e^{-\Gamma_t t_W} \tag{A.3}$$

$$P_e(t_W) = P_i(0) \frac{\Gamma_e}{\Gamma_t - W} (e^{-W t_W} - e^{-\Gamma_t t_W}) \tag{A.4}$$

$$P_g(t_W) = 1 - P_i(t_W) - P_e(t_W) \tag{A.5}$$

We have used the simplification that  $P_e(t_W = 0) = 0$ .

Now we set up the rate equations for the second stage of the pulse (“readout”). We will assume that both the rate for tunneling out of GS and tunneling into ES

are zero. This is not necessary the case (e.g. when the splitting between GS and ES is on the order of  $k_B T$  or when taking second order processes into account, these two rates are finite) but for CNTs with  $g = 2$  this assumption can be met already at moderate magnetic fields, if GS and ES are Zeeman-split levels.

$$\dot{P}_i(t_r) = -\Gamma_{On}P_i + \Gamma_{Off}P_e \quad (\text{A.6})$$

$$\dot{P}_e(t_r) = -\Gamma_{Off}P_e - WP_e \quad (\text{A.7})$$

$$\dot{P}_g(t_r) = WP_e + \Gamma_{On}P_i \quad (\text{A.8})$$

Solving these equations gives:

$$P_i(t_r) = Ae^{-(\Gamma_{Off}+W)t_r} + (P_i(T_W) - A)e^{-\Gamma_{On}t_r} \quad (\text{A.9})$$

$$P_e(t_r) = P_e(T_W)e^{-(\Gamma_{Off}+W)t_r} \quad (\text{A.10})$$

$$P_g(t_r) = 1 - P_i(t_r) - P_e(t_r) \quad (\text{A.11})$$

with

$$A = \frac{\Gamma_{Off}}{\Gamma_{On} - \Gamma_{Off} - W} P_e(T_W)$$

The third stage of the pulse (“ionization”) is ment to empty the QD. If we assume that there the same rate  $\Gamma_i$  for tunneling out of ES and GS, the probability that the QD is empty after  $T_I$  is simply given by:

$$P_i(T_I) = 1 - (1 - P_i(T_R))e^{-\Gamma_i T_I} \quad (\text{A.12})$$

By making  $T_I$  sufficiently large, one wants to ensure that the dot is empty at the begin of the new pulse cycle.

### A.3 Finding $W = 1/T_1$

Now that we have solved the rate equations, we show how to find the relaxation rate  $W$ . A typical solution of the rate equations is shown in figure A.2. For CNT-QDs, we find typically that the rates  $\Gamma_e$ ,  $\Gamma_g$  and  $\Gamma_i$  for tunneling into (out of) the QD when the energy levels are far below (above) the Fermi level of the leads are much larger than the rates  $\Gamma_{On}$  and  $\Gamma_{Off}$  when the energy levels are close to the Fermi energy. This allows us to make the “ionization” stage of the pulse considerably shorter than the “readout” stage.

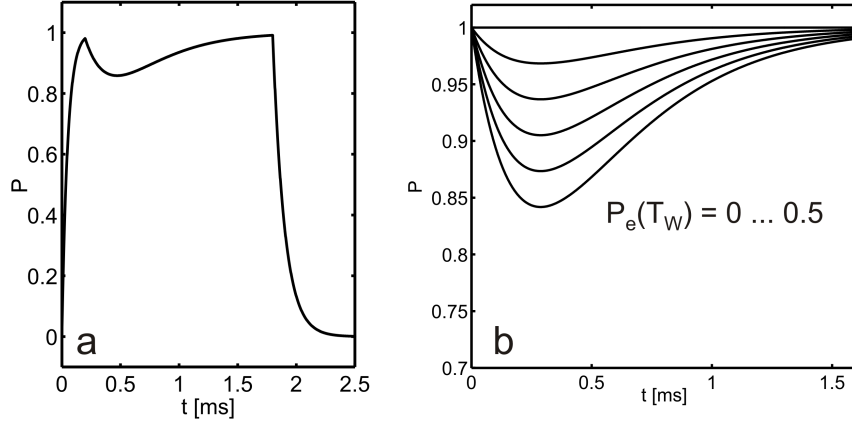


**Figure A.2: QD occupation probability during the pulse** We plot the probability of having an electron in the QD during the different stages of the pulse. **(a)** Occupation probability  $P$  during the three stages of the pulse. We have used the following parameters:  $\Gamma_e = \Gamma_g = \Gamma_i = 10kHz$ ,  $\Gamma_{On} = \Gamma_{Off} = 3kHz$ ,  $W = 1kHz$ . The lengths of the three pulse stages are:  $T_W = 0.2$  ms,  $T_R = 1.6ms$  and  $T_I = 0.7ms$  **(b)** Occupation probability during the readout stage for different probabilities  $P_e$ , of having an electron in ES after the “charge and relax” stage. We have assumed  $P_e(T_W) + P_g(T_W) = 1$  for this plot. The size of the dip allows to determine  $P_e(T_W)$ .

The fraction of electrons that are not relaxed after the “charge and relax” stage shows up in a characteristic dip during the “readout” stage. To optimize the visibility of the dip and the precision of the whole measurement scheme, it is desirable to tune the tunnel rates such that  $\Gamma_{On}, \Gamma_{Off} \gg W$ . Of course,  $\Gamma_{On}$  and  $\Gamma_{Off}$  should be smaller than the measurement bandwidth of the charge detector to resolve the dip. When measuring the charge detector signal, one has to take into account that this signal typically not only reflects the QD occupation but also some direct cross-coupling from the gate where the pulse is applied to. In principle, if all the tunnel rates are known,  $P_e$  can be extracted just from the dip height. However, if there is some uncertainty about  $\Gamma_{On}$  and  $\Gamma_{Off}$ , it is more accurate to make a fit to the dip. Measuring  $P_e$  as a function of  $T_W$  now allows to extract the relaxation time  $T_1 = W^{-1}$  [91].



## Bibliography

- [1] J. J. Ramsden, “What is nanotechnology?,” *Nanotechnology Perceptions*, vol. 1, pp. 3–17, 2005.
- [2] C. Joachim, “To be nano or not to be nano?,” *Nature Materials*, vol. 4, pp. 107–109, 2005.
- [3] L. C. Venema, V. Meunier, P. Lambin, and C. Dekker, “Atomic structure of carbon nanotubes from scanning tunneling microscopy,” *Phys. Rev. B*, vol. 61, no. 4, pp. 2991–2996, 2000.
- [4] S. Ijima, “Helical microtubules of graphitic carbon,” *Nature*, vol. 354, pp. 56–58, 1991.
- [5] S. Ijima and T. Ichihashi, “Single-shell carbon nanotubes of 1-nm diameter,” *Nature*, vol. 363, pp. 603–605, 1993.
- [6] C. Dekker, “Carbon nanotubes as molecular quantum wires,” *Physics Today*, vol. 52 (2), pp. 22 – 28, 1999.
- [7] P. McEuen, “Single - wall carbon nanotubes,” *Physics World*, vol. 13, pp. 31 – 36, 2000.
- [8] R. Saito *et al.*, “Electronic - Structure of Chiral Graphene Tubules,” *Appl. Phys. Lett.*, vol. 68, p. 1579, 1992.
- [9] J.-C. Charlier, X. Blase, and S. Roche, “Electronic and transport properties of nanotubes,” *Rev. Mod. Phys.*, vol. 79 (2), pp. 677 – 732, 2007.
- [10] M. Dresselhaus, G. Dresselhaus, and P. Avouris, *Carbon Nanotubes: Synthesis, Structure, Properties and Applications*. Springer, New York, 2001.
- [11] P. Wallace, “The band theory of graphite,” *Phys. Rev.*, vol. 71, p. 622, 1947.

- [12] E. Minot, *Tuning the band structure of carbon nanotubes*. PhD thesis, Cornell University, 2004.
- [13] E. Minot *et al.*, “Determination of electron orbital magnetic moments in carbon nanotubes,” *Nature*, vol. 428, p. 536, 2004.
- [14] C. Zhou *et al.*, “Intrinsic electrical properties of individual single-walled carbon nanotubes with small band gaps,” *Phys. Rev. Lett.*, vol. 84, p. 5604, 2000.
- [15] V. Deshpande *et al.*, “Mott insulating state in ultraclean carbon nanotubes,” *Science*, vol. 323, pp. 106–110, 2009.
- [16] C. Kane and E. Mele, “Size, shape and low energy electronic structure of carbon nanotubes,” *Phys. Rev. Lett.*, vol. 78, p. 1932, 1997.
- [17] M. Ouyang *et al.*, “Energy gaps in ‘metallic’ single - walled carbon nanotubes,” *Science*, vol. 292, p. 702, 2001.
- [18] R. Heyd, A. Charlier, and E. McRae, “Uniaxial-stress effects on the electronic properties of carbon nanotubes,” *Phys. Rev. B*, vol. 55, p. 6820, 1997.
- [19] L. Yang and J. Han, “Electronic structure of deformed carbon nanotubes,” *Phys. Rev. Lett.*, vol. 85, p. 154, 2000.
- [20] D. Huertas Hernando *et al.*, “Spin-orbit coupling in curved graphene, fullerenes, nanotubes, and nanotube caps,” *Phys. Rev. B*, vol. 74, p. 155426, 2006.
- [21] F. Kuemmeth, Ilani, S. Ralph, D.C., and P. McEuen, “Coupling spin and orbital motion of electrons in carbon nanotubes,” *Nature*, vol. 452, p. 448, 2008.
- [22] T. Ando, “Spin-orbit interaction in carbon nanotubes,” *J. Phys. Soc. Jpn.*, vol. 69, p. 1757, 2000.
- [23] D. Bulaev *et al.*, “Spin-orbit interaction and anomalous spin relaxation in carbon nanotube quantum dots,” *Phys. Rev. B*, vol. 77, p. 235301, 2007.
- [24] K. Nowack *et al.*, “Coherent control of a single electron spin with electric fields,” *Science*, vol. 318, p. 1430, 2007.

## BIBLIOGRAPHY

---

- [25] K. Flensberg and C. M. Marcus, “Bends in nanotubes allow electric spin control and coupling,” *Phys. Rev. B*, vol. 81, p. 195418, 2010.
- [26] D. H. Cobden and J. Nygård, “Shell filling in closed single-wall carbon nanotube quantum dots,” *Phys. Rev. Lett.*, vol. 89, p. 046803, 2002.
- [27] P. Jarillo Herrero *et al.*, “Electron-hole symmetry in a semiconducting carbon nanotube quantum dot,” *Nature*, vol. 429, p. 389, 2004.
- [28] M. J. Biercuk *et al.*, “Gate-defined quantum dots on carbon nanotubes,” *Nano Lett.*, vol. 5, pp. 1267–1271, 2005.
- [29] S. Sapmaz *et al.*, “Excited state spectroscopy in carbon nanotube double quantum dots,” *Nano Lett.*, vol. 6(7), p. 1350, 2006.
- [30] S. Sapmaz *et al.*, “Quantum dots in carbon nanotubes,” *Semiconductor science and technology*, vol. 21 (11), pp. 52–63, 2006.
- [31] T. Balder, “Modeling quantum dots in realistic carbon nanotube devices,” Master’s thesis, Delft University of Technology, 2008.
- [32] M. A. Kastner, “The single-electron transistor,” *Rev. Mod. Phys.*, vol. 64, pp. 849–858, 1992.
- [33] L. Kouwenhoven, C. Marcus, P. McEuen, S. Tarucha, R. Westervelt, and N. Wingren, “Electron transport in quantum dots,” in *Mesoscopic electron transport* (L. Sohn, L. Kouwenhoven, and G. Schön, eds.), Series E 345, Kluwer, 1997.
- [34] A. Fuhrer, *Phase coherence, orbital and spin states in quantum rings*. PhD thesis, Swiss Federal Institute of Technology Zurich, 2003.
- [35] A. Johnson *et al.*, “Triplet-singlet spin relaxation via nuclei in a double quantum dot,” *Nature*, vol. 435, p. 925, 2005.
- [36] J. R. Petta *et al.*, “Coherent manipulation of coupled electron spins in semiconductor quantum dots,” *Science*, vol. 309, p. 2180, 2005.
- [37] F. H. L. Koppens *et al.*, “Driven coherent oscillations of a single electron spin in a quantum dot,” *Nature*, vol. 442, pp. 766–771, 2006.
- [38] F. Koppens *et al.*, “Universal phase shift and nonexponential decay of driven single-spin oscillations,” *Phys. Rev. Lett.*, vol. 99, p. 106803, 2007.

- [39] K. Ono *et al.*, “Current rectification by Pauli exclusion in a weakly coupled double quantum dot system,” *Science*, vol. 297, p. 1313, 2002.
- [40] I. Vink, *Manipulation and read-out of spins in quantum dots*. PhD thesis, Delft University of Technology, 2008.
- [41] H. O. H. Churchill *et al.*, “Relaxation and dephasing in a two-electron  $^{13}\text{C}$  nanotube double quantum dot,” *Phys. Rev. Lett.*, vol. 102, p. 166802, 2009.
- [42] A. Pályi and G. Burkard, “Hyperfine-induced valley mixing and the spin-valley blockade in carbon-based quantum dots,” *Phys. Rev. B*, vol. 80, p. 201404, 2009.
- [43] A. Pályi and G. Burkard. cond-mat/1005.2738.
- [44] J. Danon and Y. V. Nazarov, “Pauli spin blockade in the presence of strong spin-orbit coupling,” *Phys. Rev. B*, vol. 80, p. 041301, 2009.
- [45] A. Pfund, I. Shorubalko, K. Ensslin, and R. Leturcq, “Suppression of spin relaxation in an inas nanowire double quantum dot,” *Phys. Rev. Lett.*, vol. 99, p. 036801, 2007.
- [46] S. Nadj-Perge *et al.*, “Disentangling the effects of spin-orbit and hyperfine interactions on spin blockade,” *Phys. Rev. B*, vol. 81, p. 201305, 2010.
- [47] F. Koppens *et al.*, “Control and detection of singlet-triplet mixing in a random nuclear field,” *Science*, vol. 309, p. 1346, 2005.
- [48] R. Hanson *et al.*, “Spins in few-electron quantum dots,” *Rev. Mod. Phys.*, vol. 79, p. 1217, 2007.
- [49] B. Wunsch, “Few-electron physics in a nanotube quantum dot with spin-orbit coupling,” *Phys. Rev. B*, vol. 79, p. 235408, 2009.
- [50] A. Secchi and M. Rontani, “Coulomb versus spin-orbit interaction in few-electron carbon-nanotube quantum dots,” *Phys. Rev. B*, vol. 80, p. 041404, 2009.
- [51] A. Secchi and M. Rontani. cond-mat/0908.2092.
- [52] V. Deshpande and M. Bockrath, “The one-dimensional Wigner crystal in carbon nanotubes,” *Nature Physics*, vol. 4, p. 314, 2008.
- [53] E. Wigner, “On the interaction of electrons in metals,” *Phys. Rev.*, vol. 46, pp. 1002–1011, 1934.



## BIBLIOGRAPHY

---

- [54] H. O. H. Churchill *et al.*, “Electron-nuclear interaction in a  $^{13}\text{C}$  nanotube double quantum dot,” *Nature Phys.*, vol. 5, p. 321, 2009.
- [55] Y. Krotov *et al.*, “Low energy properties of (n,n) carbon nanotubes,” *Phys. Rev. Lett.*, vol. 78, p. 4245, 1997.
- [56] N. F. Mott, “Metal-insulator transition,” *Rev. Mod. Phys.*, vol. 40, pp. 677–683, 1968.
- [57] J. Cao, Q. Wang, and H. Dai, “Electron transport in very clean, as-grown suspended carbon nanotubes,” *Nature Mater.*, vol. 4, pp. 745 – 749, 2005.
- [58] P. L. McEuen, M. Bockrath, D. H. Cobden, Y.-G. Yoon, and S. G. Louie, “Disorder, pseudospins, and backscattering in carbon nanotubes,” *Phys. Rev. Lett.*, vol. 83, pp. 5098–5101, 1999.
- [59] B. W. Smith and D. E. Luzzi, “Electron irradiation effects in single wall carbon nanotubes,” *J. Appl. Phys.*, vol. 90, p. 3509, 2001.
- [60] T. Fulton *et al.*, “Observation of single-electron charging effects in small tunnel junctions,” *Phys. Rev. Lett.*, vol. 59, p. 109, 1987.
- [61] J. Kong *et al.*, “Synthesis of individual single-walled carbon nanotubes on patterned silicon wafers,” *Nature*, vol. 395, p. 878, 1998.
- [62] C. Fasth *et al.*, “Tunable double quantum dots in InAs nanowires defined by local gate electrodes,” *Nano Lett.*, vol. 5, pp. 1487 – 1490, 2005.
- [63] M. Field, C. G. Smith, M. Pepper, D. A. Ritchie, J. E. F. Frost, G. A. C. Jones, and D. G. Hasko, “Measurements of coulomb blockade with a non-invasive voltage probe,” *Phys. Rev. Lett.*, vol. 70, no. 9, pp. 1311–1314, 1993.
- [64] J. M. Elzerman *et al.*, “Few-electron quantum dot circuit with integrated charge read out,” *Phys. Rev. B*, vol. 67, no. 16, p. 161308, 2003.
- [65] D. Wallin *et al.*, “Detection of charge states in nanowire quantum dots using a quantum point contact,” *Appl. Phys. Lett.*, vol. 90, no. 17, p. 172112, 2007.
- [66] I. Shorubalko *et al.*, “Self-aligned charge read-out for InAs nanowire quantum dots,” *Nano Lett.*, vol. 8, no. 2, pp. 382–385, 2008.

- [67] M. Koltonyuk *et al.*, “Single-electron capacitance spectroscopy of vertical quantum dots using a single-electron transistor,” *Appl. Phys. Lett.*, vol. 74, p. 555, 1999.
- [68] W. Lu *et al.*, “Real-time detection of electron tunnelling in a quantum dot,” *Nature*, vol. 423, p. 422, 2003.
- [69] M. Biercuk *et al.*, “Charge sensing in carbon-nanotube quantum dots on microsecond timescales,” *Phys. Rev. B*, vol. 73, p. 201402, 2006.
- [70] R. Brenner, *Single-electron transistors for the detection of charge motion in the solid state*. PhD thesis, The University of New South Wales, 2004.
- [71] A. N. Korotkov, “Intrinsic noise of the single-electron transistor,” *Phys. Rev. B*, vol. 49, pp. 10381–10392, 1994.
- [72] C. Thelander *et al.*, “Nanowire single-electron memory,” *Nano Lett.*, vol. 5, no. 4, pp. 635–638, 2005.
- [73] B. Turek *et al.*, “Single-electron transistor backaction on the single-electron box,” *Phys. Rev. B*, vol. 71, p. 193304, 2005.
- [74] M. Avinun-Kalish *et al.*, “Controlled dephasing of a quantum dot in the Kondo regime,” *Phys. Rev. Lett.*, vol. 92, p. 156801, 2004.
- [75] V. Krupenin *et al.*, “Charging and heating effects in a system of coupled single-electron tunneling devices,” *Phys. Rev. B*, vol. 59, p. 10778, 1999.
- [76] E. Onac *et al.*, “Using a quantum dot as a high-frequency shot noise detector,” *Phys. Rev. Lett.*, vol. 96, p. 176601, 2006.
- [77] S. Hershfield *et al.*, “Zero-frequency current noise for the double-tunnel-junction Coulomb blockade,” *Phys. Rev. B*, vol. 47, pp. 1967 – 1979, 1993.
- [78] E. V. Sukhorukov, G. Burkard, and D. Loss, “Noise of a quantum dot system in the cotunneling regime,” *Phys. Rev. B*, vol. 63, p. 125315, 2001.
- [79] E. Onac, *High frequency noise detection*. PhD thesis, Delft University of Technology, 2005.
- [80] Y. Semenov *et al.*, “Electron spin relaxation in semiconducting carbon nanotubes: The role of hyperfine interaction,” *Phys. Rev. B*, vol. 75, p. 045429, 2007.

## BIBLIOGRAPHY

---

- [81] P. Jarillo Herrero *et al.*, “Orbital Kondo effect in carbon nanotubes,” *Nature*, vol. 434, p. 484, 2005.
- [82] N. Mason *et al.*, “Local Gate Control of a Carbon Nanotube Double Quantum Dot,” *Science*, vol. 303, p. 655, 2004.
- [83] R. Schleser *et al.*, “Time-resolved detection of individual electrons in a quantum dot,” *Appl. Phys. Lett.*, vol. 85, p. 2005, 2004.
- [84] S. Gustavsson *et al.*, “Measuring current by counting electrons in a nanowire quantum dot,” *Appl. Phys. Lett.*, vol. 92, p. 152101, 2008.
- [85] J. Elzerman *et al.*, “Excited-state spectroscopy on a nearly closed quantum dot via charge detection,” *Appl. Phys. Lett.*, vol. 84, p. 4617, 2004.
- [86] S. Tans *et al.*, “Individual single-wall carbon nanotubes as quantum wires,” *Nature*, vol. 386, p. 474, 1997.
- [87] M. Rudner and E. Rashba, “Spin relaxation due to deflection coupling in nanotube quantum dots,” *Phys. Rev. B*, vol. 81, p. 125426, 2010.
- [88] H. I. Jørgensen *et al.*, “Single wall carbon nanotube double quantum dot,” *Appl. Phys. Lett.*, vol. 89, p. 232113, 2006.
- [89] M. R. Gräber *et al.*, “Molecular states in carbon nanotube double quantum dots,” *Phys. Rev. B*, vol. 74, p. 075427, 2006.
- [90] D. Loss and D. DiVincenzo, “Quantum computation with quantum dots,” *Phys. Rev. A*, vol. 57, p. 120, 1998.
- [91] J. M. Elzerman *et al.*, “Single-shot read-out of an individual-electron spin in a quantum dot,” *Nature*, vol. 430, p. 431, 2004.
- [92] T. Fujisawa *et al.*, “Allowed and forbidden transitions in artificial hydrogen and helium atoms,” *Nature*, vol. 419, p. 278, 2002.
- [93] O. Klein, “Die Reflexion von Elektronen an einem Potentialsprung nach der relativistischen Dynamik von Dirac,” *Z. Phys.*, vol. 53, p. 157, 1929.
- [94] M. I. Katsnelson *et al.*, “Chiral tunneling and the Klein paradox in graphene,” *Nature Phys.*, vol. 2, p. 620, 2006.
- [95] B. Trauzettel *et al.*, “Spin qubits in graphene quantum dots,” *Nature Phys.*, vol. 3, p. 192, 2007.

- [96] W. G. van der Wiel *et al.*, “Electron transport through double quantum dots,” *Rev. Mod. Phys.*, vol. 75, p. 1, 2002.
- [97] S. De Francesci *et al.*, “Electron cotunneling in a semiconductor quantum dot,” *Phys. Rev. Lett.*, vol. 86, p. 878, 2001.
- [98] C. Zener, “A theory of the electrical breakdown of solid dielectrics,” *Roy. Soc. Proc.*, vol. 145, p. 523, 1934.
- [99] L. Esaki, “New phenomenon in narrow germanium p-n junctions,” *Phys. Rev.*, vol. 109, p. 603, 1958.
- [100] T. H. Stoof and Y. Nazarov, “Time-dependent resonant tunneling via two discrete states,” *Phys. Rev. B*, vol. 53, p. 1050, 1996.
- [101] T. Fujisawa *et al.*, “Spontaneous emission spectrum in double quantum dot devices,” *Science*, vol. 282, p. 932, 1998.
- [102] J. A. Misewich *et al.*, “Electrically induced optical emission from a carbon nanotube FET,” *Science*, vol. 300, p. 783, 2003.
- [103] T. Fujisawa *et al.*, “Inelastic tunneling in a double quantum dot coupled to a bosonic environment,” *Physica E*, vol. 7, p. 413, 2000.
- [104] T. Fujisawa *et al.*, “Spontaneous emission spectrum in double quantum dot devices,” *Science*, vol. 282, pp. 932–935, 1998.
- [105] D. Perkins, *Introduction to High Energy Physics*. Addison-Wesley, Menlo Park, 1987.
- [106] A. Bernardini *et al.*, “Relativistic tunneling and accelerated transmission,” *Phys. Rev. B*, vol. 77, p. 235301, 2008.
- [107] A. Vidan, R. M. Westervelt, M. Stopa, M. Hanson, and A. C. Gossard, “Triple quantum dot charging rectifier,” *Applied Physics Letters*, vol. 85, no. 16, pp. 3602–3604, 2004.
- [108] L. Gaudreau *et al.*, “Stability diagram of a few-electron triple dot,” *Phys. Rev. Lett.*, vol. 97, no. 3, p. 036807, 2006.
- [109] E. Laird *et al.*, “Coherent spin manipulation in an exchange-only qubit.” [cond-mat/1005.0273](https://arxiv.org/abs/cond-mat/1005.0273).
- [110] K. Grove-Rasmussen *et al.*, “A triple quantum dot in a single-wall carbon nanotube,” *Nano Letters*, vol. 8, no. 4, pp. 1055–1060, 2008.

## BIBLIOGRAPHY

---

- [111] D. S. Saraga and D. Loss, “Spin-entangled currents created by a triple quantum dot,” *Phys. Rev. Lett.*, vol. 90, p. 166803, 2003.
- [112] A. D. Greentree *et al.*, “Coherent electronic transfer in quantum dot systems using adiabatic passage,” *Phys. Rev. B*, vol. 70, p. 235317, 2004.
- [113] A. C. Johnson, J. R. Petta, C. M. Marcus, M. P. Hanson, and A. C. Gossard, “Singlet-triplet spin blockade and charge sensing in a few-electron double quantum dot,” *Phys. Rev. B*, vol. 72, no. 16, p. 165308, 2005.
- [114] D. Farmer and R. Gordon, “Atomic layer deposition on suspended single-walled carbon nanotubes via gas-phase noncovalent functionalization,” *Nano Lett.*, vol. 6, no. 4, pp. 699–703, 2006.
- [115] O. Usmani, Y. M. Blanter, and Y. V. Nazarov, “Strong feedback and current noise in nanoelectromechanical systems,” *Phys. Rev. B*, vol. 75, no. 19, p. 195312, 2007.
- [116] B. Lassagne *et al.*, “Coupling Mechanics to Charge Transport in Carbon Nanotube Mechanical Resonators,” *Science*, vol. 325, pp. 1107–1110, 2009.
- [117] G. A. Steele *et al.*, “Strong Coupling Between Single-Electron Tunneling and Nanomechanical Motion,” *Science*, vol. 325, pp. 1103–1107, 2009.
- [118] M. Pioro-Ladriere *et al.*, “Electrically driven single-electron spin resonance in a slanting Zeeman field,” *Nature Physics*, vol. 4, pp. 776–779, 2008.



# Summary

## Single Electron-ics with Carbon Nanotubes

In this thesis, we investigate the electrical properties of quantum dots (QDs) made from carbon nanotubes (CNTs). Single-wall CNTs are hollow cylinders, made out of a single layer of carbon atoms which are arranged in a hexagonal structure. CNTs have diameters of only a few nm and possess remarkable electrical and mechanical properties. QDs, often also called *artificial atoms*, are small structures containing a well-defined number of electrons with a discrete energy spectrum. At temperatures below a few Kelvin, a short ( $\leq 1\mu\text{m}$ ) segment of a CNT forms such a QD.

The energy spectrum of a QD can provide information about the electronic structure of the CNT, as well as give insight into physical properties of electrons in one- and zero-dimensional systems in general. Furthermore, there is the possibility of using the spin of confined electrons for new types of electronic devices, e.g. *quantum bits*. CNTs are of particular interest for these applications: On the one hand, CNTs without any nuclear spins can be fabricated, thereby eliminating the main source of spin decoherence in other QD systems. On the other hand, spin and orbital degrees of freedom are coupled in CNT, which enables spin manipulation with electric fields.

Until recently, the charge states and the spectra of CNT-QDs were investigated by electrical transport measurements only. In this thesis, we make use of an external charge detector in order to study a CNT-QD independently of current transport. In our case, the charge detector is a metallic single electron transistor (SET) which is capacitively coupled to the CNT. Charge detection is necessary for investigating closed quantum dots where transport measurements are not possible due to the low tunneling rates. This is important for slow processes or single shot read-out of a QD. Also, charge sensing yields cleaner spectroscopy data than transport measurements in the case that there exist resonances in the leads, which is almost inevitable in one-dimensional systems. In our experiments, we demonstrate that the tunneling rates into a CNT-QD can be tuned by elec-

trostatic gates with high precision down to frequencies below 1 Hz. We show this by reading out the charge state of a CNT-QD in real time. Also the excited state spectrum of such a closed QD is measured with the charge detector. When investigating backaction effects, we find that using a SET with a small charging energy keeps the backaction to the CNT-QD low, while maintaining a sufficient coupling for the charge readout. At the same time, the SET is also sensitive to the shot noise in the current through the CNT-QD.

In the second part of this thesis, we describe a fabrication scheme that aims at minimizing the fabrication-induced disorder in CNT devices. For CNTs this is crucial, since they basically consist of surface only. This makes them very susceptible to disorder induced from the environment. We first fabricate gates and contacts and then grow the CNTs on top of these structures in the very last fabrication step. Furthermore, to suspend the CNTs, we grow them across a trench which is etched into the substrate. Originally, the fabrication scheme uses separated areas of a highly doped silicon layer inside the substrate as gates. This, however, imposes some limitations on possible devices. A new scheme allows us to fabricate devices with a larger number of narrow metallic gates, enhancing the tunability of the QD devices and also making the application of high-frequency electrical pulses possible.

The absence of disorder in these devices allows to define few-electron single, double and triple quantum dots in a CNT by electrostatics gates. Tunnel barriers can be defined by p-n junctions, which is possible because of the ambipolar nature of CNTs. In the the same device, we can define both few-electron single and double-QDs, depending on the voltages applied to the gates. Also, we can define QDs with either electrons or holes as charge carriers. In particular it is possible to create multiple QDs with alternating types of charge carriers (e.g. p-n double QDs and n-p-n triple QDs). In a clean CNT with a small bandgap, we demonstrate that tunneling through a barrier shows a phenomenon which is similar to Klein tunneling in relativistic quantum mechanics.

Finally, we discuss the possibilities for experiments on coherent spin manipulation with the clean, as-grown CNT devices. Different schemes - some of them adapted from GaAs QD systems, some of them proposed exclusively for CNTs - are considered and important problems are identified and analyzed.

Georg Götze  
May 2010



# Samenvatting

## Enkele Elektron-ica met Koolstof Nanobuisjes

In dit proefschrift worden de elektronische eigenschappen van kwantum dots (KDs) gemaakt van koolstof nanobuisjes (KNBs) onderzocht. Enkele-wand KNBs zijn holle cilinders, gemaakt van slechts één laag koolstofatomen. De koolstofatomen zitten in een hexagonale raster structuur, zoals bij een honingraat. KNBs hebben een diameter van slechts enkele nanometers en bezitten bijzondere elektronische en mechanische eigenschappen.

KDs worden vaak ook *kunstmatige atomen* genoemd. Het zijn kleine structuren waarin het aantal elektronen goed gedefinieerd is en de elektronen een discreet energie spectrum hebben. Bij temperaturen beneden enkele Kelvin, kan er een KD gevormd worden in een kort ( $\leq 1\mu\text{m}$ ) stukje van één KNB.

Naast informatie over de elektronische structuur van de KNB kunnen ook de fysische eigenschappen van elektronen in 1-dimensionale en 0-dimensionale systemen uit het energie spectrum van één KD afgeleid worden. De KD in de KNB is een model systeem voor het bestuderen van de fysica van laag dimensionale systemen. Daarnaast is het mogelijk om de spin van geïsoleerde elektronen in de KD te gebruiken in nieuwe elektronische systemen, zoals quantum bits. In andere KD systemen zijn kernspins een belangrijke bron van spin-decoherentie. Er kunnen echter KNBs gemaakt worden zonder kernspins. Ook is er spin-baan wisselwerking in de KNB, die het mogelijk maakt om spin manipulatie met elektrische velden uit te voeren. Deze eigenschappen maken KNBs bijzonder geschikt voor quantum bits.

Tot voor kort werden ladingstoestanden en de energie spectra van KNB-KDs alleen maar onderzocht met elektrische transport metingen. In dit proefschrift maken we gebruik van een externe ladingsdetector om de de KNB-KD te bestuderen. De ladingsdetector is een metallisch “single-electron-transistor” (SET), die capacitief gekoppeld is aan de KNB. Voor het onderzoeken van gesloten KDs is ladingsdetectie noodzakelijk. In deze KDs zijn transportmetingen niet mogelijk vanwege de lage tunnel frequentie. Voor het bestuderen van langzame processen,

of het in-één-keer uitlezen van een KD, is ladingsdetectie nodig. Daarnaast levert ladingsdetectie schonere spectroscopie data op in vergelijking met transport metingen. Dit is in het bijzonder zo wanneer er resonanties zijn in de contacten, iets wat bijna onvermijdbaar is in 1-dimensionale systemen.

In onze experimenten laten we zien dat de tunnelfrequentie in een KNB-KD nauwkeurig afgesteld kan worden met elektrostatische gates, tot frequenties beneden 1Hz. Dit tonen we aan door de ladingstoestand van de KNB-KD real-time uit te lezen. We meten ook het spectrum van de aangeslagen toestanden van een gesloten KD met een ladingsdetector. We onderzoeken de terugwerkende effecten en zien dat wanneer we een SET met een kleine ladingsenergie gebruiken, de terugwerking op de KNB-KD klein is, terwijl we toch voldoende koppeling hebben voor het uitlezen van de ladingstoestand. Tegelijkertijd is de SET gevoelig voor shot noise in de stroom door de KNB-KD.

In het tweede deel van dit proefschrift beschrijven we een nieuwe fabricage-techniek. Het doel van deze techniek is om door fabricage veroorzaakte wanorde in de KNB systemen te minimaliseren. Dit is cruciaal voor KNBs omdat ze voornamelijk uit een oppervlak bestaan. Dit maakt ze zeer gevoelig voor wanorde veroorzaakt door de omgeving van de KNB. We beginnen met het fabriceren van de gates en contacten en groeien de KNB op deze structuren in de allerlaatste fabricage-stap. Om hangende KNBs te maken, groeien we ze over een geul die geëët is in het substraat. Eerst hebben we gates te gemaakt van hooggedoteerde silicium lagen in het substraat. Deze methode levert echter beperkingen op. Met een andere methode kunnen we systemen maken met een groot aantal smalle metallische gates, waardoor de afstelling van KDs eenvoudiger wordt. Deze gates maken ook het gebruik van hoog frequente elektrische pulsen mogelijk.

De afwezigheid van wanorde in onze systemen maakt het mogelijk om met gates, enkele-elektron, enkel, dubbel en drievoudige KDs te maken. Het ambipolaire karakter van KNBs maakt het mogelijk om tunnelbarrières te vormen met P-N juncties. In hetzelfde systeem, kunnen we enkel-elektron enkel- en dubbel KD's maken. We kunnen ook elektron- of gat KDs maken. KNBs zijn bijzonder geschikt voor het maken van een reeks KDs met variërende ladingsdrager, bijvoorbeeld P-N dubbel KD en N-P-N drievoudige KDs.

In een schone KNB met een kleine bandgap, tonen we aan dat het tunnelen door een barrière vergelijkbaar is met Klein-tunnelen in relativistische kwantum mechanica.

Ten slotte beschrijven we mogelijke experimenten waarin schone KNBs gebruikt kunnen worden voor coherente spin manipulatie. Schemas die al toegepast zijn op GaAs KDs, maar ook schemas die exclusief van toepassing zijn op KNB KDs worden beschreven. De belangrijke problemen worden hier door ons geïdenti-

---

ficeerd en geanalyseerd.

Georg Götz  
Mei 2010



# Curriculum Vitae

Georg Thomas Jakob Götz

- October 15, 1979    Born in Hamburg, Germany.
- 1990 – 1999        Gymnasium Christianeum, Hamburg.
- 2000 – 2005        Studies of Physics (with distinction),  
ETH Zürich, Switzerland.  
Diploma Thesis (under supervision of Prof. K. Ensslin):  
*Symmetries of magneto-transport in a mesoscopic ring*
- 2004                ERASMUS student at Aarhus University, Denmark.
- 2006 – 2010        PhD research at Delft University of Technology  
under supervision of prof. dr. ir. L. P. Kouwenhoven  
Subject: *Single Electron-ics with Carbon Nanotubes*



# Publications

1. *Tunable few-electron double quantum dots and Klein tunnelling in ultraclean carbon nanotubes*  
G.A. Steele, G. Gotz, & L.P. Kouwenhoven  
Nature Nanotechnology Vol. **4**, No. 6, p. 363-367 (2009).
2. *Real Time Electron Tunneling and Pulse Spectroscopy in Carbon Nanotube Quantum Dots*  
G. Gotz, G.A. Steele, W.-J. Vos, & L.P. Kouwenhoven  
Nano Letters Vol. **8**, No. 11, p. 4039-4042 (2008).
3. *Coherent nonlinear transport in quantum rings*  
R. Leturcq, R. Bianchetti, G. Gotz, T. Ihn, K. Ensslin, D.C. Driscoll & A.C. Gossard  
Physica E **35**, No. 2, p. 327-331 (2006).
4. *Magnetic field symmetry and phase rigidity of the nonlinear conductance in a ring*  
R. Leturcq, D. Sanchez, G. Gotz, T. Ihn, K. Ensslin, D.C. Driscoll & A.C. Gossard  
Physical Review Letters **96**, 126801 (2006).

